An Investigation of Lightning-Generated Whistler Waves in the Inner Magnetosphere

Hao Zheng

A dissertation

submitted in partial fulfillment of the

requirements for the degree of

Doctor of Philosophy

University of Washington

2019

Reading Committee:

Robert Holzworth, Chair

Michael McCarthy

Abram Jacobson

Program Authorized to Offer Degree:

Earth and Space Sciences

University of Washington

Abstract

An Investigation of Lightning-Generated Whistler Waves in the Inner Magnetosphere

Hao Zheng

Chair of the Supervisory Committee:
Professor Robert Holzworth
Earth and Space Sciences

In this dissertation, we use a new and unique dataset to investigate lightning-generated whistler waves in the Earth's inner magnetosphere. Global lightning data and high-resolution waveform data in the inner magnetosphere are combined to study lightning-generated whistler waves including source, propagation, and potential scattering effects. Lightning can produce strong broadband radio waves especially in the very low frequency (VLF) band from 300 Hz to 30 kHz. A fraction of wave energy leaks into the ionosphere during reflections in the Earth-ionosphere waveguide and becomes lightning-generated whistler waves. Lightning-generated whistler waves and energetic electrons are important in the inner magnetosphere dynamics. The recent launch of the near-equatorial Van Allen Probes provides a great opportunity to observe and study lightning-generated whistler waves. During the conjunction work between World Wide

Lightning Location Network (WWLLN) and Van Allen Probes, we successfully predict the occurrence of lightning-generated whistler waves near the geomagnetic equator at low L-shells ($L < 3$) with a rate of ~80%. About 22.6% of whistler waves observed by Van Allen Probes correspond to possible source lightning in the WWLLN data, which agrees with the detection efficiency of WWLLN. About 40.1% additional whistler waves observed by Van Allen Probes may be related with WWLLN lightning if the source region is extended from 2000 km to the global area. The far-field radiated energy of lightning may not be the dominant factor for the appearance of lightning-generated whistler waves if it is larger than 100 J. By using the high-resolution waveform data from Van Allen Probes, we can study the possible pitch angle scattering process in both ducted whistler wave and non-ducted whistler wave events. Diffusion coefficients calculated from the high-resolution waveform data show that strong lightning-generated whistler waves may be important for scattering electrons with energies around 100 keV. Ducted whistler waves may be more effective in pitch angle scattering than non-ducted whistler waves due to smaller wave normal angles. The work in this dissertation shows the possibility to simulate the electron precipitation caused by lighting-generated whistler waves in individual cases.

TABLE OF CONTENTS

LIST OF FIGURES

LIST OF TABLES

ACKNOWLEDGEMENTS

At first, I would like to thank my advisor, Robert Holzworth, for his amazing guidance and support over the past 6 years. I am deeply grateful that he provided countless advices with his board insights in science and in life. His help is extremely important for me, an international student, who is far away from home to dive into the mystery space. I will always enjoy our discussions about science, career and life.

I also want to thank my committee members, Michael McCarthy, Abram Jacobson, John Sahr and Mike Wallace, for their support over the years. Special thanks to Michael McCarthy, for his wealth of knowledge and enthusiastic support in both theoretical research and hardware engineering.

In addition, I would like to thank Qianli Ma and Jinxing Li for providing the assistant of simulation work in Chapter 3, and for their contributions in discussing the results.

My friends in JHN 266 made my graduate life easier than fighting alone. I will miss the wonderful journey at UW with Michael Hutchins, Brian Burkholder, Todd Anderson, Paul Sturmer and of course Leo, who I know for more than 10 years.

Finally, I would like to thank my family for their long-time support. My parents and parents-in-law may never understand my research, but they just share their endless love without any hesitate. My wife Tianshi (Skye) has shown incredible patience and understanding for the past 6 years. Thank you Tianshi, I love you.

DEDICATION

To Tianshi

Chapter 1. INTRODUCTION

Magnetosphere is the region around a planet dominated by the planet's magnetic field. The shape of the Earth's magnetosphere is the direct result of being blasted by solar wind. The Earth's inner magnetosphere is the region with nearly dipolar magnetic field, which usually points to the region within 8 R_E (radius of Earth) to the center of the Earth at night side. There are two important parts inside the inner magnetosphere, which are separated by plasma energies, not the locations. First is the plasmasphere, which has dense and cold plasma. The other part is called radiation belts, where the energetic particles are located. This is a brief introduction of the Earth's inner magnetosphere. In the following sections, we will specifically explain the magnetosphere, the radiation belts, basic motions of charged particles, important plasma waves and the wave-particle interactions in the inner magnetosphere.

1.1 THE EARTH'S MAGNETOSPHERE

The solar wind plasma cannot easily penetrate the Earth's magnetic field but is mostly deflected around it. As explained in *Baumjohann and Treumann* [1997], the interplanetary magnetic field lines cannot penetrate the Earth's field lines. The boundary separating the two different regions is called magnetopause. And the cavity generated by the Earth's field has been named magnetosphere. At the dayside, solar wind compresses the field to about 10 R_E, while the nightside magnetic field is stretched out into a long magnetotail to > 60 R_E. The structure of the Earth's magnetosphere and some related regions are shown in Figure 1.1.

The plasmasphere is a region consisting of dense (~10 cm^{-3}) but low energy (<1 eV) plasma (light blue region in Figure1.1). It is located above the ionosphere and within the region called plasmapause, which is defined by an order of magnitude drop in plasma density. The plasmapause

was discovered by *Carpenter* [1963] from the analysis of the VLF whistler wave data. The plasmasphere is also treated as the separation of corotating plasma and the convecting plasma in the inner magnetosphere.

Besides cold plasma in the plasmasphere, there are also energetic particles which are trapped by the Earth's magnetic field and form the radiation belts (red dot region in Figure 1.1). The hot particles consist electron and protons with energies higher than 30 keV, which may be harmful for the spacecrafts and astronauts in this region.

The dominant component of the Earth's magnetic field is a nearly dipolar field in the inner magnetosphere. The geometry can be explained by a formula of $r = Rcos^2\lambda$, where r is the distance to the center of the Earth, R is the equatorial distance of the same magnetic field line to the center of the Earth, and λ is the latitude. In this work, we only focus on the region in the inner magnetosphere and a dipolar magnetic field model is used if not specifically pointed out.

1.2 The Radiation Belts

The existence of the radiation belts is firstly confirmed by Explorer 1 and Explorer 3 in early 1958 under James Van Allen [*Van Allen and Frank*, 1959], and as a result, Earth's belts are also known as the Van Allen Belts. From the observations of energetic electron flux, it is indicated that the Earth's radiation belts are located at two distinct zones separated by a region of depleted flux called slot [e.g., *Horne et al.*, 2003]. The structure of the inner zone tends to be relatively stable between L = 1.2 – 2 (L is the equatorial distance of the magnetic field line to the center of the Earth, in the unit of R_E). The outer zone is highly dynamic between L = 3 – 8 [*Millan and Thorne*, 2007]. The separation of inner and outer radiation belt is generally based on electron flux. For proton flux, there is only one peak in the inner radiation belt. The energetic particles are trapped stably in the radiation belts by the magnetic field. At low altitude, collisions between trapped particles and

atmospheric particles is the main loss mechanism of radiation belt particles. Energetic particles may also be lost at magnetopause due to the variation of solar wind conditions. The source of radiation belt particles is still under study. One major source of high-energy particles of the inner radiation belt is secondary particles from cosmic rays. The main source of outer radiation belt particles seems to be the solar wind, but the pathways by which this energy is transported and distributed in the magnetosphere are not yet completely clear.

1.3 The Significance of Radiation Belts Research

The study of radiation belts especially the outer radiation belt is important. There are many satellites working in this region, for example, the geostationary orbit is located at ~6.6 R_E and the GPS satellite orbit is located at ~4.2 R_E. Other spacecrafts like deep space exploration spacecraft or moon-landing, mars-landing spacecrafts all need to pass through this region to their destinations. Figure 1.2 shows several types of space environment hazards caused by energetic particles, which may affect the spacecrafts by internal charging, surface charging and single event. As explained in *Meredith et al*., [2016], relativistic electrons, which are also called "killer" electrons, can penetrate spacecraft shielding and may stack in the insulators and conductors. This charge can accumulate over time and generate high electric fields which may lead to an internal discharge and damage satellite components. Single Event Effects are caused by a single, energetic particle (usually a high energy proton). They can be soft errors like Single Event Upsets, which are non-destructive but provide wrong signals, or hard errors like Single Event Latch-up, which must be cleared by a power reset. The high energy particles may also be harmful for astronauts. The major goal of NASA's Space Radiation Program Element is to develop the knowledge to accurately predict and efficiently manage the radiation risk of human flight. The ionizing radiation depositing energy in living bodies can cause structural damage to DNA and change cellular processes.

1.4 PARTICLE MOTIONS

The dynamics of charged particles in the inner magnetosphere are controlled by magnetic field (B) and electric field (E). In general, the motion of particles can be described by the momentum equation:

$$\frac{d\boldsymbol{p}}{dt} = q\,(\mathbf{E} + \boldsymbol{v} \times \mathbf{B}), \tag{1.1}$$

where $\boldsymbol{p} = \gamma m_0 \boldsymbol{v}$ is the particle momentum, q is the charge of the particle, m_0 is the rest mass, $\boldsymbol{v}$ is the particle velocity, **E** is the electric field, **B** is the magnetic field and γ is the Lorentz factor, which is used for relativistic electrons. Figure 1.3 shows that there are three basic motions when a charged particle is moving in the Earth's magnetic field over three different timescales [*Walt*, 1994]: fast gyration around the magnetic field line with a period of about millisecond; bounce motion along the magnetic field line between mirror points at northern and southern hemisphere with a period of about second; drift motion around the Earth with a period of 1 – 10 minutes. There are three adiabatic invariants associated with each type of motions:

$$\begin{aligned} \mu &= \frac{v_\perp^2}{2B}, \\ J &= \int_a^b m v_\parallel ds\,, \\ \Phi &= \iint \boldsymbol{B} d\boldsymbol{S}\,, \end{aligned} \tag{1.2}$$

If the outside perturbations or variations are much slower than the timescales, the adiabatic invariants are treated as conserved. The first adiabatic invariant is μ, which is also called magnetic moment. The second adiabatic invariant is J, which is also called longitudinal invariant. The last one is Φ, which is the total magnetic flux enclosed by a drift surface. The pitch angle (PA) is the angle of a charged particle between the particle's velocity vector and the local magnetic field. It is

defined as $\alpha = tan^{-1}(v_{\perp}/v_{\parallel})$. Based on that, we can change the first adiabatic equation to another form:

$$v_{\parallel} = v\,cos\alpha, \qquad v_{\perp} = v\,sin\alpha, \qquad \frac{sin^2(\alpha_0)}{sin^2(\alpha_m)} = \frac{B_0}{B_m}, \tag{1.3}$$

where B_0 is the equatorial magnetic field strength, B_m is the maximum magnetic field strength (it can be any point of the same magnetic field line), α_0 is the equatorial pitch angle of the particle and $\alpha_m$will be 90° at maximum (or the pitch angle of the particle at the point corresponding to B_m). When the pitch angle reaches 90°, the particle effectively reflects and travels in the opposite direction along the same field line. In (1.3) it is shown that the position or the altitude of mirror point is decided by the magnetic field strength and the equatorial pitch angle.

As mentioned in previous section, the main loss mechanism of trapped particles in the inner magnetosphere is due to the collisions between energetic particles and atmospheric particles. This happens when the mirror point is lower enough to reach upper atmosphere (usually we use altitude of 100 km as the lowest mirror point of particles when they can still bounce back). If the mirror point is higher than 100 km, the particles are stably trapped. If the mirror point is lower than 100 km, the particles will precipitate into the atmosphere and get lost. The altitude of mirror point at 100 km is related to a specific equatorial PA, which we call it loss cone angle. In Figure 1.4, three types of mirror points are shown to explain the relationship between the mirror point altitude and the equatorial pitch angle. The particles with larger pitch angle than the loss cone angle at equator will be stably trapped in the inner magnetosphere, while the particles with smaller pitch angle than the loss cone angle at equator will precipitate into the atmosphere. In this work, we will discuss the mechanisms that slightly change the pitch angle of particles from loss cone angle to a smaller value.

1.5 PITCH ANGLE SCATTERING

Pitch angle scattering, which is also known as pitch angle diffusion, is one of the main processes by which energetic particles are removed from the inner magnetosphere. In this work, we will focus on the pitch angle scattering caused by the wave-particle interactions. To be specifically, we study the interactions between lightning-generated whistlers and energetic particles in the inner magnetosphere. When the plasma waves and the energetic particles meet some conditions, they can interact with each other. Through the interactions, the plasma waves can change the momentum, energy and pitch angles of particles. This condition is what we called resonance conditions:

$$\omega - k_{\parallel} v_{\parallel} = n\frac{\Omega}{\gamma} \tag{1.4}$$

where ω is the wave frequency, $k_{\parallel}$ is the parallel component of wave vector **k**, $v_{\parallel}$ is the parallel component of particle velocity vector **v**, Ω is the electron cyclotron frequency, n is the harmonic number integer (0, ±1, ±2, …) and γ is the Lorentz factor. During resonance, the pitch angle of electrons stochastically increases or decreases by the waves, but the gradient of the distribution function will decrease. An illustration of normal first-order cyclotron resonance between right-hand circularly polarized waves and electrons is shown in Figure 1.5.

1.6 WHISTLER-MODE WAVES IN THE INNER MAGNETOSPHERE

Resonant scattering by whistler-mode VLF waves is a main loss mechanism for radiation belt electrons at L > 1.3 [*Abel and Thorne*, 1998a]. There are three main types of whistler-mode waves in the inner magnetosphere: hiss wave, chorus wave and lightning-generated whistler wave. Hiss wave, which is also called plasmaspheric hiss, is frequently observed at a high-density region in the plasmasphere. The emissions of hiss are incoherent with a wide frequency band between ~50

Hz to 1 kHz [*Li et al*., 2013]. The key feature of hiss waves is the structureless and mixed phase at similar frequency band. There are three main generation sources of hiss waves in the inner magnetosphere: local generation by electron injections, chorus propagated from the region out of the plasmapause and mixed lightning-generated whistlers. Hiss waves may cause the loss of energetic electrons with energies from tens of keV to several MeV in the plasmasphere [*Ni et al*., 2013]. Unlike hiss waves, chorus waves are coherent emissions between ~0.1f_{ce} and f_{ce}. Chorus waves are usually observed outside of the plasmapause with two types of structure, rising tone and falling tone. The rising tones usually has a stronger wave amplitude than falling tones [*Li et al*., 2011]. Lightning-generated whistler waves (whistler waves or whistlers) are also coherent emissions. The frequency of terrestrial whistlers is 1 – 30 kHz and in the plasmasphere, the lightning-generated whistlers have an upper cutoff at local electron plasma frequency and gyrofrequency. The electron whistlers usually have a structure of falling tone, which means the high frequency components travel faster than the low frequency components. In this work, we will focus on lightning-generated whistler waves and their contribution to the pitch angle scattering of energetic electrons in the inner magnetosphere. In the recent decades, it is shown that some other types of waves may also be important for energetic electron precipitation in the inner magnetosphere, like man-made VLF transmissions and electromagnetic ion cyclotron (EMIC) waves [e.g., *Meredith et al*., 2003a, *Ma et al*., 2017].

1.7 Lightning and Lightning-Generated Whistler Waves

Lightning can produce strong broadband radio waves, called “sferics”, which propagate in the Earth-ionosphere waveguide and are detected thousands of kilometers away from their source. The strongest waves are in the ELF/VLF bands from 300 Hz to 30 kHz. During propagation in the Earth-ionosphere waveguide, the ELF/VLF waves reflect many times between the surface of the

Earth and the ionosphere. Since the ionosphere is not a perfect conductor, a fraction of wave energy leaks into the ionosphere and propagates upward to the top of ionosphere, and further to the inner magnetosphere. Figure 1.6 illustrates the process, with black arrows showing different paths in the Earth-ionosphere waveguide and red arrows showing the upward propagation of lightning-generated whistler waves (Note that Figure 1.6 is just a cartoon plot. The direction of lightning-generated whistler waves won't be vertical upward in the ionosphere until multiple refractions due to the Snell's law). It is also shown in this figure that there are multiple entry points for lightning-generated whistler waves to the ionosphere at reflections.

Lightning-generated whistler is a right-handed circularly polarized wave. The dispersion relation of electromagnetic wave propagating in the cold magnetized plasma can be explained by Appleton-Hartree equation:

$$\mathrm{n}^2 = 1 - \frac{X}{1 - \frac{Y^2 sin^2\theta}{2(1-X)} \pm \left[\frac{Y^4 sin^4\theta}{2(1-X)^2} + Y^2 cos^2\theta\right]^{\frac{1}{2}}}, \qquad (1.5)$$

$$X = \frac{\omega_{pe}^2}{\omega^2}, \qquad Y = \frac{|\omega_{ce}|}{\omega}.$$

where n is the refractive index, ω_{ce} is the electron cyclotron frequency, ω_{pe} is the electron plasma frequency and ω is the wave frequency. For lightning-generated whistler waves in the inner magnetosphere, the approximation of $X \gg 1$ is applied on (1.5), and we can get

$$\mathrm{n}^2 \approx 1 - \frac{X}{1 - Ycos\theta} = 1 - \frac{\omega_{pe}^2}{\omega(\omega - \omega_{ce}cos\theta)}. \qquad (1.6)$$

Based on (1.6), we can also calculate the group velocity of lightning-generated whistler waves when $\omega \ll \omega_{ce}$,

$$v_g = \frac{\partial\omega}{\partial k} \approx 2c\frac{\sqrt{\omega\omega_{ce}}}{\omega_{pe}} \propto \sqrt{f}. \qquad (1.7)$$

From the group velocity formula, we can find that when frequency is low, the high frequency component has a higher group velocity which agrees with the falling tone structure.

1.8 Electron Precipitation Caused by Lighting-Generated Whistler Waves

Figure 1.7 illustrates the basic physics processes how lightning-generated whistler waves can cause the precipitation of energetic electrons. 1) A lightning discharge produce broadband radiation especially in VLF frequency range. 2) A fraction of energy from VLF waves leaks into the inner magnetosphere as whistler waves, which propagate along (or in some angles) with magnetic field to the magnetic equator. 3) Whistler waves can effectively interact with energetic electrons in the radiation belts when the resonance conditions meet, which leads to the pitch angle scattering of electrons. 4) The new mirror point of electrons is too low, so the electrons collide with atmospheric particles and precipitate into the atmosphere. This phenomenon, which is named Lightning-induced Electron Precipitation (LEP), was firstly discovered using in situ rocket measurements [e.g., *Rycroft*, 1973, *Goldburg et al.*, 1985]. LEP is a known troposphere-to-magnetosphere coupling mechanism. The first satellite measurements of LEP events was reported by *Voss et al.*, [1984]. As shown in Figure 1.8, multiple electron flux bursts are observed at several hundred kilometers altitude, with almost simultaneous existence of whistler waves. In the LEP events, the particles precipitate during the initial bounce path after the wave-particle interactions, so we say that the pitch angle of particles drops into the bounce loss cone. Besides the bounce loss cone, there is another type of loss cone called drift loss cone. Figure 1.9 shows a drift loss cone precipitation event caused by lightning. The drift loss cone is different with the bounce loss cone in that the particle doesn't precipitate within one bounce period after the wave-particle interactions,

but precipitate within one drift period around the Earth. The reason for that is the South Atlantic Anomaly (SAA). The particle in the L-shell range of SAA may be temporarily trapped if the pitch angle is larger than the local bounce loss cone angle but may still precipitate during its eastward drift when its pitch angle is smaller than the bounce loss cone angle at SAA.

1.9 Summary and Thesis Structure

The lightning-generated whistler waves and energetic particles are significant in the inner magnetosphere dynamics. It is important to investigate the lightning-generated whistler waves including the lightning source, the propagation from troposphere to magnetosphere, the wave-particle interactions in the inner magnetosphere and the electron precipitations as a result. In previous work, there are several limitations of available data, so it is hard to statistically study the correlations between global lightning and whistler waves in the inner magnetosphere. The limitations usually come from two parts, data of lightning and data of whistler waves. Lightning data is usually limited by the resolution or coverage. For example, lightning data may only be available at some local regions or globally but with only a low resolution. In this thesis, we will use the lightning data from World Wide Lightning Location Network (WWLLN), which is a long-range network capable of locating global lightning strokes in space and time. WWLLN is capable to locate lightning to within a few kilometers and ten microseconds and also provide a far-field energy from the detected strokes in the 6 – 18 kHz band. The other limitation comes from the satellite measurements of whistler waves in the inner magnetosphere. In previous research, the lightning-generated whistler waves are usually studied at hundreds of kilometer altitude, like DEMETER satellite. CRRES may be the only satellite specifically designed for radiation belts research in the past. There are a lot of studies on long time scale plasma waves based on CRRES

data. But the data may not be accurate for lightning-generated whistler waves due to low time resolution. Lightning-generated whistler waves usually have a time scale within second, so it is required to have a high sample rate in the data. In this thesis, we will use the most recent data from Van Allen Probes (RBSP), which are designed to understand the dynamics in the Earth's radiation belts.

The burst mode data obtained with a high sampling rate from Van Allen Probes can be a powerful tool to study detailed changes in the radiation belts. By using the data from WWLLN and Van Allen Probes, we will study the propagation of lightning-generated whistler waves and the related pitch angle scattering processes. The results of this thesis are based on previous studies but working on totally new data sets and they can show a new view or path to understand the dynamics of lightning-generate whistler waves in the inner magnetosphere. In Chapter One, we introduce background information, previous understandings and the reason of our research. In Chapter Two, we will show the statistical results of one-to-one coincidence between lightning and lightning-generated whistler waves observed in the inner magnetosphere. In Chapter Three, we will focus on two events to study pitch angle scattering processes related with two types of lightning-generated whistler waves. In Chapter Four, we will summarize the results in this thesis and also provide some suggestions for future work.

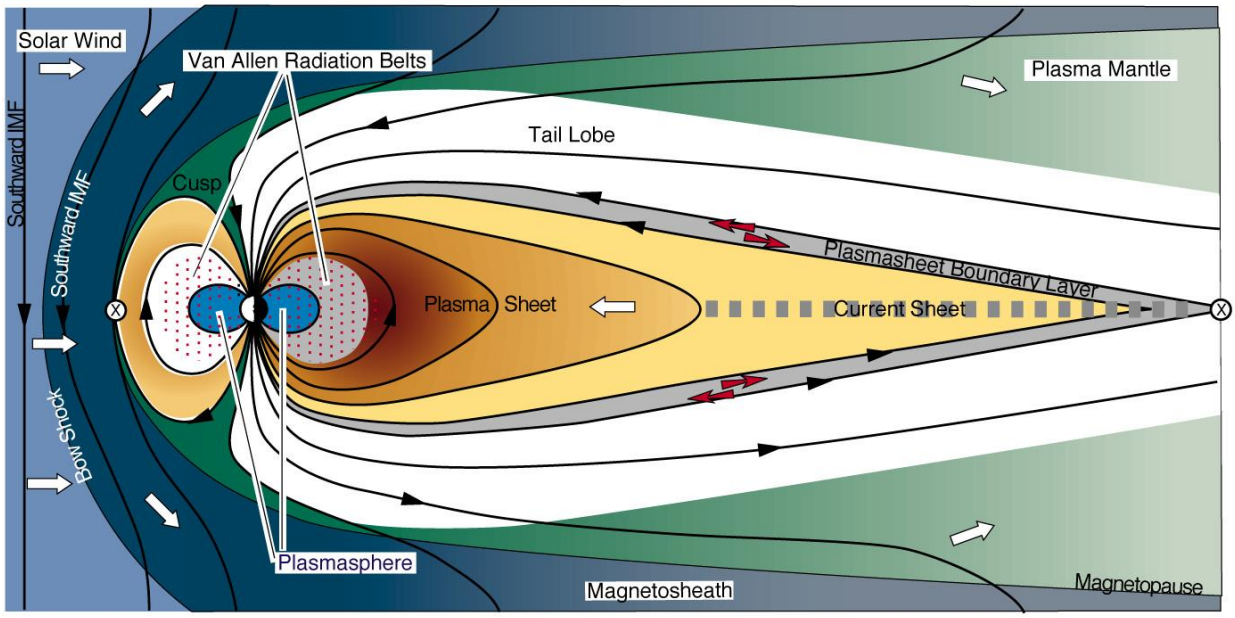

Figure 1.1. Schematic of the Earth's magnetosphere, with principal particle regions [Rice Space Institute Server, adapted from T. W. Hill].

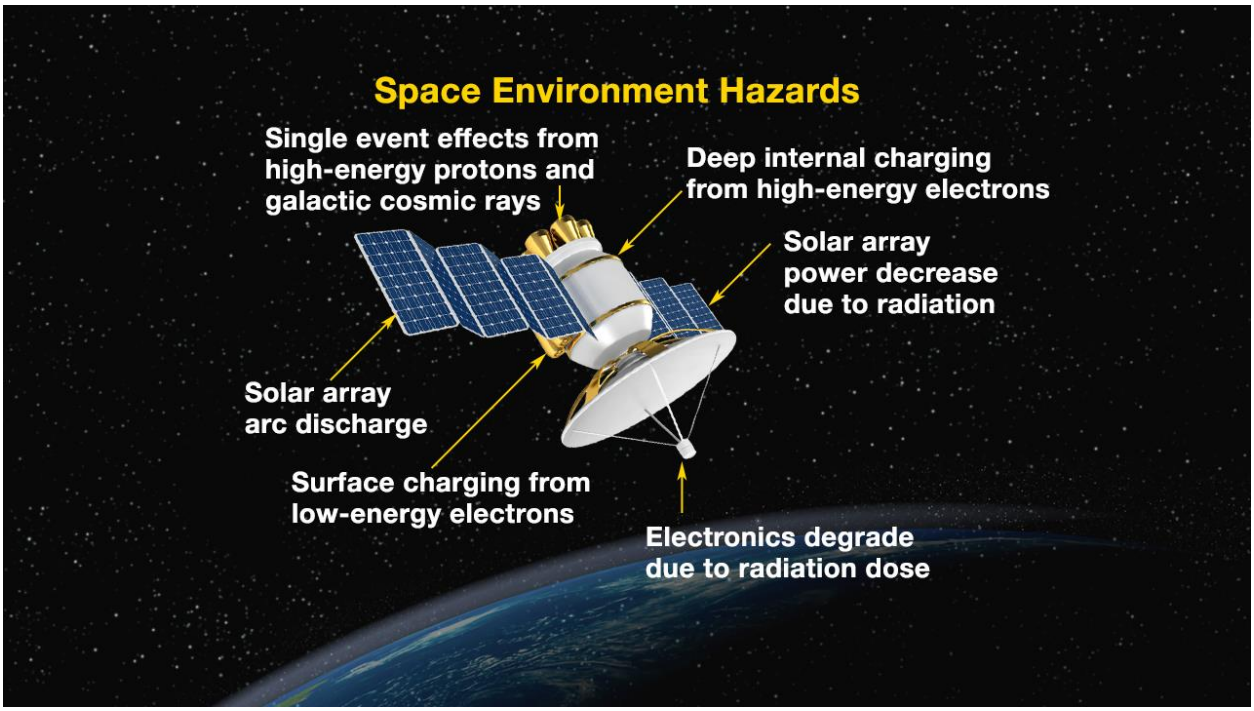

Figure 1.2. Various types of satellite anomalies caused by high levels of charged particles [NASA. Credit: JHUAPL].

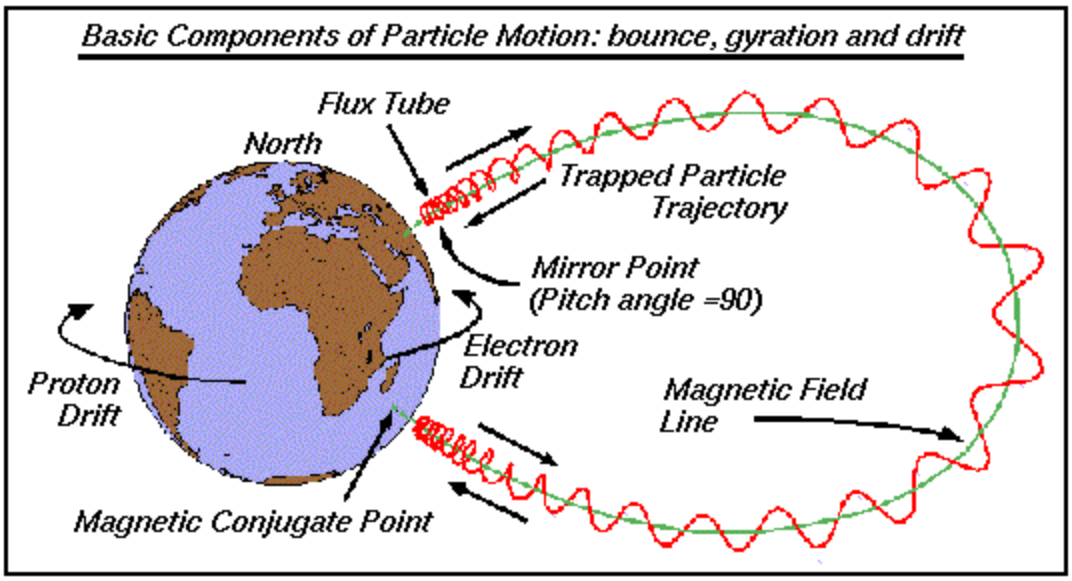

Figure 1.3. Three basic components of particle motion in the inner magnetosphere [NASA].

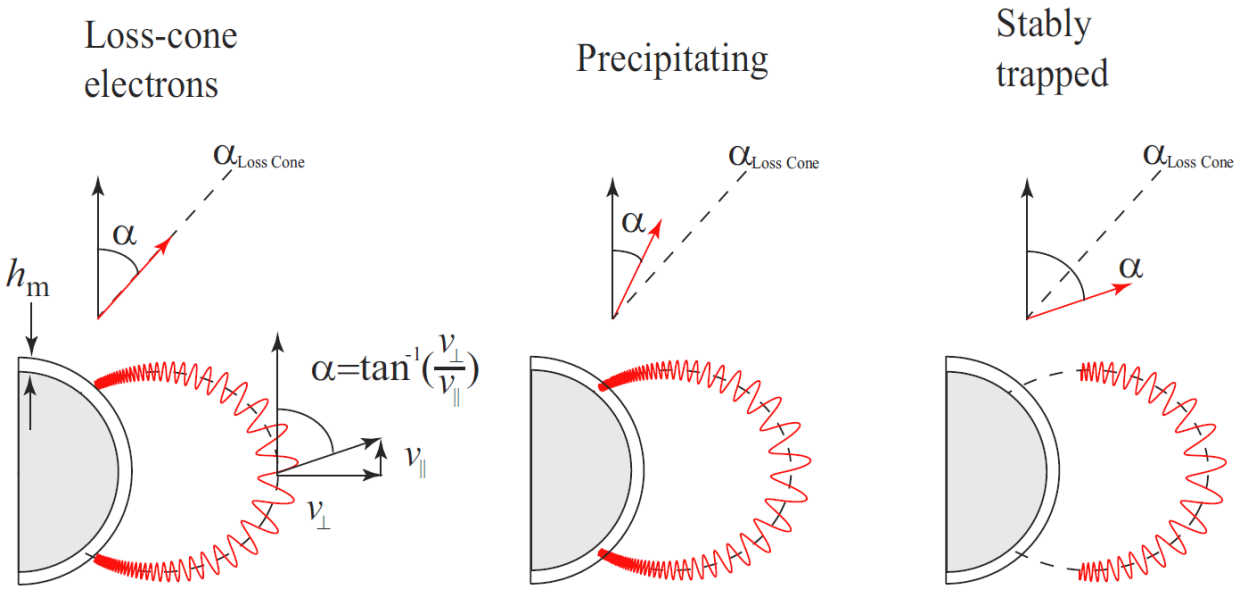

Figure 1.4. The relation of mirror height to the equatorial pitch angle, and the concept of a loss-cone angle [Figure 2.8 in *Bortnik*, 2004].

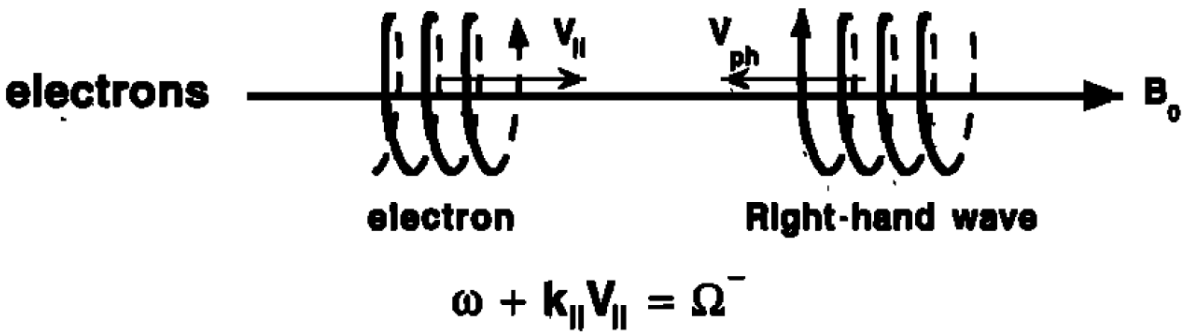

Figure 1.5. Normal first-order cyclotron resonance between electromagnetic circularly polarized waves and charged particles [Figure 8 in *Tsurutani* and *Lakhina*, 1997].

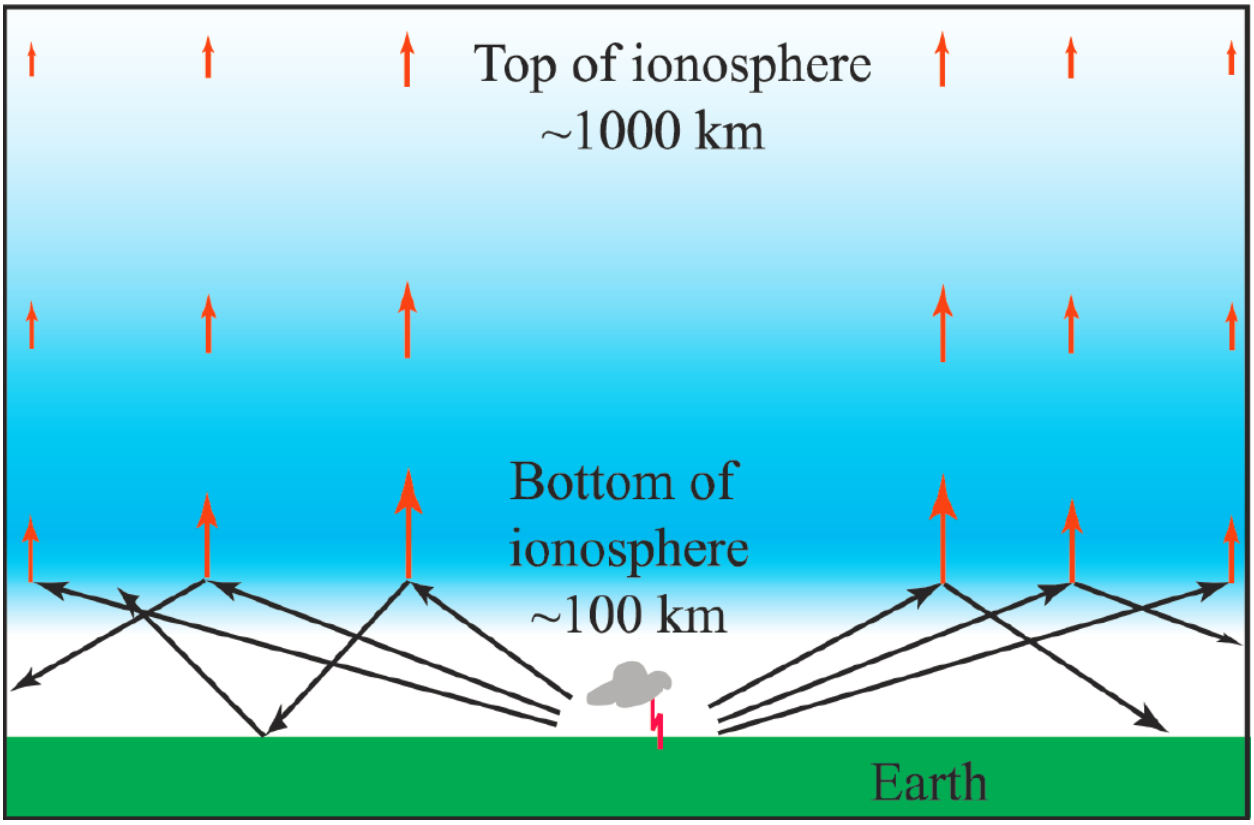

Figure 1.6. Illustration of a lightning discharge radiating ELF and VLF waves that propagate away from the source in the Earth-ionosphere waveguide and leak into the magnetosphere [Figure 1.2 in *Bortnik*, 2004].

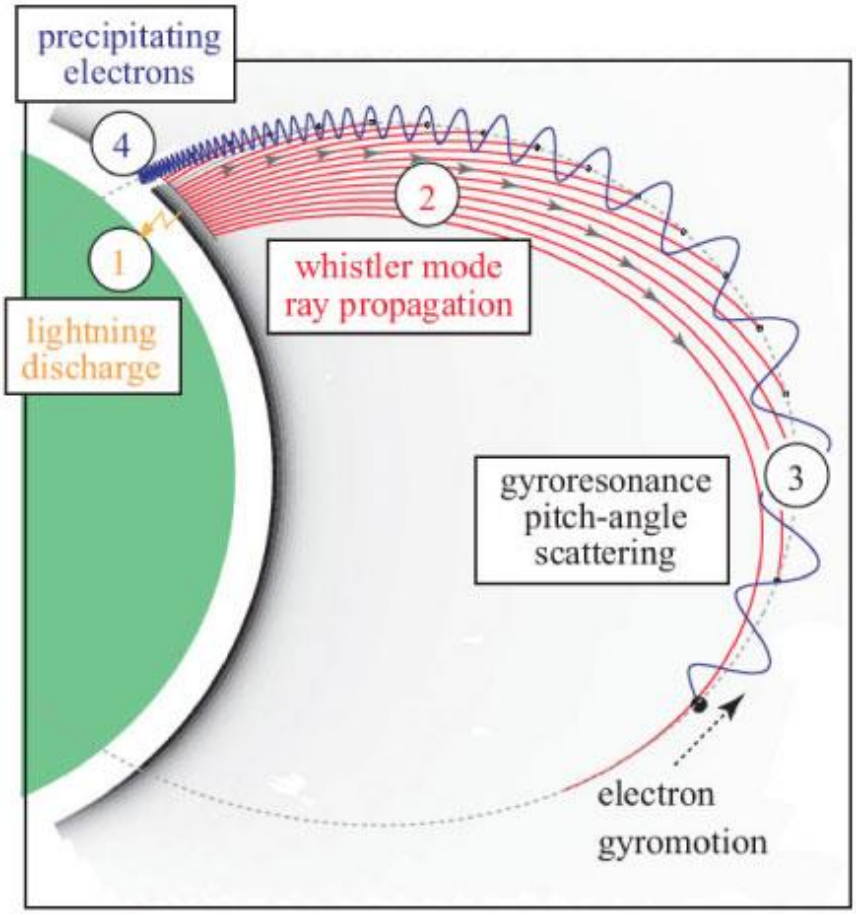

Figure 1.7. Illustration of the lightning-induced precipitation process [Stanford VLF Group website].

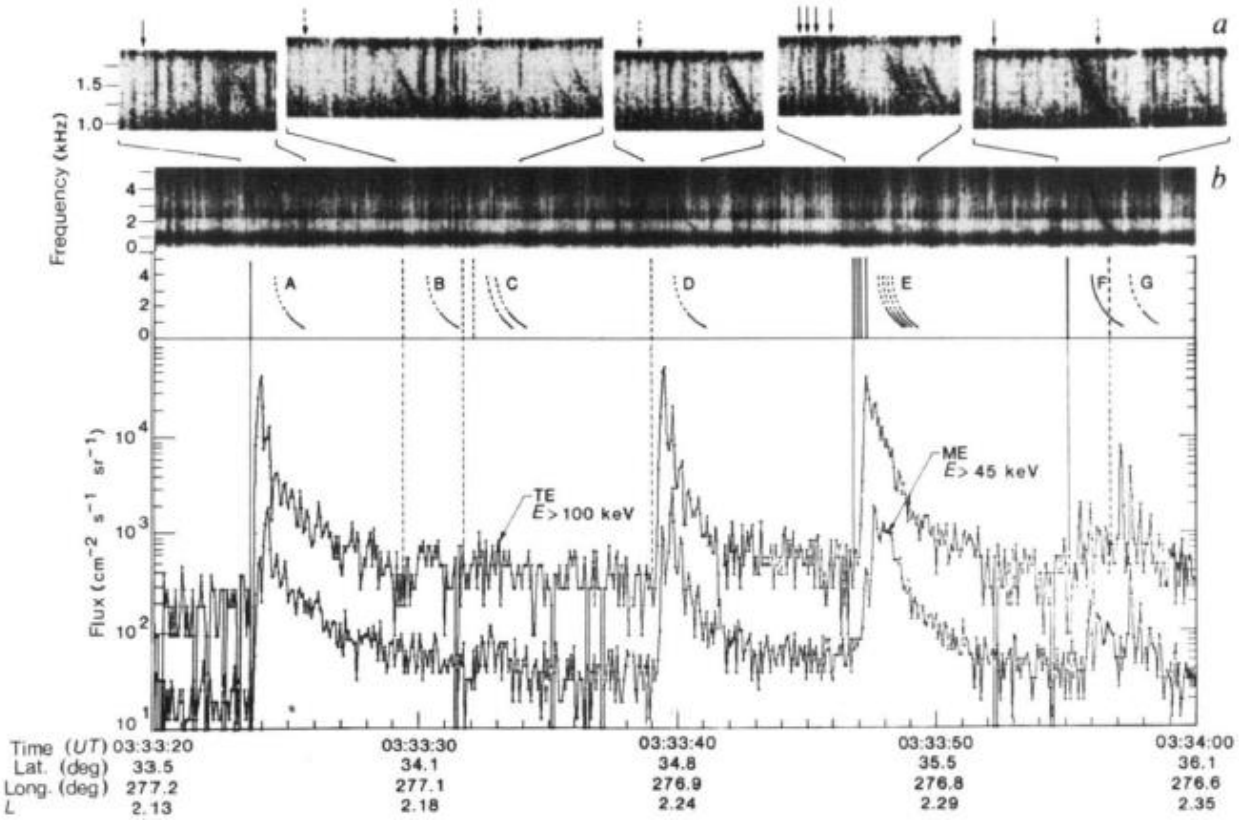

Figure 1.8. Observations of sferics (top), whistlers (middle) and electron flux bursts (bottom) in LEP events [Figure 1 in *Voss et al.*, 1984].

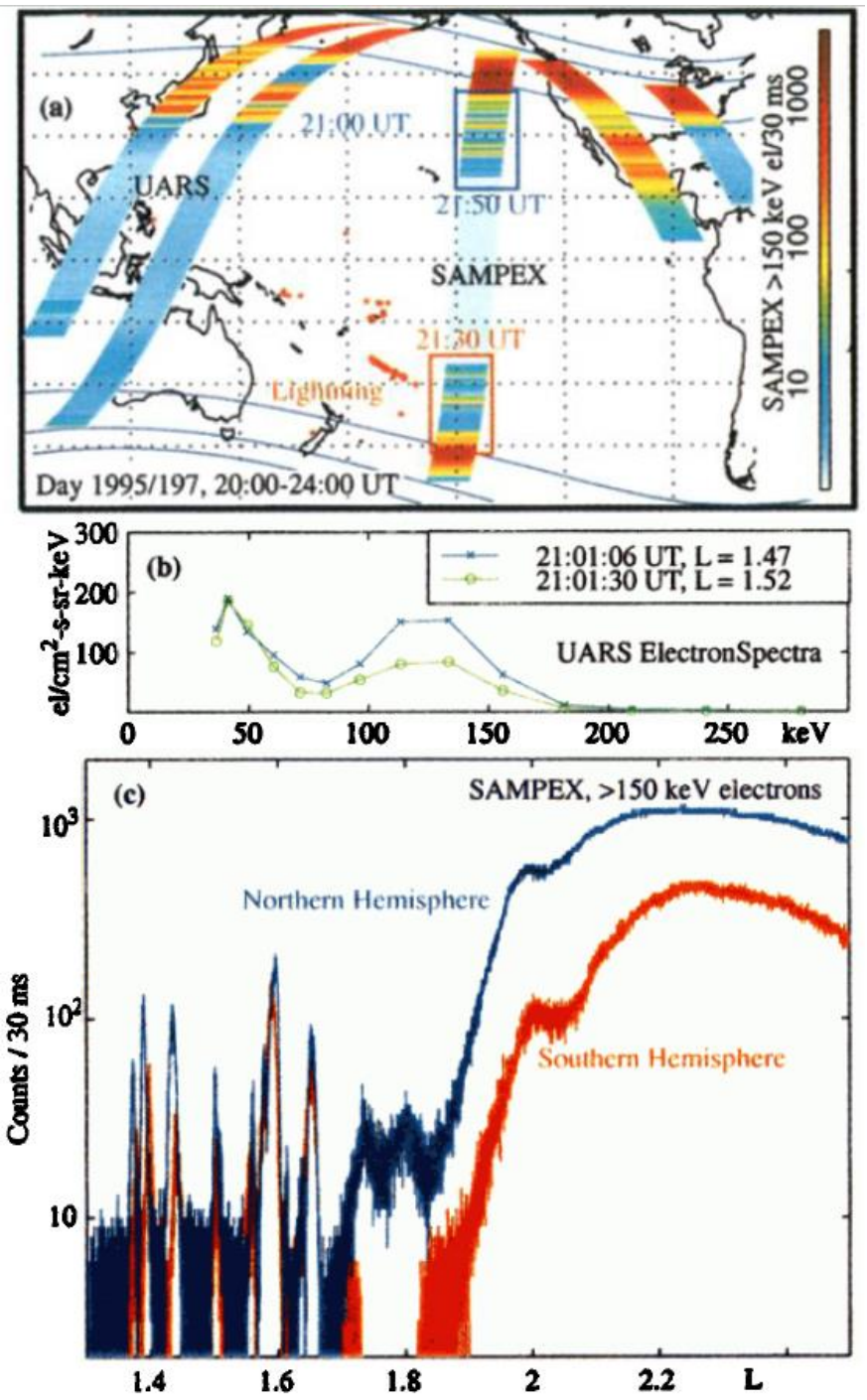

Figure 1.9. Observations of drift loss cone event. (top) Drift loss cone electrons observed on board SAMPEX and UARS are plotted in spectrogram format on their orbital tracks. (middle) Electron spectrum at UARS. (bottom) electron precipitation over different L-shells [Plate 5 in *Blake et al.*, 2001].

Chapter 2. A STATISTICAL STUDY OF WHISTLER WAVES OBSERVED BY VAN ALLEN PROBES (RBSP) AND LIGHTNING DETECTED BY WWLLN

This chapter is published as:

Zheng, H., R. H. Holzworth, J. B. Brundell, A. R. Jacobson, J. R. Wygant, G. B. Hospodarsky, F. S. Mozer, and J. Bonnell (2016), A statistical study of whistler waves observed by Van Allen Probes (RBSP) and lightning detected by WWLLN, J. Geophys. Res. Space Physics, 121, 2067–2079, doi:10.1002/2015JA022010.

2.1 INTRODUCTION

Previous observations of energetic electron flux indicate that the Earth's radiation belts are distributed in two distinct zones separated by a region of depleted flux called the slot [e.g., *Horne et al.*, 2003, Figure 2]. The structure of the inner zone ($L < 2$) tends to be relatively stable, in comparison to the outer zone ($L \geq 3$), which is highly dynamic [*Millan and Thorne*, 2007]. Over the past few decades, it has been shown that this difference is primarily related to the source and loss mechanisms that control radiation belt electrons. It is believed that in the inner magnetosphere, pitch angle scattering (including both Coulomb collisions and resonant scattering by whistler-mode waves) controls the loss of energetic electrons [*Abel and Thorne*, 1998a, 1998b]. Coulomb collisions with atmospheric constituents are the dominant loss process for energetic electron ($E \geq 100$ keV) inside $L = 1.3$ [Walt and MacDonald, 1964; Abel and Thorne, 1998a]. Above $L = 1.3$, the long-term energetic electron population is largely controlled by whistler mode waves, including plasmaspheric hiss, lightning-generated whistlers, and man-made transmitter signals. The calculations in *Abel and Thorne* [1998a] suggest that all three types of whistler mode waves

may play important roles in the loss of energetic electrons, but different types of whistler mode waves may interact with different electron energies and be dominant at different L shells. Specifically, the lightning-generated whistlers, which are the concern of this work, are suggested to become important at L = 2.0, provide the dominant scattering process at L = 2.4 and still make a contribution at L = 3.2 [*Abel and Thorne*, 1998a]. Recent studies have also shown that whistler mode chorus wave can provide local acceleration of energetic electrons by efficient energy diffusion in the outer radiation belts [e.g., *Summers et al.*, 2002; *Meredith et al.*, 2003b; *Li et al.*, 2014]. It has also been shown that intense whistler mode chorus emission may cause microburst electron precipitation into the atmosphere [*Thorne et al.*, 2005].

Previous studies have shown that whistlers play an important role in the dynamics of the radiation belts and are partly responsible for the loss of the energetic electrons [e.g., *Dungey*, 1963; *Voss et al*., 1984, 1998; *Abel and Thorne*, 1998a, 1998b; *Lauben et al*., 2001; *Rodger et al.*, 2004; *Millan and Thorne*, 2007; *Meredith et al.*, 2009]. Pitch angle scattering of energetic Van Allen belt electrons by whistlers can result in the precipitation of these electrons into the atmosphere [*Dungey*, 1963]. Lightning-induced electron precipitation (LEP) from the Earth's radiation belts, caused by whistler wave-particle interaction, is a known troposphere-to-magnetosphere coupling mechanism. The first satellite measurements of LEP events were obtained as a result of the SEEP experiment on S81-1 satellite [*Voss et al.*, 1984]. By using the same data, *Voss et al.* [1998] found that a single LEP burst (10^{-3} erg s^{-1} cm^{-2}) in the slot region is estimated to deplete ~0.001% of the particles in the region. Whistlers can be important for pitch angle diffusion of 100 – 250 keV electrons in the $2 < L < 3$ range [*Voss et al*., 1998]. *Rodger et al*. [2004] provide evidence for the relative significance of the electron losses driven by whistler-induced electron precipitation and that caused by VLF transmitters. Magnetospherically reflected whistlers generated by lightning

are also considered to be a source of plasmaspheric hiss [*Sonwalkar and Inan*, 1989]. By using ray-tracing simulations, it was shown that whistlers produced by a single lightning flash, but entering the magnetosphere at different points, can form a continuous hiss-like signal at a fixed point [*Draganov et al.*, 1992]. The analysis of DE-1 and IMAGE data showed that the geographic distribution of hiss over the ~500 Hz to ~3 kHz frequency range is similar to the geographic distribution of lightning strokes [*Green et al.*, 2005]. Similar results are shown in the analysis of CRRES data for the plasmaspheric hiss at higher frequencies $f > 2$ kHz [*Meredith et al.*, 2006].

Plasmaspheric electron densities are an important and fundamental parameter in the dynamics of Earth's radiation belts. The propagation of whistlers in the plasmasphere is strongly connected with cold electron density. Whistler data from ground-based stations were used to identify the large-scale electron-density irregularities in the plasmasphere [*Park and Carpenter*, 1970] and also to present a statistical study of equatorial plasmaspheric electron density and associated flux tube electron content [*Park et al.*, 1978]. Understanding the link between lightning activities and whistler observations on satellites may assist in estimating of plasmaspheric electron densities and testing of magnetospheric models of electron density and energy distribution [*Liemohn and Scarf*, 1964].

The broadband radio waves produced by lightning discharge, called "sferics," can propagate in the Earth-ionosphere waveguide and be detected thousands of kilometers away from the source. A portion of the sferics can penetrate into the ionosphere, coupling with the whistler mode in the very low frequency (VLF) band, and travel upward obliquely within tens of degrees along the geomagnetic field line [*Helliwell*, 1965]. The source and the destination of lightning-generated whistlers have been studied for years. Early in situ rocket-borne measurements demonstrated the one-to-one connection between whistlers observed in the upper atmosphere/ionosphere and

individual lightning strokes from specific thunderstorms within 1000 – 2000 km [e.g., *Holzworth et al.*, 1985, 1999; *Kelley et al.*, 1990; *Li et a*l., 1991]. SCATHA satellite VLF data indicated that whistlers are rarely detected near the magnetic equator across the L shells of L = 5.5 – 9.0 [*Koons*, 1985]. The apparent scarcity of whistlers near geostationary altitude as covered by the SCATHA satellite, suggests that there may be few if any propagation paths from the Earth-ionosphere waveguide to the outer regions of magnetosphere. But it also may indicate that VLF spectral data are not always investigated with high enough time resolution to easily detect lightning whistlers. *Gurnett and Inan* [1988] examined the data from the DE spacecraft and discovered several lightning whistlers up to 15 kHz or even 25 kHz at L < 4 [*Gurnett and Inan*, 1988, Figures 21–23]. *Holzworth et al.* [1999] used a global three-dimensional two-fluid code to investigate the propagation of whistlers at 0.5, 1, and 2.0 kHz into the high-latitude magnetosphere. The results show that with southward interplanetary magnetic field, the energy of whistlers which start from magnetic latitude above 70° can propagate to near magnetopause or high-altitude magnetosphere. In recent decades, localized and global ground lightning detection networks have been gradually improving, which has proven critical in linking whistlers to their source lightning strokes. *Santolík et al*. [2009] analyzed three lightning strokes detected by METEORAGE, sferics received by Nançay station, and the corresponding whistlers observed by the DEMETER satellite at 707 km altitude. The electric field data and optical flashes measurements on the C/NOFS satellite were used with simultaneous global lightning location information from WWLLN in *Holzworth et al*. [2011] to show that whistlers have abundant access to the ionosphere, even close to the magnetic equator. Both papers showed that the one-to-one coincidence between whistler waves observed at LEO and individual lightning strokes and the penetration into the topside ionosphere occurs at nearly vertical wave vector angles due to the gradient of electron density. *Fiser et al.* [2010] used

two reference samples to automatically detect the fractional hop whistlers on the DEMETER satellite. A local lightning detection network in Europe was used to match the lightning and whistler data. They found that the amplitudes of whistlers decrease monotonically with horizontal distance up to ~1000 km from the source lightning and the amplitude of whistlers are stronger at nighttime than during the daytime. In this paper, we will explore the connection between lightning sferics and whistlers by using data from the Van Allen Probes (formerly known as the Radiation Belt Storm Probes (RBSP)) and World Wide Lightning Location Network (WWLLN). The high-resolution waveform data obtained near the geomagnetic equator provide a wider area coverage in the inner magnetosphere than LEO satellites like DEMETER. Global lightning data, including the location, time, and energy for every individual stroke, are simultaneously collected in the conjunction periods. One-to-one coincidences between whistlers observed by RBSP and lightning strokes detected by WWLLN are explored in this work.

2.2 RBSP AND WWLLN

The RBSP satellites were launched in August 2012 into a near-equatorial orbit with 10° inclination, apogee altitude of 30,050 – 31,250 km (~5.8 R_E from the center of the Earth) and perigee altitude of 500 – 675 km [*Stratton et al.*, 2013]. These constraints place the satellites in orbits that cut through both the inner and outer radiation belts. After launch the satellites were officially renamed to the Van Allen Probes. The fundamental purpose of the RBSP mission is to provide a better understanding of the processes that drive changes within the Earth's radiation belts. The Electric Field and Waves (EFW) instrument [*Wygant et al.*, 2013] on the RBSP can provide both 3-D electric field and 3-D magnetic field waveform data. The burst mode data we used in this work have a sampling rate of 16.4 ksamples s^{-1}. Another instrument called RBSP-EMFISIS (The Electric and Magnetic Field Instrument Suite and Integrated Science) [*Kletzing et al.*, 2013] can

also provide 3-D electric and magnetic field waveform data with a sampling rate of 35 ksamples s^{-1} in 6 s blocks. The burst mode of EMFISIS can be trigged automatically or manually.

WWLLN is a global very low frequency lightning-location system using the time-of-group-arrival (TOGA) technique [*Dowden et al.*, 2002]. It can detect both cloud-to-ground (CG) and intracloud (IC) lightnings, but the type of lightning is not distinguished in the data. At present, WWLLN includes over 70 participating stations. This network improves in accuracy and detection efficiency with increased number of stations. The number of lightning strokes located increased from 10.6 million to 28.1 million (~165%) when the number of WWLLN stations increased from 11 in 2003 to 30 in 2007 [*Rodger et al.*, 2009]. As of 2011 the network had an estimated detection efficiency of about 11% for CG lightning over the continental United States, and the number can increase to >30% for higher peak current lightning [*Hutchins et al.*, 2012]. Knowledge of individual stroke locations, with high temporal and spatial accuracy, is very helpful for studying VLF energy radiation and the global electric circuit [e.g., *Hutchins et al.*, 2013, 2014].

This paper presents data collected during two periods of conjunction work, from July to September 2013 and from March to April 2014, during which we were able to collect specific burst mode RBSP data. The conjunction work of 2013 between WWLLN and RBSP began on 1 July 2013 and ended on 15 September 2013. The following study period started on 15 March 2014 and ended on 30 April 2014. For each day of the two time periods, a prediction was computed in advance, to determine the best times to collect the broadband wave data. Burst mode sampling was conducted during the predicted time for each satellite. In addition to the statistical study conducted in this work, we also provide some examples from other burst mode sampling intervals when high L shell whistlers were seen.

2.2.1 *Prediction*

Due to the limit of data storage onboard and in agreement with the RBSP instrument team, the burst mode for this lightning study at 16.4 ksamples/s on RBSP-EFW was limited to 10 min per day per satellite (in 2014, only RBSP-B was available for the data collection). Additionally, due to data download limitations, everyday we had to select 3 or 4 min out of the 10 min stored broadband data, which were then downloaded. In order to predict the best 10 min/d to collect high sampling rate burst mode data on RBSP satellites, we traced the satellite magnetic footpoints over a lightning occurrence map. The footpoints data were calculated at an altitude of 100 km using the T89c magnetic field model developed by *Tsyganenko* [1989] and is provided by the SSC 4D Orbit Viewer from NASA (http://sscweb.gsfc.nasa.gov/tipsod/). This lightning occurrence map is composed of all global WWLLN lightning data from the same date in the last 3 years (2010 – 2012). That is, we used 3 weeks of data, 1week from each of the last 3 years, centered at the day of the year for which we want a prediction. This map therefore had global lightning data from 21 days. We then used the predicted satellite ephemeris with 1 min time resolution to identify the magnetic field footpoints in both Northern and Southern Hemispheres. From previous research [*Santolík et al.*, 2009; *Fiser et al.*, 2010; *Holzworth et al.*, 2011], we know that the entry point of whistlers into the ionosphere can be thousands of kilometers away from the source lightning. In our work, a source area of 20° × 20° box was used in the prediction instead of a circle with ~1000 km radius in order to get a faster calculation in the program. Although the area of 20° × 20° box is not the same at different latitudes, the predicted peaks will not change significantly because the results are dominated by the variance of lightning occurrence rate at different latitudes. In our prediction, for every 1 min footpoint location, we summed all lightning strokes within the 20° × 20° box centered at the footpoint. This gave us a 1 min resolution prediction of possible strokes at

the magnetic footpoint for the whole day. Figures 2.1a and 2.1b show the prediction results for RBSP-A and RBSP-B on 17 July 2013 as an example. The blue lines represent the prediction result using WWLLN data from 2010 to 2012 and the red lines represent the real lightning number in the same footpoint box using actual WWLLN data on 17 July 2013. The time difference between prediction peak and actual peak is within 5 min for both satellites. If this example is true in general, it would suggest that if we set a time period with ±5 min centered at the predicted peak time, there should be lightning strokes detected around the footpoints within the predicted 10 min. The conjunction work between WWLLN and RBSP started in July 2013 after the prediction test for the whole month of June was finished. For RBSP-A and RBSP-B, 93.3% and 96.7% of daily time shifts between actual peak and prediction peak are within 5 min. Even on days when the time difference between the actual and predicted peaks is larger than 5 min, there are still many lightning strokes detected during the predicted 10 min period. After the RBSP burst mode sampling on the satellites was finished, we checked the actual WWLLN lightning stroke numbers detected within the 20° × 20° box for every 1 min footpoint location and selected the best 3 – 4 min to download everyday.

2.2.2 *Dechirping*

Figure 2.2 shows a 1s spectrogram and waveform plot of the RBSP-A observation on 17 July 2013 during 18:27:20.5 – 18:27:21.5 UT period. Figure 2.2a shows the power spectral density (PSD) of Bu component (UVW coordinate system is the spacecraft coordinate system, where the W axis is the spin axis and is orthogonal to U and V axis). In Figure 2.2a, at least five intense whistler events are detected and identified by numbered oblique arrows. There are also some weak events shown as unnumbered vertical arrows in Figure 2.2a. The original waveform data of Bu is shown in Figure 2.2c. Figure 2.2e shows the lightning strokes detected by WWLLN in the 20° × 20° box centered

at the footpoint. The lightning strokes detected in the first half second are shown as dashed vertical lines in Figures 2.2a – 2.2d. From the original data (Figures 2.2a and 2.2c), it is difficult to determine whether there is an actual one-to-one coincidence between the lightning detected by WWLLN and whistlers observed by RBSP-A or if they are actually unrelated events that happened to be observed simultaneously. In the ionosphere at low latitude and midlatitudes, the time delay of a whistler approximately varies as $D/\sqrt{f}$, where f is the wave frequency and D is the dispersion constant. *Jacobson et al.* [2011] developed an automated algorithm called "dechirping" for recognizing and selecting the signatures of electron whistlers observed on C/NOFS satellite. Here we employ this method to identify the best dispersion constant between 0 and 400 in each analysis window (detailed definition described in *Jacobson et al*., 2011, section 4.1 and equation (1)). In the final step, we shift different frequency parts of waveform back to the arrival time by using the best fit to $D/\sqrt{f}$ for each time interval. Figures 2.2b and 2.2d are the dechirped results for the data in Figures 2.2a and 2.2c. In Figure 2.2b, the whistlers detected in Figure 2.2a have been corrected for the time delay and are no longer dispersed. Instead, the whistler energy is now sharpened in the vertical red bars between 1 kHz and 8 kHz. In order to reduce the contribution of noise below the waveguide cutoff and alias effects around the Nyquist frequency, low (1 kHz) and high (8 kHz) cutoff frequencies were applied before the dechirping process. After the dechirping process, the vertical dashed lines (WWLLN lightning time) and vertical red bars (dechirped whistler time) are located quite close in time. The dechirping method enables us to identify even low-intensity whistlers from background noise. The two weak signals in Figure 2.2a (vertical arrows) become much more prominent in Figure 2.2b (also vertical arrows). The dechirping process also makes it possible to identify overlapping whistlers. Using the Number 3 whistler in Figure 2.2a as an example, we see it contains two to three whistler traces observed at almost the same time. In Figure

2.2d, the number 3 event clearly resolves as several independent dechirped whistler packets which are shown in the dechirped waveform. Considering the leftward migration of signal energy in the dechirping, a 50% overlap between the time windows was applied. We only compared the lightning strokes and dechirped peaks in the first half second because the dechirped peak near the end of the observation window may not be accurate since only the high-frequency packet of whistler waveform underwent the dechirping process. In Figure 2.2, all six lightning strokes (in first 0.5 s) detected in the 20° × 20° box centered at the footpoints correspond to whistler signals observed by RBSP-A. The correspondence between Number 5 whistler and WWLLN lightning stroke is also good and can be identified in the next time window. There is still a small time-difference between the dechirped waveform peak and WWLLN lightning time because we have not yet accounted for the propagation time.

2.2.3 *Propagation Model*

WWLLN provides lightning stroke location with better than 15 μs temporal accuracy and 10 km spatial accuracy [*Jacobson et al.*, 2006]. We assume that the VLF sferics generated from lightning strokes propagate in the Earth-ionosphere waveguide to the footpoint of satellites with a speed slightly less than c [*Dowden et al.*, 2002] (where c is the speed of light in a vacuum). Near the footpoint they couple with the plasma and propagates obliquely along the geomagnetic field to the RBSP satellites according to the oblique whistler dispersion relation. This type of propagation process has been used extensively in previous work [e.g., *Holzworth et al.*, 1999; *Jacobson et al.*, 2011]. It is based on the quasi-longitudinal approximation to the Appleton-Hartree dispersion relation [*Helliwell*, 1965].

To compare the WWLLN lightning stroke time with the dechirped peak time from RBSP, we subtract two terms from the dechirped peak time. The first is the speed of light propagation time

along the geomagnetic field line from the footpoint to the satellites. Here we used IGRF-11 model in the Geopack DLM to trace the geomagnetic field and calculated the length of the geomagnetic field line. The second term is the propagation time in the Earth-ionosphere waveguide from WWLLN lightning stroke to the footpoint of RBSP satellites. After subtracting the two terms on the dechirped peak time, the whistler is effectively transported back to the possible candidate of source lightning. We call it the "corrected" dechirped peak time in this paper.

2.2.4 *One-to-One Coincidence Between WWLLN and RBSP*

The goal of this paper is to find possible one-to-one coincidences between lightning and whistlers by comparing the WWLLN lightning time and corrected dechirped peak time from RBSP. For all the continuous burst mode data, we divided Bu component into several analysis windows. Each window includes 16,384 samples (1 s) and 50% overlapping (8196 samples). Every 1 s window was then extended to a 2 s window by adding another 16,384 empty data just before the Bu data, in order to leave enough space for the leftward migration of the signal during the dechirping process. Every new 2 s window was fed into the dechirping process, and all dechirped peaks between 1 s and 1.5 s were saved for later analysis except for the first and last window (the dechirped peaks of first and last window were searched from 0 s to 1.5 s and from 1 s to 2 s, respectively). Once there was at least one dechirped peak found in the analysis window, we loaded the WWLLN lightning data detected in the same 2 s analysis window as the source candidates for the dechirped peaks. At the same time, the footpoint with shorter arc distance (spherical distance between one of the footpoint to lightning location) to each lightning stroke was selected from two hemispheres and used to correct the dechirped peak. The time differences between source lightning candidates and corrected dechirped peaks in the same analysis window were calculated, and the histogram results are shown in Figure 2.3. We have already shown that the time difference between

WWLLN lightning and dechirped peak is usually a few milliseconds in Figure 2.2, so only time differences between −100 ms and 100 ms are plotted here. Figure 2.3a shows a histogram of the time difference between corrected dechirped peak and WWLLN lightning ($t_{corrected} - t_{WWLLN}$) in 1ms bin, for all stroke locations. Figures 2.3b and 2.3c are similar but only include WWLLN stroke locations within 10,000 km and 2000 km away from the nearest footpoint. In Figures 2.3a – 2.3c, a clear peak of match numbers is located between -30 ms and 0. There are several possible reasons for the time difference. The first reason is the uncertainty of the dispersion constant. Take a whistler observed on 5 August 2013 as an example. In the 236th analysis window with a dispersion constant of 220.5 $s^{1/2}$, the dechirped peak was located at 20:00:58.748679. (This peak was located in the 1.5 s to 2 s of 236th window, so it was not saved here but would be saved in the 237th window.) While in the 237th analysis window with a dispersion constant of 208.0 $s^{1/2}$, the same peak was located at 20:00:58.761069 instead (12.39 ms difference). The second reason is the uncertainty of two subtracted propagation terms. Waveguide and field line arc lengths are calculated from models, which also generated errors. Finally, the errors may be introduced by the propagation model, since it may not work perfectly for all latitudes (L shells).

The maximum absolute value of time difference above the "noise" level between corrected dechirped peak and its WWLLN source was found to be around 30 ms in Figure 2.3. By using this number, an automatic one-to-one coincidence search was applied to the whole data set. For every dechirped peak, we loaded global WWLLN lightning data, corrected the dechirped peak time, and then found the one-to-one coincidence with time difference from -30 ms to 0.

2.3 Statistical Results

During the conjunction work in 2013, we downloaded 192 min over 65 separate days from RBSP-A and 192 min over 66 days from RBSP-B. In 2014, we downloaded 221 min over 39 days only

from RBSP-B. In total, we collected 605 min of data across 170 distinct days for RBSP-A and RBSP-B. In July 2013, no special selection criteria were used, so the burst mode period was biased toward the low-latitude region, where lightning is most prevalent. For the highly eccentric RBSP orbit, low satellite altitude always corresponds to low L shell. Figure 2 in *Rodger et al.* [2004] showed that the lightning activity may reach to the high L shell region in the summer of the Northern Hemisphere. From August 2013 to September 2013, the prediction was changed to focus on the footpoints region with geographic latitude larger than 40°, which is poleward of the regions with highest lightning activities.

Figure 2.4 shows the L shell coverage of RBSP data used in our work. As mentioned before, the burst mode sampling period is only requested when it includes the peak number of strokes in the daily prediction. For July 2013, the best prediction time occurred when the satellites were conjugate to low-latitude regions where lightning is most prevalent (Figure 2.4a). Thus, during the first period (July 2013), whistler observations were only made at low L shells. Beginning in August 2013, our focus shifted to the region with geographic latitude larger than 40°. In August and September 2013, the L shell values of satellite footpoints were therefore significantly higher than in July 2013 (Figure 2.4b). Most of the data in this period were sampled between L = 2 and 3. There are 780 s (13 min) of data sampled at $L \geq 5$ region. In March and April 2014, the L shell value coverage returned to $L < 2.5$ due to the seasonal change of global lightning (Figure 2.4c). Figure 2.4d shows the global coverage of the satellites footpoints when whistlers were observed by RBSP satellites. All of the dechirped peaks are observed inside of L = 3. The data mainly cover four regions, with three small portions located at 100° – 130°, 170° – 220°, and 230° – 250°, and a large region located at 310° – 40°. These are approximately corresponding to Europe/Africa, Asian, Oceania, and America, respectively. In Figure 2.4d, the longitude coverage is limited in

several parts because lightning has a higher occurrence rate on continents than over oceans. Figure 2.4e shows the distribution of lightning strokes that are one-to-one coincident with whistlers observed by RBSP satellites. Figure 2.4d refers to the L value of the RBSP satellites during whistlers observation, while Figure 2.4e refers to the L value of the lightning source location. In Figure 2.4e, the matched lightning strokes show full coverage of all geomagnetic longitudes and have peak numbers around the same regions of dechirped peaks in Figure 2.4d. There are some lightning strokes at high L shell, larger than L = 3 in Figure 2.4e, which are the sources of whistlers observed by RBSP inside of L = 3 in the magnetosphere. This means the distance between lightning and satellite footpoint may be larger than 1000 – 2000 km, which is consistent with previous research [e.g., *Holzworth et al.*, 1999].

Table 2.1 shows the statistical results of both RBSP-A and RBSP-B. The total of 605 min data are divided into three periods: 151 min in July 2013, 233 min in August and September 2013, and 221 min in March and April 2014. Whistlers are observed in 485 min (80.2%) of data, with 140 min (92.7%), 150 min (64.4%), and 195 min (88.2%) in the three periods, respectively. A total number of 20,986 whistlers are observed by RBSP satellites. The 8308 (39.6%) of them are one-to-one coincident with WWLLN lightning strokes. Specifically, 2526/5938 (42.5%), 730/2454 (29.7%), and 5052/12,594 (40.1%) of the observed RBSP whistlers are one-to-one coincident with WWLLN lightning strokes in the three periods. In the 485 min, 206,470 lightning strokes are detected by WWLLN. Four percent of them are found to be one-to-one coincident with whistlers observed on RBSP. If we narrow the lightning locations to the area within 2000 km from the footpoints, there are 38,777 lightning strokes detected in the 485 min, and 15.3% of them are one-to-one coincident with whistlers observed on RBSP.

2.4 DISCUSSIONS

As explained in the Section 2.1, previous studies found that whistlers play a significant role in the dynamics of the radiation belts. But the connection between source lightning strokes and subsequent whistlers in the magnetosphere has been difficult to study due to lack of simultaneous, high time resolution waveform and global lightning observations. In this paper we present a new data set that identifies the source lightning locations for specific whistlers in the inner magnetosphere with the help of WWLLN and RBSP. Unlike *Fiser et al.* [2010], the lightning data used in our work are not simply narrowed to the region near the footpoints of satellites. Additionally, we do not use reference whistlers to automatically detect whistlers since the dispersion factor may change at different regions. The final difference between two studies is the propagation of whistlers. At low altitude, the main propagation process happens in the Earth-ionosphere waveguide between footpoint and source lightnings. While in the inner magnetosphere, the whistlers travel a long path along (or within some angles of) field lines till they are observed by satellites. We did not compare the amplitude of whistlers with horizontal distance or the amplitude of whistlers between day and night, like what *Fiser et al.* [2010] did, in this paper. The propagation model used in this work is quite simple and does not include the various propagation mechanisms of whistlers in the magnetosphere. Whether whistlers are ducted or non-ducted remains an outstanding question. Although lightning is considered the only source for whistlers, the observed one-to-one coincident rate between whistlers and lightning is much less than 100%. This rate is limited by lightning detection efficiency, the strength of whistlers, and how well we understand the propagation of whistlers.

In this work, we used the WWLLN lightning location data from 2010 – 2012 to forecast the lightning activity along the daily trajectory of RBSP footpoints. Then we recorded the 10 min of

RBSP burst mode data for the time period with peak lightning stroke counts in the 20° × 20° grid centered at the footpoint. After onboard recording, we were only able to download 3 – 4 min (of the daily 10 min recording). During the entire 605 min of downloaded data, whistlers are observed 80.2% of the time we predicted, suggesting that satellites should have a high probability of observing whistlers if their footpoints are located within a few thousand kilometers of an active thunderstorm. The occurrence of these high lightning activity areas can be predicted by using archival WWLLN data. We can use the results of this method to predict the occurrence of lightning-generated whistler waves in the inner magnetosphere and its related phenomena.

In the 485 min of data, 20,986 dechirped peaks are observed by RBSP satellites. 39.6% of those peaks are one-to-one coincident with a WWLLN lightning stroke. It is obvious that WWLLN does not detect the source lightning for every whistler observed by RBSP satellites. It is found that WWLLN only has a 20 – 40% detection efficiency for strong CG lightning (peak current larger than 55 kA) [*Rodger et al.*, 2009; *Abarca et al.*, 2010], so the possible source lightning may be missed by WWLLN. A test was also undertaken to evaluate the probability that we might match whistlers with some noncorresponding lightning due to the high occurrence rate of global lightning. During the 485 min, 20 random times for every second were set as the "dechirped peaks" and fed into the same automatic one-to-one coincidence search with WWLLN lightning. The random match rate is around 16.7%. After subtracting the random match rate, we find that at least about 22.9% of whistlers correspond to a source lightning stroke detected by WWLLN. This number is comparable to the detection efficiency of WWLLN for strong lightning.

About 4.0% of WWLLN lightning strokes correspond to the whistlers observed by the RBSP satellites. Figure 2.5a shows the scatter plot of all the coincident WWLLN lightning strokes with energy versus arc distance in the waveguide to the nearest satellite footpoint. Figures 2.5b and 2.5c

are the histograms of energy and arc distance shown in Figure 2.5a. In Figure 2.5b, we see that the number of coincident lightning strokes decreases from ~4000 with the increase of arc distance below 7000 km. Above 7000 km, the number of coincident lightning strokes shows another small peak of ~200. This phenomenon is also found in the one-to-one coincidence between WWLLN and C/NOFS data [see *Jacobson et al.*, 2011, Figure 16]. They explained it as an expected behavior of the spherical-shell effect. In Figure 2.5c, the energy of coincident lightning strokes shows a peak of 1 – 10 kJ. If we only consider the range from 50 J to 500 kJ, the average and median energy of the coincident lightning strokes are about 7.5 kJ and 2.6 kJ, respectively, while the average and median energy of all detected lightning strokes are 6.5 kJ and 2.4 kJ, respectively. *Hutchins et al.* [2012] showed that the median energy of WWLLN lightning strokes is around 2 kJ after April 2011 (see their Figure 8), which is consistent with our results. In Figure 2.5a, the majority of the scatter points above ~100 J may suggest that any lightning stroke with energy $\geq$ 100 J may generate a whistler strong enough to be detected by the RBSP-EFW. Figure 2.5b shows that the lightning strokes detected near the footpoints (within 7000 km) have a larger potential to generate a whistler propagated to the inner magnetosphere. In Table 2.1 the numbers of lightning strokes detected by WWLLN within 2000 km of footpoints (both Northern and Southern Hemispheres) are shown as 12,699, 6103, and 20,005 respectively. The coincident rate increased from about 4.0% to 15.3% if the source region was narrowed to within 2000 km of footpoints. If the source regions of whistlers are extended beyond 2000 km from the footpoints, the coincident whistlers can increase from 5932 to 8308 (40.1%).

Based on the one-to-one coincident match between lightning-generated whistlers and lightning, we compared the energy of lighting from WWLLN data and Poynting flux calculated from RBSP data. The measurement along spin axis (w) on EFW is not capable to calculate the

Poynting flux so we use the EMFISIS data at the same period when it is available. The calculation of Poynting flux density followed the work in *Santolík et al.*, [2010]. Figure 2.6 showed the scatter plot for each lightning-whistler pair when EMFISIS data is available. The Poynting flux is integrated between 1 – 8 kHz with an FFT bin size of 68.36 Hz (35000 Hz/512). In Figure 2.6, it is shown that there is not a strong linear correlation between lightning energy and whistler Poynting flux. Most of the points are located at 10^3 to 10^4 J, which is near the average energy of WWLLN lightning as we explained before. We applied a linear fitting (solid) on these data, and the formula is y = 6829.41 + 20.11 * x (y is the lighting energy and x is the Poynting flux). A power law fitting is also shown in the figure as dashed curve, and the formula is lg(y) = 3.36 + 0.13 * lg(x). It looks like the power law fitting works better than the linear fitting here. From the fitting results we can find that the propagation of energy from lightning to whistlers in the inner magnetosphere is still a complicated problem. The main reasons are, first, there can be multiple entry points for lightning energy to leak into the ionosphere during propagation in the waveguide; secondly, the channel size of each path for whistlers in the magnetosphere is also unknown. Sometimes there is a large flux tube (duct) which can reach to 0.5 R_E (we have an example in Chapter 3), but it is not necessary for non-ducted whistlers. However this work showed a possibility to predict the appearance of lightning-generated whistlers at satellite locations, and we may be able to provide a Poynting flux estimate based on the fitting equation.

We note that in August and September of 2013, the occurrence rate of one-to-one coincidence (29.7%) is much lower than in July 2013 (42.5%) or in March and April 2014 (40.1%). One reason may be that fewer lightning strokes are detected at high latitude in August and September. Although the arc distance from the possible source lightning to the footpoint varies from 0 to 18,000 km, the match rate of one-to-one coincidence between lightning and whistlers is still

dominated by lightning near the footpoint especially within 2000 km. Figures 2.4a – 2.4c show that the L shell coverage of the RBSP data in August and September 2013 is larger than in other two periods. The occurrence rate of lightning at high latitudes is lower than found at low latitude and midlatitude [*Hutchins et al.*, 2012], and the number of lightning strokes detected at the footpoints in August and September 2013 is lower than for the other two periods (Table 2.1). Another reason may be the failure of finding one-to-one coincidence between lightning and whistlers at high L shells. In Figure 2.4d, no dechirped peaks are observed above L = 3 during 7 min of data sampling between L = 3 and 3.5 and 13 min of data sampling above L = 5 in Figure 2.4b. This could be due to two different situations: (1) no whistlers are observed by RBSP satellites at high L shells; (2) whistlers are observed by RBSP but do not pass the dechirping process. After carefully checking the data above L = 3, it was found that no whistlers were observed when L is larger than 5. Although this is consistent with the work of *Koons* [1985], we cannot conclusively state that lightning has no impact at L > 5. There are three possible reasons whistlers may not be observed above L = 5. First, the magnetic field around the geomagnetic equator is small at high L shells, so the whistlers would have a low upper cutoff frequency and may be masked by low-frequency noise or even be reflected before they arrived at the satellites. Second, the amplitude of whistlers may be not strong enough due to the attenuation. *Burkholder et al.* [2013] showed that within the ionosphere, there is an approximately 3 order of magnitude loss of energy from the footpoint to C/NOFS satellites. Third, the propagation of whistlers at high L shell may not follow the same magnetic field line, so the lightning-generated whistler waves near the footpoint may not reach the geomagnetic equator of the same L shell. The propagation of magnetospherically reflected whistlers is studied by ray trace method [e.g., *Bortnik et al.*, 2002, 2003]. By reviewing recent EMFISIS data collected during the Northern Hemisphere summer in 2015, we identified

several lightning-generated whistler waves with upper cutoff frequencies of ~2 kHz observed near the RBSP apogee (L ≈ 5.797) which may correspond to WWLLN located lightning. It is also found that in the 7 min data located between L = 3 and 3.5, there were whistlers observed by RBSP but which failed to pass the dechirping process. This may be due to the fact that the dispersion is stronger and the whistler waves may no longer be fully displayed in the 1 s window, and the dispersion constant may also exceed the number we set. At last, nose whistlers may be observed when L shell is large. Figure 2.7 shows an example of a nose whistler observed by RBSP-A at L ≈ 3.88 on 16 July 2014. Lightning near the footpoint is detected at 07:15:38.64 (Figure 2.7c and the dashed line in Figure 2.7). About 0.9 s later, both EFW and EMFISIS captured the nose whistler with a nose frequency of about 4.5 kHz and an upper cutoff frequency of about 8 kHz. As shown in Figures 2.7a and 2.7b EMFISIS provides more information at high frequency (8 – 12 kHz). The dechirping method used in our work has a band-pass filter of 1 – 8 kHz, which is no longer appropriate for nose whistlers because the nose frequency is usually lower than 6 kHz or even 4 kHz in the outer magnetosphere [*Helliwell*, 1965, Figures 4 – 19]. With a better dechirping process in the future, we can probably get more information about the contribution of lightning to the high L shell whistlers in the magnetosphere.

2.5 CONCLUSIONS

A study of simultaneous observations of global lightning and whistlers was conducted from July to September 2013 and from March to April 2014. Global lightning data of the past 3 years from the WWLLN were used to forecast lightning conditions along the trajectory of RBSP's magnetic field footpoints. Ten minutes with the highest lightning probability around the footpoints were selected for burst mode recording on the satellites. Data were downloaded for short time periods during 170 days, leading to a total of 605 min of high-resolution waveform which were statistically

analyzed in this paper. By using this method, lightning-generated whistlers near the magnetic equator at low L shell regions can be successfully predicted with a rate of 80.2%. This new data set should prove valuable for the future study of whistler-related phenomena. About 22.6% of the whistlers observed by the satellites correspond to possible source lightning in the actual WWLLN data, which closely matched the time and location. This rate also agrees with the detection efficiency of WWLLN. The source regions of whistlers are extended 2000 km from the footpoints in this study. About 40.1% more whistlers observed by the RBSP satellites are found to correspond with WWLLN lightning. Lightning strokes with energy larger than 100 J all have the potential to generate a whistler and propagate to the inner magnetosphere. We show that whistlers strongly correspond to WWLLN lightning at low L shell ($L < 3$) regions. The correspondence between high L shell whistlers and lightning still exist but need further study.

Acknowledgments. The authors wish to acknowledge partial support for this research from CRDF grant RUG1-7084-PA-13, from NOAA grant NA10OAR4320148, and from NSF grant 1443011. The authors wish to thank the World Wide Lightning Location Network (http://wwlln.net), a collaboration among over 50 universities and institutions, for providing the lightning location data used in this paper. The authors wish to acknowledge the Space Sciences Laboratory at University of Berkeley and the University of Minnesota for providing EFW data (data link: http://www.space.umn.edu/rbspefw-data/, PI: John Wygant) and the University of Iowa for providing the EMFISIS data (data link: http://emfisis.physics.uiowa.edu/data/index, PI: Craig Kletzing), both of which are instruments on board the Van Allen Probes.

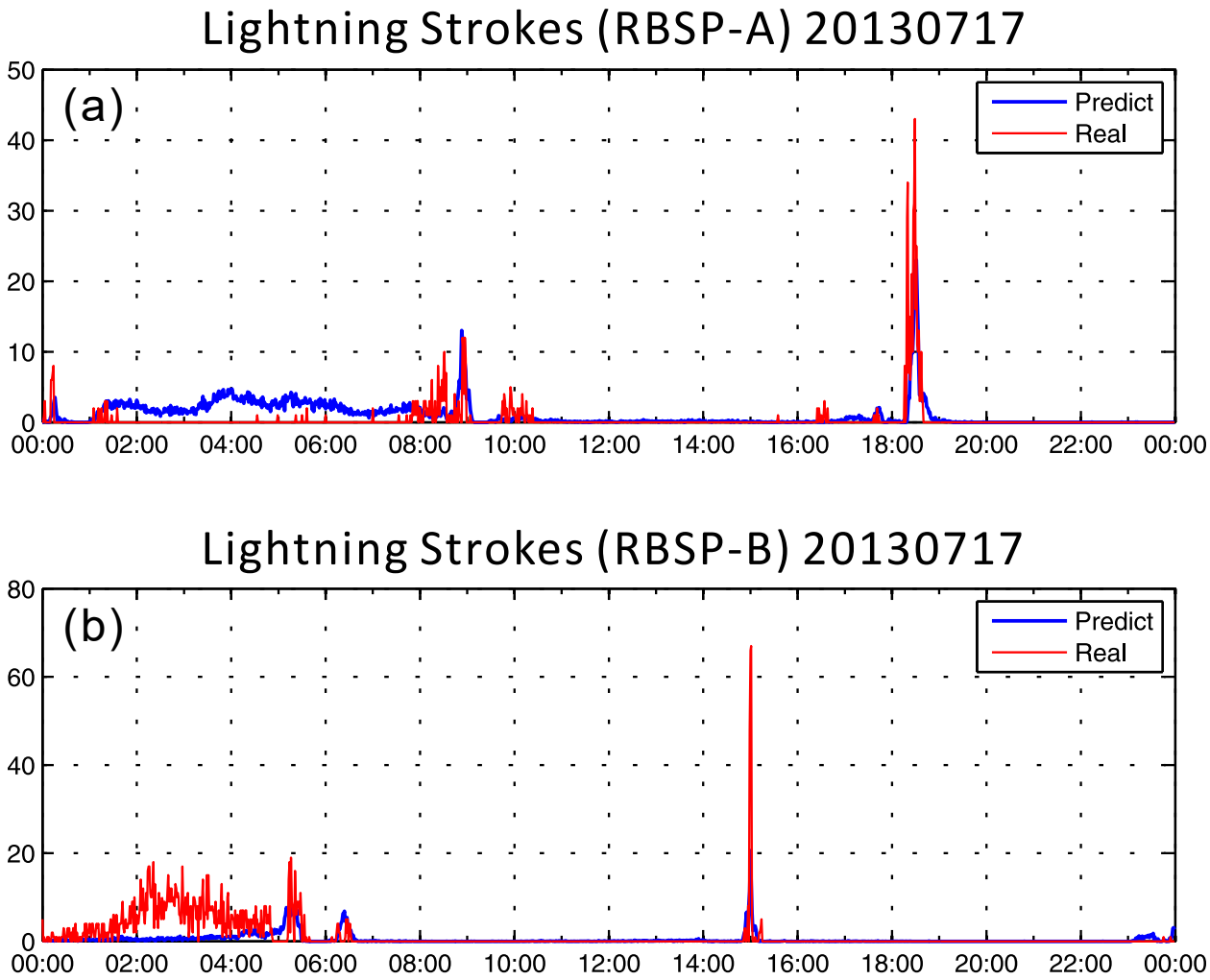

Figure 2.1. Prediction and real results for (a) RBSP-A and (b) RBSP-B on 17 July 2013. The red lines show the real result, and blue lines show the prediction result.

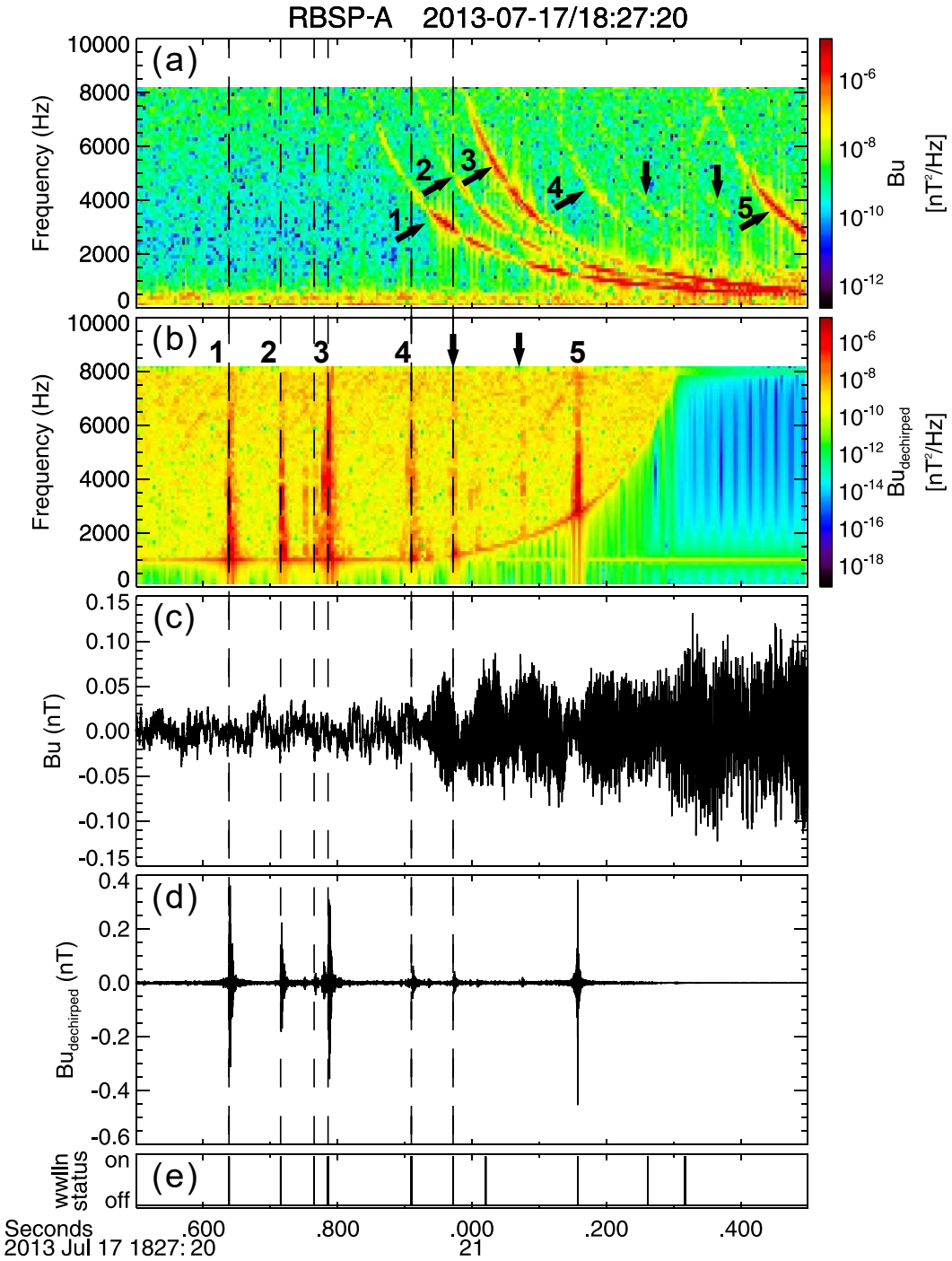

Figure 2.2. Spectrogram and waveform of Bu component on RBSP-A from 18:27:20.5 UT to 18:27:21.5 UT on 17 July 2013. (a) Original spectrogram. (b) Dechirped spectrogram. (c) Original waveform. (d) Dechirped waveform. (e) Timing of WWLLN lightning strokes near the satellite footpoints. The vertical dashed lines represent the WWLLN lightning time observed in first half of the second.

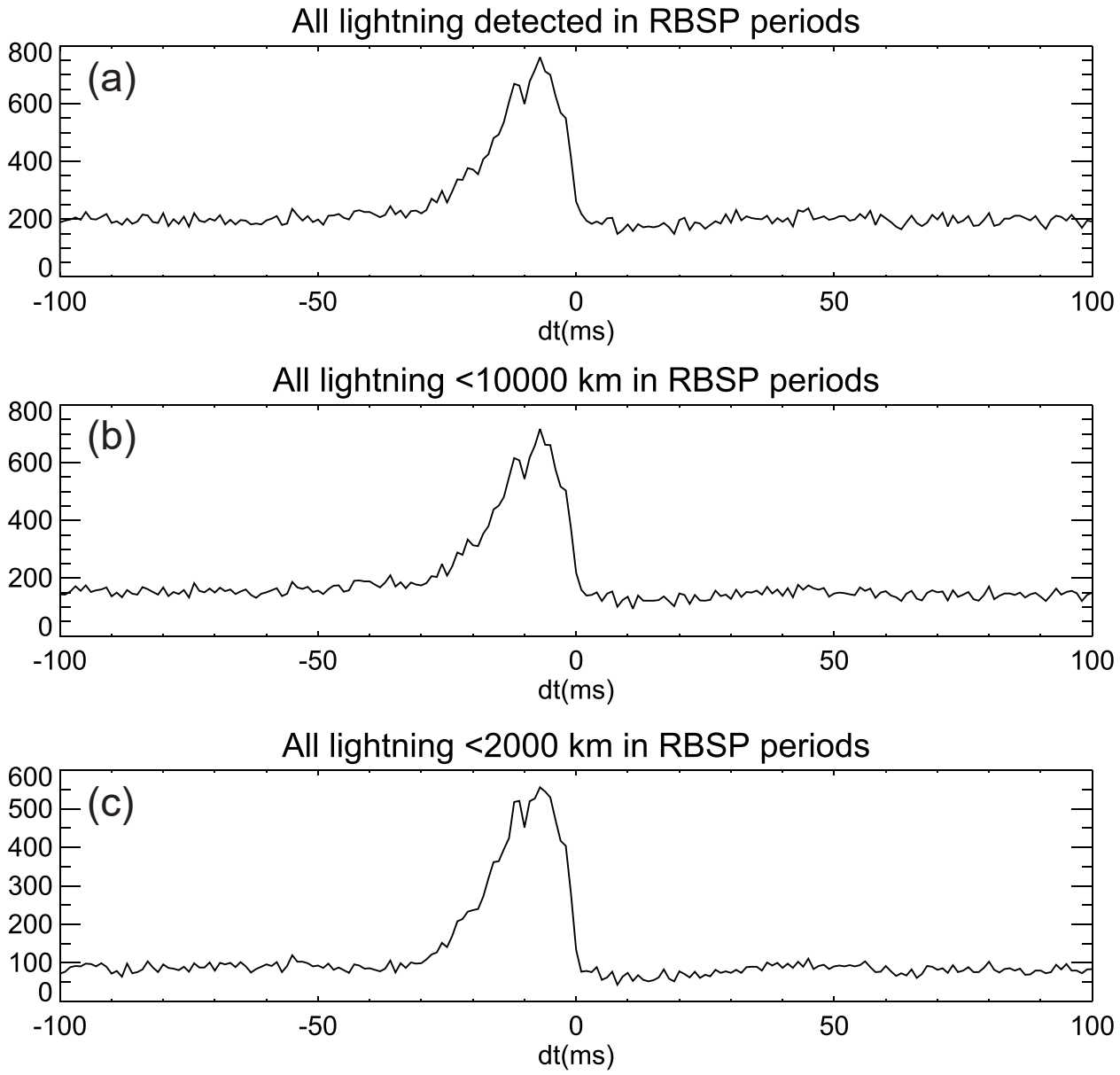

Figure 2.3. Histogram of corrected dechirped peak time minus WWLLN stroke time in every 2s dechirping window, after correction for two propagation terms. (a) Including all WWLLN strokes. (b) Including WWLLN strokes within 10,000 km. (c) Including WWLLN strokes within 2000 km.

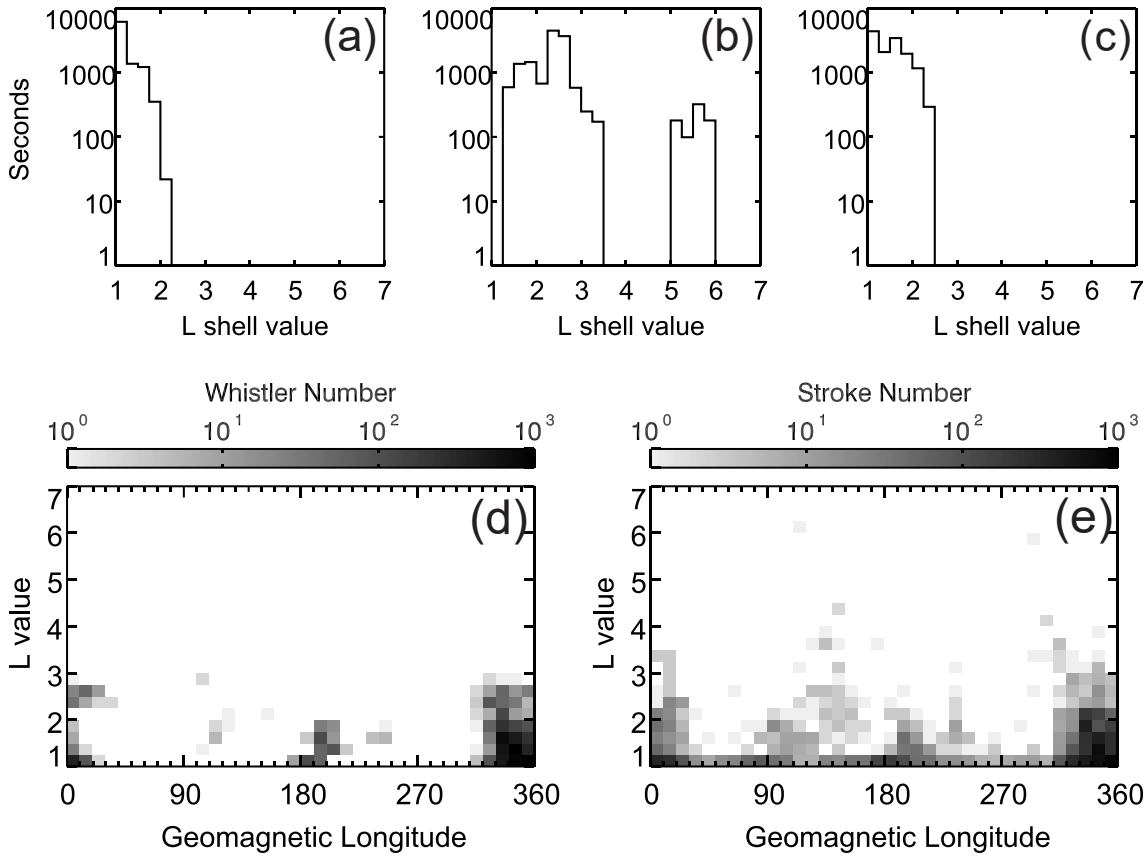

Figure 2.4. (a–c) L shell value distribution of data downloaded by both RBSP-A and B in seconds: (a) July 2013, (b) August and September 2013, and (c) March and April 2014. (d) Footpoint location of RBSP satellites when whistlers are observed with a one-to-one coincident WWLLN source lightning. (e) Location of WWLLN lightning strokes which are one-to-one coincident with whistlers observed on RBSP satellites. Figures 2.4d and 2.4e are all plotted in geomagnetic coordinate system.

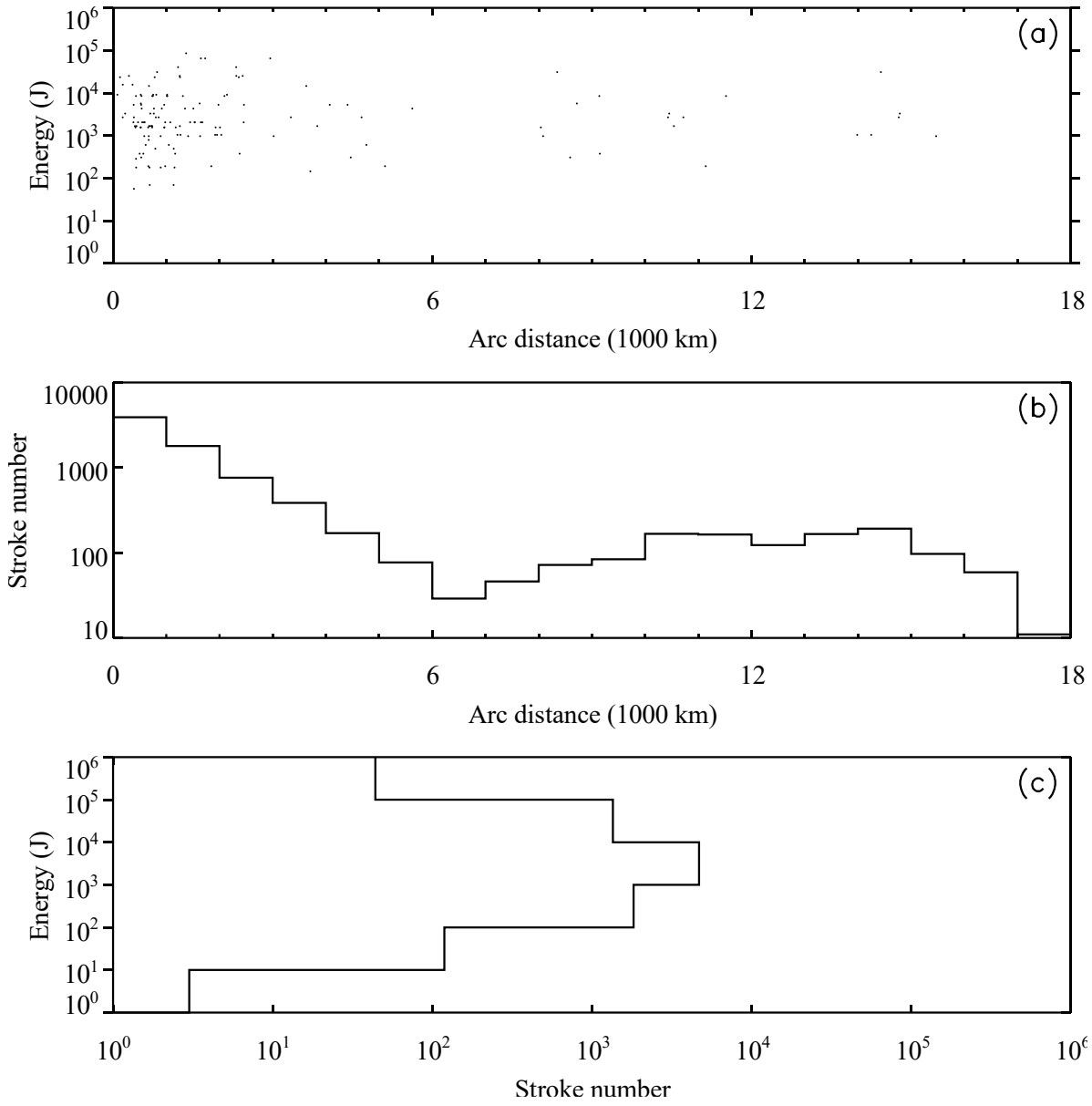

Figure 2.5. Distribution of one-to-one coincident lightning with energy vs arc distance from lightning to satellite footpoint. (a) Scatter plot; (b) Histogram of arc distance from lightning to satellite footpoint. (c) Histogram of lightning energy.

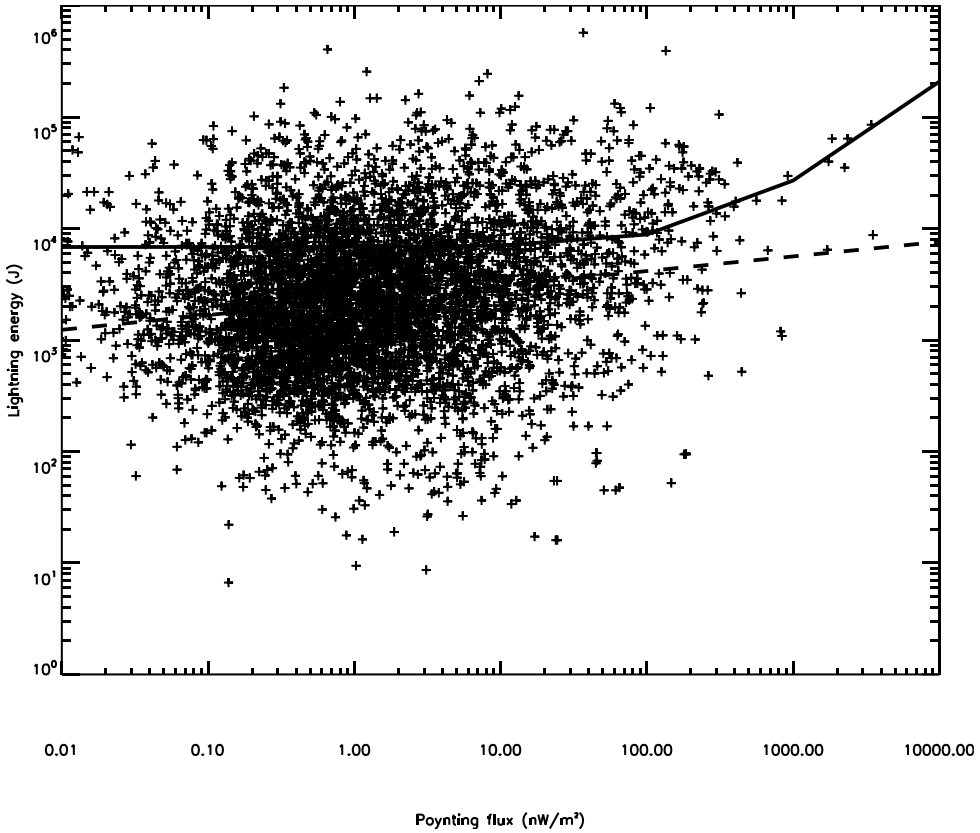

Figure 2.6. Scatter plot of lightning energy from WWLLN and Poynting flux calculated from EMFISIS at RBSP for one-to-one coincident events. Both linear fitting and power law fitting results are shown here as solid and dashed curves (fitting formula in text).

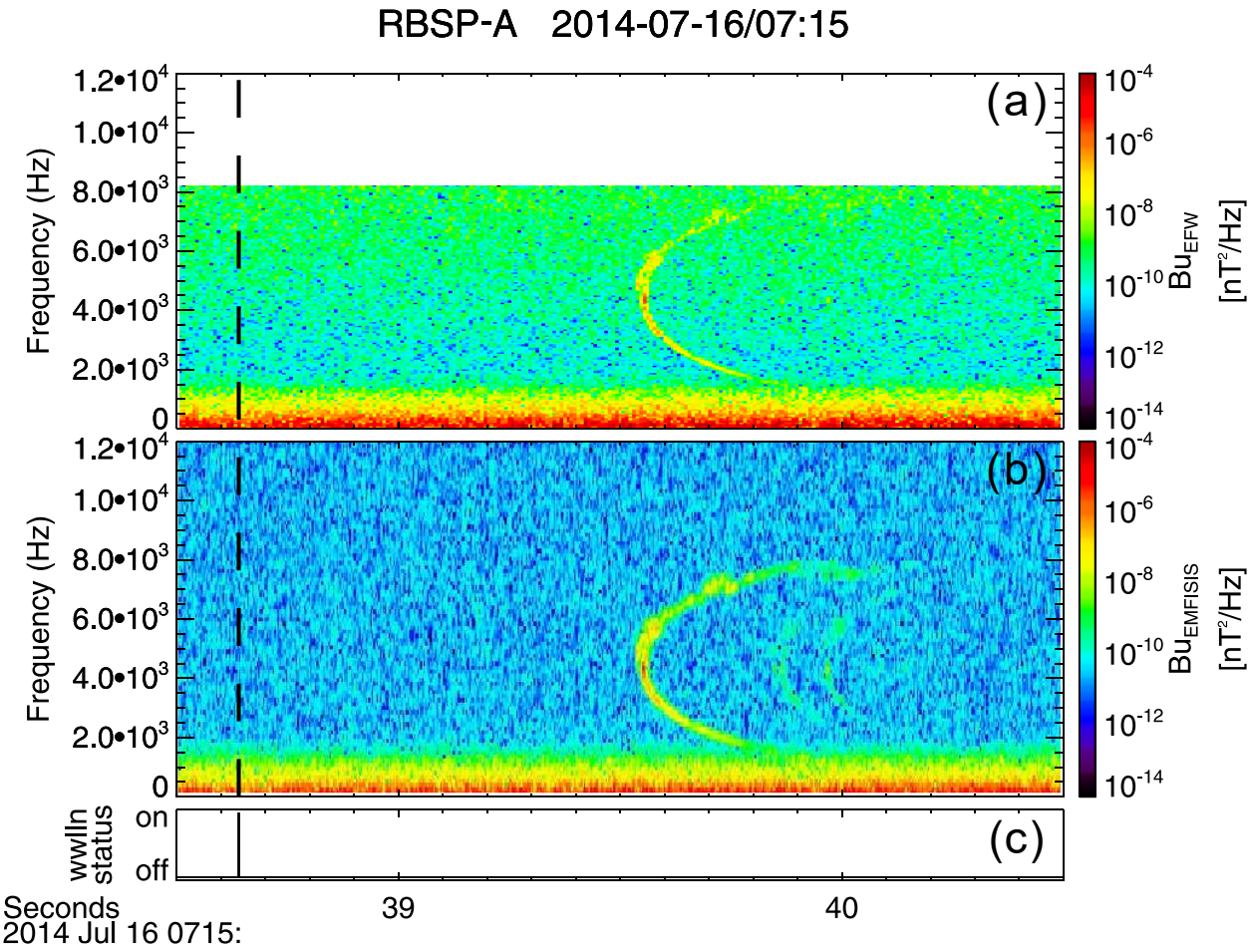

Figure 2.7. A nose whistler example observed by RBSP-A from 07:15:38.5 UT to 07:15:40.5 UT on 16 July 2014. (a) EFW spectrogram. (b) EMSIFIS spectrogram. (c) Timing of WWLLN lightning strokes near the satellite footpoints. The vertical dashed line also represents the WWLLN lightning time.

Table 2.1. Statistical results of whistler waves observed by RBSP and WWLLN lightning.

	July 2013	Aug – Sep 2013	Mar – Apr 2014	Total
Number of sampling minute	151	233	221	605
Number of sampling minute with dechirped peaks	140	150	195	485
Percentage	92.7%	64.4%	88.2%	80.2%
Number of dechirped peaks	5938	2454	12,594	20,986
Number of coincident dechirped peaks	2526	730	5052	8308
Percentage	42.5%	29.7%	40.1%	39.6%
Number of global WWLLN lightning strokes	54,675	62,520	89,275	206,470
Number of coincident WWLLN lightning strokes	2526	730	5052	8308
Percentage	4.6%	1.2%	5.7%	4.0%
Number of WWLLN lightning strokes within 2000 km	12,699	6103	20,005	38,777
Number of coincident WWLLN lightning strokes within 2000 km	2004	452	3476	5932
Percentage	15.8%	7.4%	17.4%	15.3%

Chapter 3. INTERACTIONS BETWEEN ENERGETIC ELECTRONS AND STRONG LIGHTNING-GENERATED WHISTLER WAVES OBSERVED AT HIGH L-SHELLS

3.1 INTRODUCTION

In the past few decades, it has been shown that there are three main loss mechanisms of radiation belt electrons: losses across the magnetopause, precipitation into the upper atmosphere and outward radial diffusion. The losses across the magnetopause and outward radial diffusion have been used to explain the rapid depletion of relativistic electrons in the outer radiation belt down to L > 5 [e.g., *Bortnik et al.*, 2006a, *Turner et al.*, 2012]. Electron precipitation into the upper atmosphere is mainly controlled by pitch angle scattering process, including Coulomb collisions and resonant wave-particle interactions between different types of plasma waves and energetic electrons [e.g., *Abel and Thorne*, 1998a, 1998b].

Pitch angle scattering outside the plasmasphere is mainly due to whistler-mode chorus waves [*Horne and Thorne*, 2003; *Thorne et al.*, 2005]. Inside the plasmasphere, the loss of electrons is mainly due to Coulomb collisions, lightning-generated whistlers, plasmaspheric hiss and man-made VLF transmitter signals. Based on the calculations in *Abel and Thorne* [1998a], three types of VLF waves may interact with energetic electrons of different energies and are dominant at different L-shells. By using the average wave intensity, lightning whistlers are suggested to be important drivers between 2.0 < L < 3.2, but much weaker than plasmaspheric hiss at L > 2.4. *Bortnik et al.* [2003] qualitatively estimated the energy distribution and lifetimes of magetospherically reflected (MR) whistlers in the plasmasphere and indicated that these MR whistlers may play a more important role than assumed in previous work at slot region. *Rodger et*

al., [2003] suggested that long-term loss driven by whistlers is more significant than all other loss processes for energetic electrons in the range of 50 – 150 keV at L = 2 – 2.4. Based on the average wave densities from CRRES measurements, *Meredith et al.*, [2007] estimated the loss timescales due to plasmaspheric hiss and lightning-generated whistlers in and above the slot region. The results showed that the loss of electrons with energies larger than 500 keV in the region $2.5 < L < 4.0$ is dominated by plasmaspheric hiss with small wave normal angles. At lower energies, ducted whistlers are more effective as a scattering process than plasmaspheric hiss, but still with a much longer loss timescale. By adding the observations from SAMPEX satellites and comparing the new results with their previous work, *Meredith et al.*, [2009] found that plasmaspheric hiss alone can't account for the observed loss timescales at $2.0 < L < 2.4$. The observed loss required the combined effects of plasmaspheric hiss and ducted lightning-generated whistlers. Although the power of whistlers used in their calculations is two orders of magnitude less than hiss, it is shown that whistlers can still play an important role in electron loss at the inner slot region. In the past decade, CRRES data were used in different models to estimate the scattering loss due to plasmaspheric hiss and lightning-generated whistlers [e.g. *Meredith et al.*, 2007; *Glauert et al.*, 2014]. It is believed that lightning-generated whistlers only have an effect on < 500 keV electrons due to the frequency range ($2.0 < f < 5.0$ kHz) and have weaker effects than plasmaspheric hiss due to the lower average wave amplitude (one or two orders of magnitude less).

Lightning-induced electron precipitation (LEP) from the Earth's radiation belts is a known troposphere-to-magnetosphere coupling mechanism caused by wave-particle interactions. *Voss et al.*, [1984] showed the first LEP event from the observations of SEEP experiment on S81-1 satellite. It was shown that a single LEP burst (10^{-3} erg s^{-1} cm^{-2}) is estimated to deplete ~0.001% of the particles in the slot region [*Voss et al.*, 1998]. The LEP events proved that lightning whistlers

may be important for pitch angle scattering of 100 – 250 keV electrons in the slot region. Simultaneous observations of LEP events and lightning-generated whistlers have been observed on the DEMETER satellite with apogee ~700 km altitude [*Inan et al.*, 2007]. The LEP events are observed within <1 second of source lightning and are coincident with a flux increase of 100 – 300 keV electrons.

Lightning-generated whistlers are also considered as a potential source of plasmaspheric hiss inside the plasmasphere [e.g., *Dowden*, 1971; *Draganov et al.*, 1992; *Green et al.*, 2005]. It was shown that whistlers produced by a single lightning event can form a continuous hiss-like signal at a fixed point after multiple magnetospheric reflections and phase mixing [*Draganov et al.*, 1992]. The analysis of DE-1 and IMAGE data by *Green et al.*, [2005] showed that the geographic distribution of plasmaspheric hiss over frequencies of ~500 Hz to ~3 kHz is similar to the distribution of lightning, with emissions stronger over continents than over ocean, stronger in the summer than in the winter and stronger on the dayside than on the nightside. This interpretation is still controversial [e.g. *Thorne et al.*, 2006; *Green et al.*, 2006; *Meredith et al.*, 2006]. By using data from the CRRES satellite, *Meredith et al.* [2006] found that the VLF waves over frequencies of 2.0 – 5.0 kHz are most likely related to lightning-generated whistlers, however, the waves at lower frequencies increase with geomagnetic activity, which should be independent of lightning.

The source and destination of lightning-generated whistlers have been studied for decades. Possible one-to-one connections between whistlers and specific individual lightning strokes were firstly studied with in situ rocket-borne measurements [e.g., *Kelley et al.*, 1985; *Holzworth et al.*, 1985; *Kelley et al.*, 1990] and then extended to several hundred kilometers altitude with measurements from LEO satellites like DEMETER [e.g., *Santolík et al.*, 2009] and C/NOFS [e.g., *Holzworth et al.*, 2011; *Jacobson et al.*, 2011]. By analyzing the high time-resolution waveform

data from Van Allen Probes and global lightning data from the World Wide Lighting Location Network (WWLLN), the one-to-one relationship between lightning strokes and lightning-generated whistlers can be extended to L > 4 near the magnetic equator [*Zheng et al.*, 2016].

Due to the limited data sampling rate or the limited space coverage on satellites, long-time-averaged wave emissions over some specific frequency ranges were used to estimate the effect of lightning-generated whistlers. However, in our recent work, we found that the wave amplitude of lightning-generated whistlers in specific events can be much stronger than the average wave intensities used in previous work. In this paper, we would like to show you two strong lightning-generated whistlers events observed at L > 3 near the geomagnetic equator with peak amplitude of waveform perturbation larger than 0.1 nT. We will present direct evidence of strong lightning-generated whistlers scattering energetic electrons in the outer radiation belt.

3.2 DATABASE

3.2.1 *Van Allen Probes*

The Van Allen Probes (formerly known as the Radiation Belt Storm Probes (RBSPs)) were launched in August 2012 into a near-equatorial orbit with 10° inclination. The two probes traverse roughly the same orbit with 1.1 R_E × 5.8 R_E (from the center of the Earth), which cut through both the inner and outer radiation belts [*Stratton et al.*, 2013]. The Electric and Magnetic Field Instrument Suite and Integrated Science (EMFISIS) wave instrument on board provides 3-D measurements of wave electric and magnetic fields and DC magnetic fields [*Kletzing et al.*, 2013]. The six-channel Waveform Receiver (WFR) on EMFISIS has a continuous coverage of wave power spectral density in the survey mode from 10 Hz to 12 kHz and a variable coverage of full waveform data in the burst mode with a sampling rate up to 35 ksamples/s. The Magnetic Electron

Ion Spectrometer (MagEIS) provides electron distributions with energies from ~30 keV to 4 MeV at a time cadence of 11 s [*Blake et al.*, 2013].

3.2.2 *WWLLN*

WWLLN detects lightning by monitoring the Time-Of-Group-Arrival (TOGA) of VLF lightning sferics at five or more stations simultaneously located globally [*Dowden et al.*, 2002]. This network has improved in accuracy and detection efficiency with the addition of many new stations since 2004. In 2011, the network had an estimated detection efficiency of about 11% for Cloud-Ground strokes and can be >50% for stokes with higher peak current [*Hutchins et al.*, 2012]. *Zheng et al.*, [2016] previously showed that the conjunction between Van Allen Probes and WWLLN is helpful to find the source lightning of whistlers observed around magnetic equator especially at low L-shells.

3.3 OBSERVATIONS

3.3.1 *Oblique Whistler Event*

Figure 3.1 shows an overview of lightning-generated whistler measurements from RBSP-A on 20141004 from 0900 to 0910UT. In this event, we had rare continuous burst mode data from EMFISIS for about 20 minutes (only the last 10 minutes data are shown here). During this event, Van Allen Probes were close to the magnetic equator (| MLAT (magnetic latitude) | < 5°), therefore we directly used the local measurements to represent the magnetic equatorial parameters. The L value of RBSP-A varied from 3.69 to 3.08 in 20 minutes and MLT was around 8.0. As illustrated in Figure 3.1a and 3.1b, it is still difficult to identify the dispersed whistler pattern in magnetic/electric wave power spectra with such a condensed plot. Every individual lightning-generated whistler wave appeared as spikes in the frequency range between 0 – 4kHz. There are

also two narrow band of waves at ~1kHz and ~300 Hz, which may be the plasmaspheric hiss waves. Unlike the previous studies in the introduction, the wave amplitudes of whistlers in this event are very strong. The magnetic perturbation was even larger than 0.2 nT at 090528UT and 090812UT, with multiple peaks higher than 0.1 nT (Figure 3.1c). In figure 3.1d – 3.1h, the 1-minute plot from 0908 to 0909UT could provide more details about this event. The spectrogram in Figure 3.1d is very similar to the first MR (non-ducted) whistler spectrogram from OGO 1, which usually contains a series of echo train with decreasing nose frequency [*Smith et al.*, 1968]. In this event, each group of whistler waves and three possible echoes became more dispersed after multiple reflections. It also agrees with the ray tracing simulation results at L = 3 – 3.5 in *Bortnik et al.*, [2003]. In order to select the frequency spectrum of whistler waves and get rid of background, only PSD higher than 5 times of its median value at each frequency bin are kept in Figure 3.1f. From the Poynting vector angle shown in Figure 3.1g, it is clearly seen that whistler echoes passed the satellite point from different directions. The wave normal angle (calculated by SVD method [*Santolík et al.*, 2003]) of non-ducted whistler waves was already very large when the first wave arrived at satellite and became even closer to 90° after several more reflections (Figure 3.1h).

As shown in Figure 3.1, strong non-ducted whistler waves were observed by Van Allen Probes, and detailed necessary wave parameters were provided to model the scattering effects. Here we used the EMFISIS measurements from 0908 to 0909 UT in Figure 3.1f as the average wave frequency spectrum. The electron density and background magnetic field amplitude were obtained from in situ measurements, producing a high ratio of electron plasma frequency to gyrofrequency. Since the wave normal angle of non-ducted whistlers increased rapidly after first reflection [*Bortnik et al.*, 2006b; *Meredith et al.*, 2007], we assumed that the wave normal angle

remained highly oblique at high L-shells. The input wave parameters we obtained from RBSP-A are shown in Figure 3.2. Specifically, the red, blue and black curves in figure 3.2a indicate the averaged power spectral density of all waves (Figure 3.1d), hiss wave (median value of Figure 3.1d) and only whistlers (Figure 3.1f). In this event, the total wave spectrum can also be divided into three frequency ranges: mostly hiss waves below 500 Hz, a mixture of hiss waves and lightning-generated whistler waves from 500 Hz to 1.1 kHz and mostly lightning-generated whistler waves from 1.1 kHz to 4 kHz. Unlike previous work which only calculated the contribution of lightning-generated whistlers from 2 kHz, the event shows that we can extend the lower cutoff frequency to 500 Hz. The wave spectral densities shown here are slightly different from average results at quiet times (Figure 2 in *Meredith et al.*, [2007]), with stronger whistler intensity and weaker hiss intensity in this event. The wave normal angle spectrum of whistlers (Figure 3.1h) is also shown in Figure 3.2b. The majority of the waves have large wave normal angles around 65°, and we applied a Gaussian fitting for the wave normal angle distribution in the following model. To quantify the scattering effects of this strong non-ducted whistler event, we calculated the bounce-averaged diffusion coefficients by using Full Diffusion Code [*Ni et al.*, 2008, 2011; *Shprits & Ni*, 2009] at different pitch angles and energies. Cyclotron resonances with harmonic numbers ranging from -10 to +10 (including Landau resonance) were included in the calculations.

The bounce-averaged pitch angle diffusion coefficients ($<D_{\alpha\alpha}>$) are shown as a function of pitch angle (PA or α) and electron kinetic energy (E_k) in Figure 3.3. The dominant scattering effect of lightning-generated whistlers is pitch angle scattering, with a much weaker effect of momentum diffusion. There are some interesting features related with this event of strong non-ducted whistler scattering. There are two parts of large diffusion coefficients in Figure 3.3a. In the near

perpendicular direction (PA = 70° – 90°), the electrons of ~10 to ~100 keV may be efficiently scattered due to Landau resonance. For the resonant electron energies from 30 keV to 100 keV, the diffusion coefficients remain large from near loss cone to intermediate pitch angles like 30°. There is also a rise to high energy around several hundred keV of $<D_{\alpha\alpha}>$ around pitch angle of 20°. The maximum value of $<D_{\alpha\alpha}>$ can reach to 10^{-5} s^{-1}, which is almost the same level as hiss waves in previous work [*Ni et al.*, 2013].

To examine the evidence of strong non-ducted whistler scattering, measurements of RBSP-B were also checked since the two Van Allen Probes were in a very similar orbit. In this event, two probes passed the same L shell at similar MLT, with RBSP-B trailing by ~86 minutes. Different geomagnetic indices on 04 October 2014 were also checked. The minimum Dst was -8 nT, the minimum SYM-H was -15 nT and Kp index was 1. Under such a quiet geomagnetic condition, we assumed that the structure of the plasmasphere didn't change too much within ~86 minutes. Therefore, the difference of measurements on RBSP-B and RBSP-A could be a temporal effect more than a spatial effect. The survey mode data of EMFISIS measurements from RBSP-A and RBSP-B when passing the same L-shells were shown in Figure 3.4. Although the resolution of the survey mode data is not as high as burst mode data in Figure 3.1, we can still find multiple "spikes" as the indication of non-ducted whistlers on both satellites. It is shown that the non-ducted whistlers still exist at the L-shells after ~86 minutes when RBSP-B arrived. Meanwhile, the lightning data from WWLLN were also checked during these two periods. In Figure 3.5a and 3.5b, the location of thunderstorms near the satellite footpoints doesn't change significantly since the thunderstorms normally last a time scale of hours. The lightning source of the strong non-ducted whistlers may originate from one of the thunderstorms in the North Atlantic Ocean based on the longitude of satellite footpoints and the ray tracing results at L = 3.5 in *Bortnik et al.*, 2003. Due

to the rotation of the Earth in ~86 minutes, the footpoints of RBSP-B were westward of the footpoints of RBSP-A when passing the same L-shell. From previous research [*Holzworth et al.*, 2011; *Zheng et al.*, 2016], it was shown that the entry point of the whistler waves into the ionosphere can be many thousands of kilometers away from the source lightings. The highest amplitudes of whistlers may be observed up to distances of ~500 km to 1000 km [*Fiser et al.*, 2010, *Jacobson et al.*, 2011]. Therefore, the whistlers generated from one thunderstorm may have the ability to "illuminate" a longitude range of ~20° to 50° (depends on the latitude). In Figure 3.5 it is shown that the footpoints of two Van Allen Probes are located at two sides of an intense line of thunderstorms in the North Atlantic both within 10° of these storms. After a short time of rotation, it is still possible that the non-ducted whistlers observed on both Van Allen Probes were generated from the lightning strokes of the same thunderstorm area, which propagated in the Earth-ionosphere waveguide and illuminated the same area in the inner magnetosphere.

The pitch angle distribution from both satellites at L = 3.40 are shown in Figure 3.6. The variation in ~86 minutes is not large, as expected. But the pitch angle distribution of ~100 keV electrons still shows a weak diffusion process which agrees with diffusion coefficients. The electrons around 80° have a small peak which corresponds with the Landau resonance at a perpendicular direction, which is also known as a "top-hat" distribution. Meanwhile, the electron phase space density (PSD) slightly decreases at intermediate pitch angles and then increases at lower pitch angles near the loss cone. We also examined the lightning-induced electron precipitation (LEP) by using measurements of POES/MetOp satellites [*Evans and Green*, 2004]. MetOp-B is close to the region of whistlers for less than 1 minute. Figure 3.7 presents the data of RBSP-A and MetOp-B during the conjunction period. Here we require the L-shell value difference between two satellites to be less than 0.1, which result in a ~40 second conjunction window.

During this period, the MLT difference is no larger than 0.65, which is also reasonable. The medium energy proton and electron detector (MEPED) on POES can provide integral electron flux in four energy bands (> 40 keV, >130 keV, >287 keV and >612 keV). In this 40-second window, there are five precipitation peaks observed at 07:05, 07:09, 07:17, 07:23 and 07:35 – 07:39. The time resolution of MEPED data is 2 seconds so sometimes it is hard to make a one-to-one match between lightning whistlers and flux peaks. Unlike the LEP events at low-L shell, the peak flux is only four times of background here. This is probably due to the sensitivity of POES satellites and the low trapped flux at around 100 keV near the outer radiation belt boundary. In some of the peaks, the flux of >287 keV is higher than >130 keV, that's caused by the geometry factors at different energy channels. The original count rate data (not shown) are checked to have reasonable numbers at different energy channels.

3.3.2 *Ducted Whistler Event*

Figure 3.8 shows an overview of ducted whistler measurements from RBSP-A on 20160625 from 0844 to 0845UT. In this event, RBSP-A was also close to the magnetic equator around L = 3.96. The maximum magnetic perturbation of the whistlers was larger than 0.4 nT at 08:44:28.5UT. The frequency range of the ducted whistlers was much higher than non-ducted whistlers due to the higher plasma density (not shown here). The electron densities which inferred from the upper hybrid resonance frequency f_{uh} on EMFISIS [*Kurth et al.*, 2015] showed a density increase from 08:42 to 08:59 UT, indicating a duct here. From previous studies, the ducted whistlers usually propagate along the magnetic field lines and can be received (also reflected) at the conjugate point of the other hemisphere [*Helliwell*, 1965]. The Poynting vector angle showed that the initial whistlers propagated from northern hemisphere to the satellite. Two-hop whistler echoes were also observed coming from southern hemisphere. As a ducted whistler event, the wave normal angle in

this event stayed at a small number after one reflection. 10 of lightning strokes from WWLLN dataset were found within 10° away from the northern magnetic footpoint of the satellite. Each of them was about 1 second before the arrival of whistlers on RBSP-A.

Here we also used the wave parameters provided on RBSP-A to model the scattering effects of ducted whistlers. The average wave frequency spectrum, electron density and background magnetic field amplitude obtained from RBSP-A is shown in Figure 3.9a. The two peaks in the wave frequency spectrum correspond to different frequency ranges of the initial whistlers and whistler echoes. We assumed that the wave normal angle didn't change during reflections in the duct. The bounce-averaged diffusion coefficients are shown in Figure 3.10. The results are similar to plasmaspheric hiss, but the scattering energy is much lower due to its higher frequency [*Ma et al.*, 2015]. The strong ducted whistlers may cause the energetic electron loss mostly at several to tens of keV, with an extension to a hundred keV. In this event, the other Van Allen Probe was far away, and it didn't pass the same L shell at a similar MLT in a short time period. We also didn't find any LEO satellites passing through the same L-shells in 1 minute. Figure 3.11 shows the electron distribution variation in 2 minutes on RBSP-A. The L-shell changed from 3.91 to 3.97. The electron loss at large pitch angles occurred at energies lower than 143 keV. At some energies lower than 108 keV, the electron PSD increased at low pitch angles near loss cone. This agrees with our diffusion coefficient results, but it can also be a spatial effect since RBSP-A moved ~400 km (0.06 R_E).

3.4 DISCUSSIONS

In this paper, we present two strong events of lightning-generated whistlers from Van Allen Probes near the geomagnetic equator of outer radiation belt. By using full waveform data from EMFISIS, we conducted a detailed study of lightning whistler events around geomagnetic equator. Lightning

whistlers at L > 3 can be divided into non-ducted and ducted types by checking the wave normal angles. During the non-ducted whistler event, wave and particle measurements from two probes show a trace of pitch angle scattering. In this event, the whistlers generated from the same thunderstorm may be observed by both probes passing the same L shell within ~86 minutes of separation. The pitch angle distribution around one hundred keV on both probes showed a possible "top-hat" near 90° and an increase near the loss cone region, which is a sign of the diffusion process. Only the wave components with strong power spectral density, which is at least 5 times higher than background were selected as whistler waves in our study. Possible hiss waves were removed by this method due to its continuous existence at similar strength. The wave spectral intensity of whistlers in this event is at least one order higher than the average intensity calculated in previous research. Using the wave properties of non-ducted whistlers observed on RBSP-A, we simulated the whistler wave scattering effects by modeling the evolution of the electron distribution. Bounce-averaged diffusion coefficients were calculated first based on the averaged wave frequency spectrum, electron density, background magnetic field and L-shell location. Low-altitude MetOp satellite, which has passed similar L-shells and MLT the same time provides the chance for the conjunction observations. Several electron precipitation events were observed related with lightning-generated whistlers. The ratio of peak flux over background is not as large as LEP events at low L-shells (e.g., L = 2.3 in *Voss et al*., [1984]). This is probably caused by the sensitivity of telescope design and low trapped electron flux near the outer radiation belt boundary.

Another ducted whistler event is also studied in this paper. A duct with increased electron density at a region of ~0.4 R_E is observed on RBSP-A. Multiple lightning-generated whistlers are detected with quasi-parallel propagation in a 1-minute window. The source lightning of some whistlers can be found in the WWLLN lightning map near the satellite footpoint. In this event, the

wave spectral intensity of whistlers is at least 20 times higher than the average intensity found before. The bounce-averaged diffusion coefficients showed similar results as hiss waves but working mostly in a lower energy range. Two probes comparison could be made in this event. But the variation of electron PSD on RBSP-A in 2 minutes agreed with the simulations. Although the simulation results showed that the strong ducted whistlers could deplete the electrons below 100 keV in about 1 – 2 hours, we would also like to point out that the duration of electron duct is a complicated question and it may not exist long enough and distributed at all MLT.

3.5 CONCLUSIONS

We conducted a detailed study of two lightning-generated whistler wave events at L > 3 region. Our results are as follows:

1. The wave intensity of lightning-generated whistlers can be much higher than the averaged results found in previous work. Specifically, the non-ducted whistler event in our work is at least one order higher and the ducted whistlers is more than 20 times higher.
2. The strong lightning-generated whistlers can be important for scattering electrons with energies near the 100 keV level.
3. Lightning-generated whistler waves may be underestimated for pitch-angle scattering effects at L > 3 regions.

Acknowledgments. The authors wish to acknowledge support from NSF grant 1443011. The authors wish to thank the World Wide Lightning Location Network (http://wwlln.net), a collaboration among over 50 universities and institutions, for providing the lightning location data used in this paper. The authors wish to acknowledge University of Iowa for providing the EMFISIS data (data link: http://emfisis.physics.uiowa.edu/data/index) and LANL for providing MagEIS

data (data link: https://www.rbsp-ect.lanl.gov/data_pub/), both of which are instruments on board the Van Allen Probes.

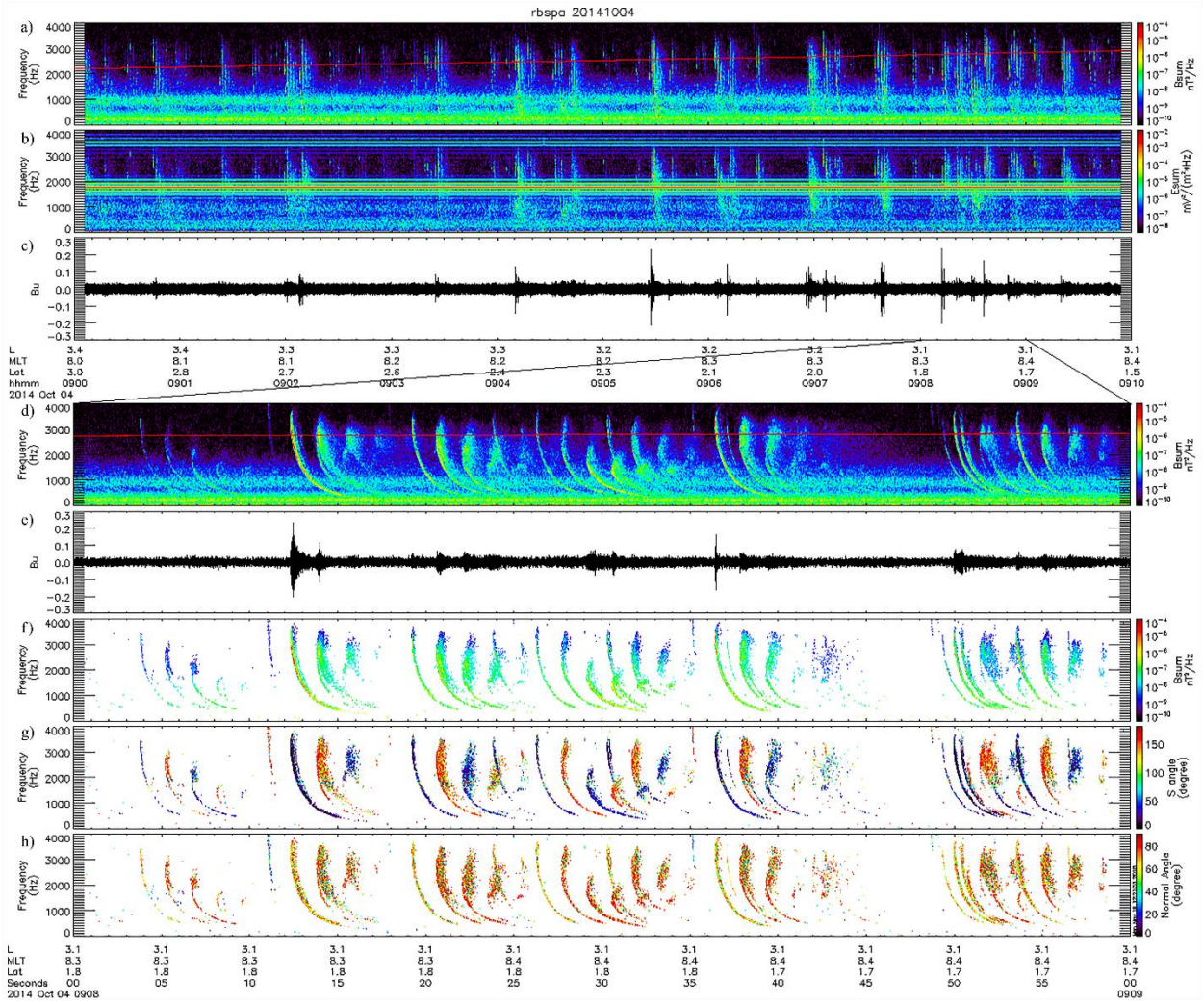

Figure 3.1. Overview of wave measurements from RBSP-A on 20141004 from 0900 to 0910 (a-c) and from 0908 to 0909 (d-h). (a) Frequency-time spectrogram of magnetic field spectral density; (b) Electric field spectral density; (c) Waveform of Bu component (UVW is the satellite spinning coordinate system with W axis as the spin axis); (d) Same as (a); (e) Same as (c); (f) Whistler wave magnetic spectral density, only wave spectra with intensities at least 5 times greater than the background (median value) are shown; (g) Poynting vector angle; (h) Wave normal angle. The horizontal lines in Figure 3.1a and 3.1d indicate 0.1 f_{ce}, where f_{ce} represents the local electron gyrofrequency.

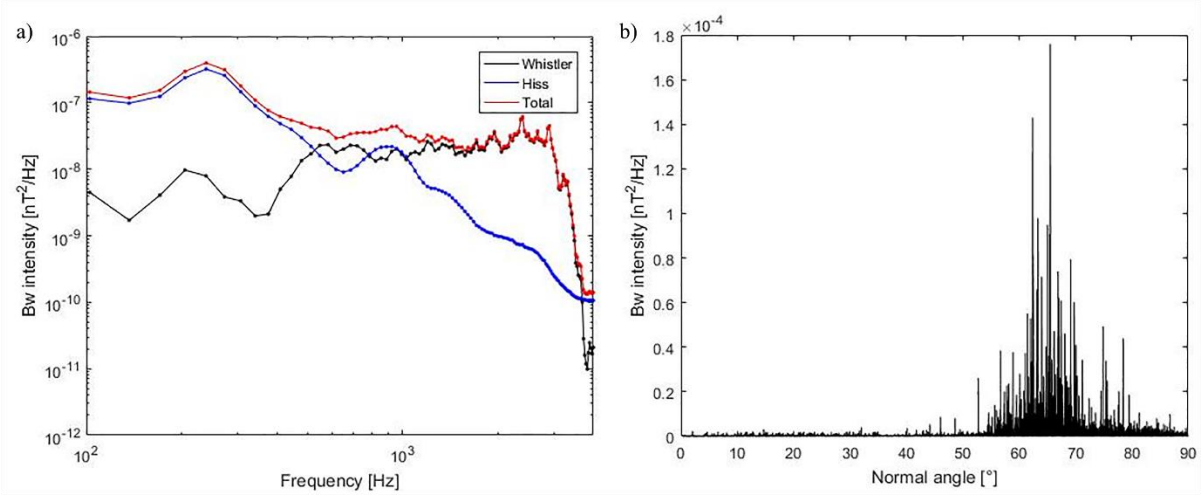

Figure 3.2. Wave power spectral density as a function of frequency (a) and wave normal angle (b) for oblique whistler event on 20141004. Red, blue and black curves indicate the spectrum of all waves, hiss wave and lightning-generated whistler waves.

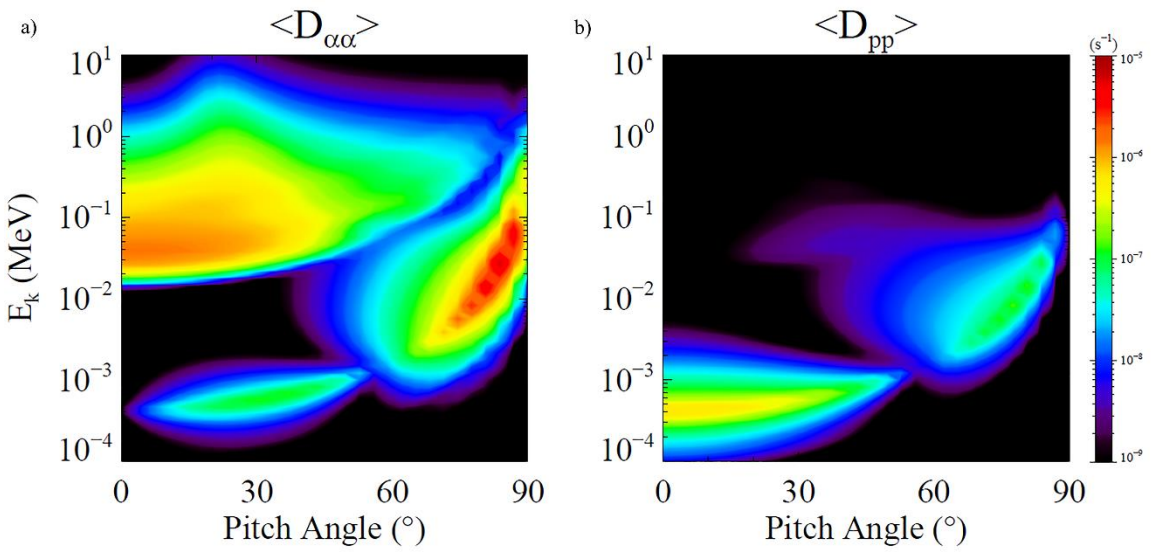

Figure 3.3. Bounce-averaged pitch angle (a) and momentum (b) diffusion coefficients of non-ducted whistlers as a function of pitch angle and energy for oblique whistler event on 20141004.

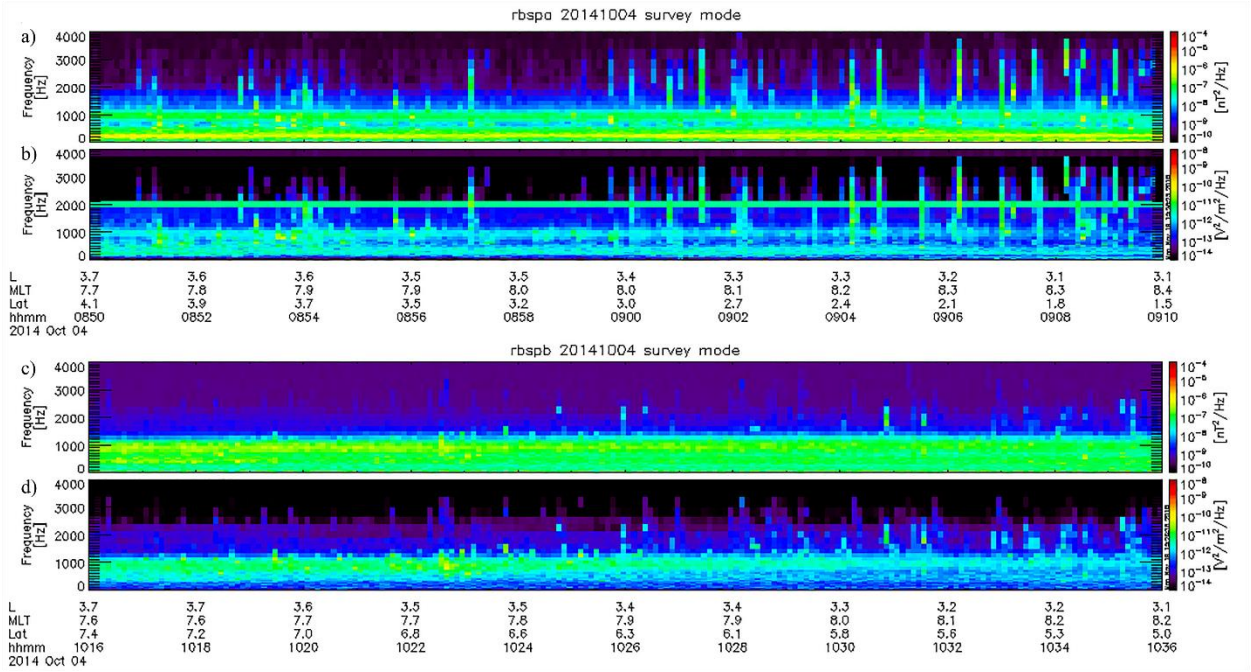

Figure 3.4. WFR survey mode measurements of two Van Allen Probes at same L range. (a, c) Magnetic field spectral density; (b, d) Electric field spectral density.

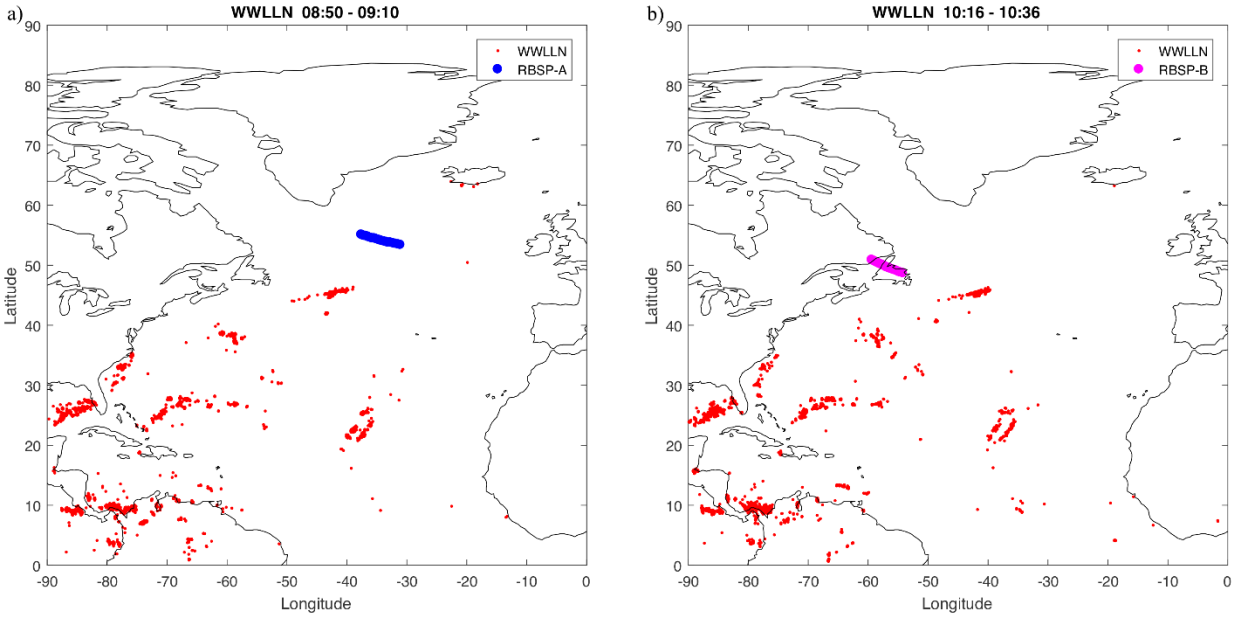

Figure 3.5. WWLLN lightning map when two Van Allen Probes pass the same L shells. The blue and magenta dots represent the footpoints of two Van Allen Probes.

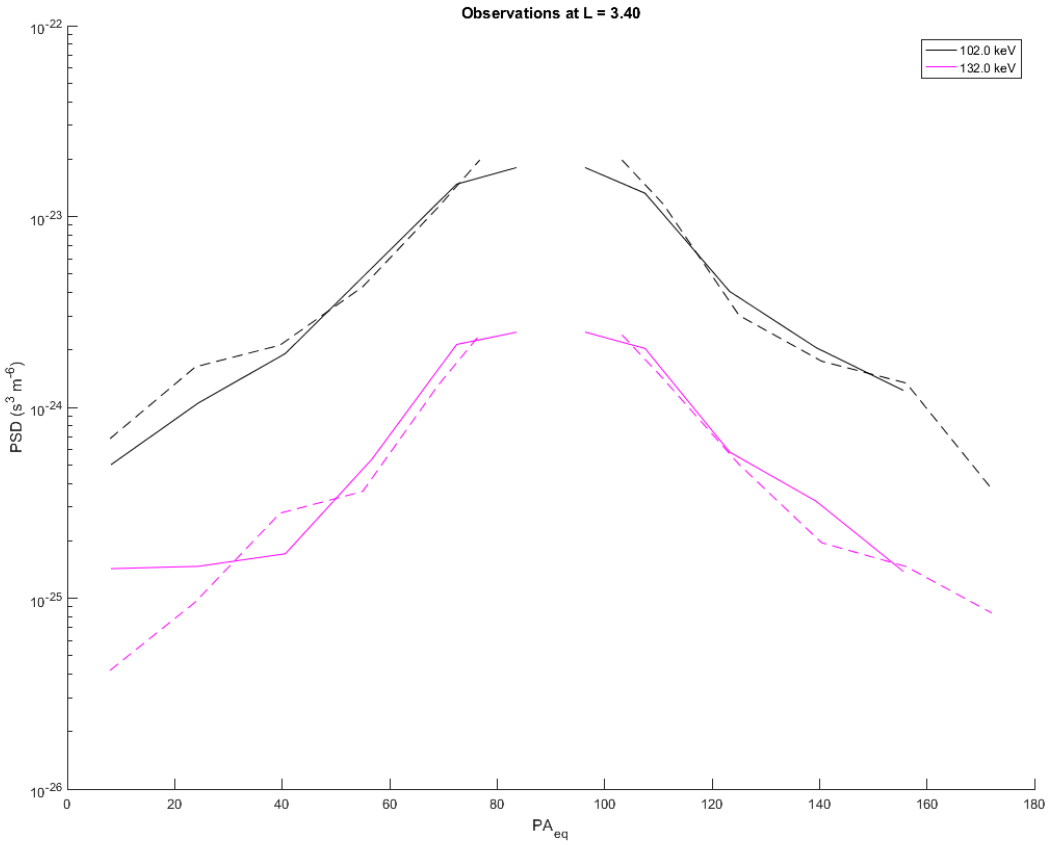

Figure 3.6. Energetic electron pitch angle distribution for 102 keV (black) and 132 keV (red) from Van Allen Probe A (solid) and B (dash) when they passed L = 3.40.

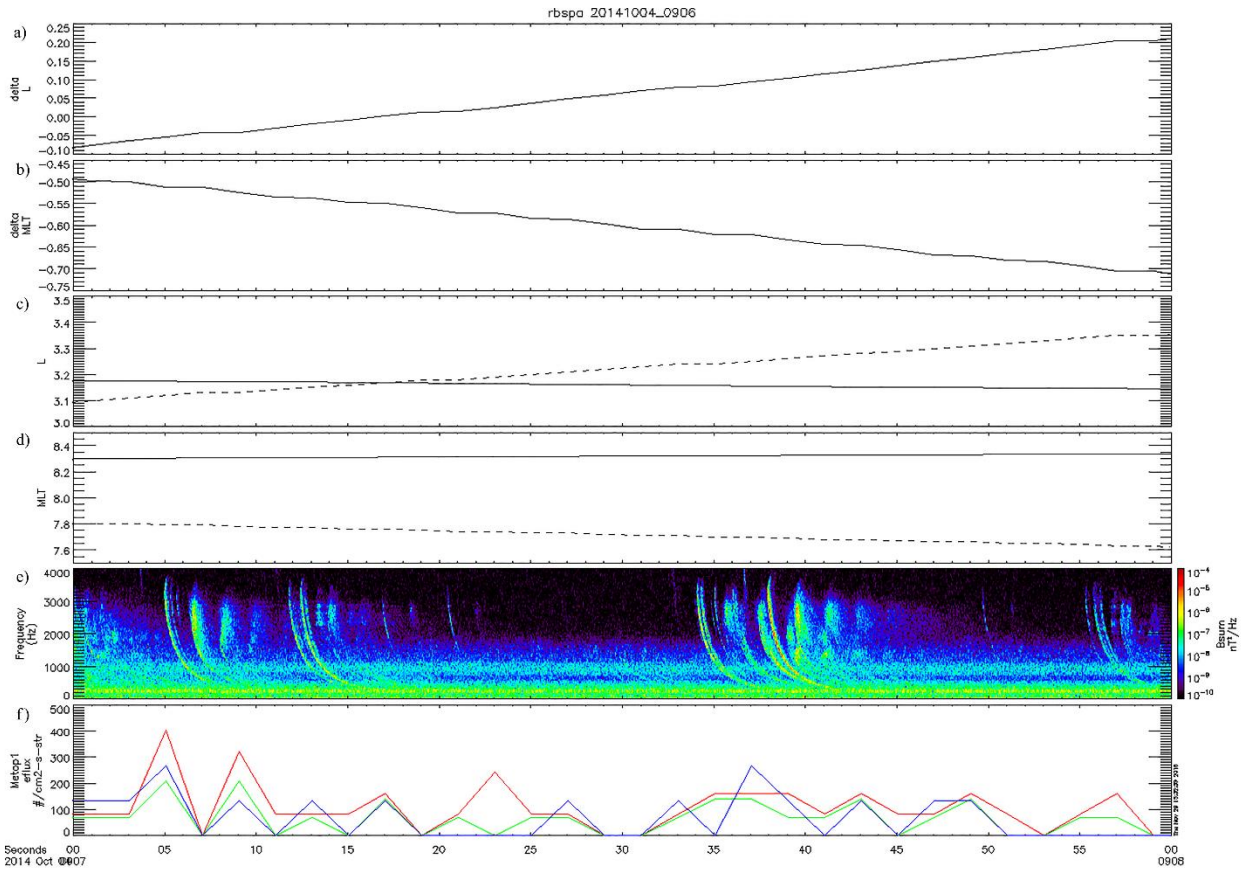

Figure 3.7. (a) L difference; (b) MLT difference; (c-d) L-shell values and MLT of RBSP-A (solid) and Metop-B (dash); (e) Lightning whistlers on RBSP-A; (f) Electron flux from 0° telescope on Metop-B for >40 keV(red), >130 keV (green) and >287 keV (blue).

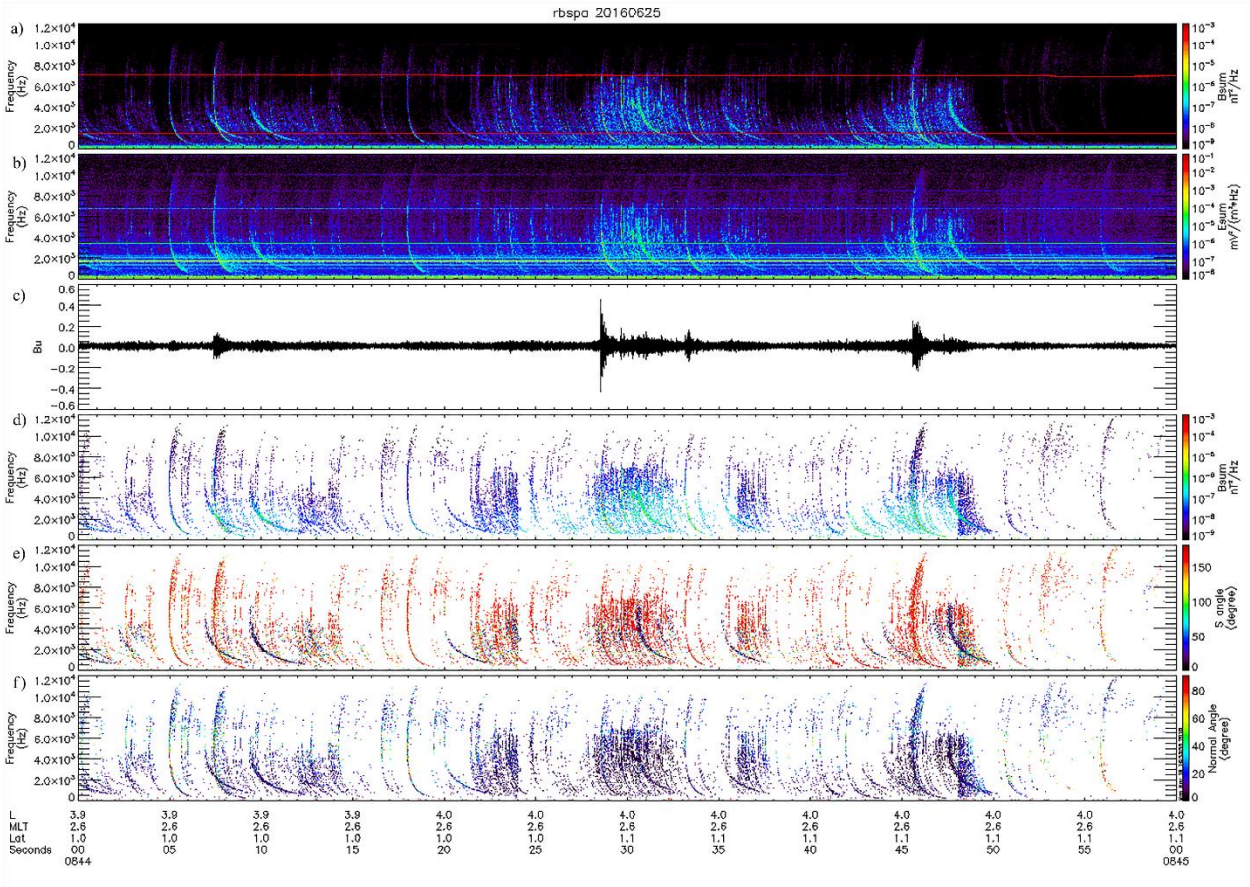

Figure 3.8. Overview of wave measurements from RBSP-A on 20160625 from 0844 to 0845. (a) Frequency-time spectrogram of magnetic field spectral density; (b) Electric field spectral density; (c) Waveform of Bu; (d) Whistler wave magnetic spectral density; (e) Poynting vector angle; (f) Wave normal angle. The horizontal lines in Figure 3.8a indicate $0.5f_{ce}$ and $0.1f_{ce}$.

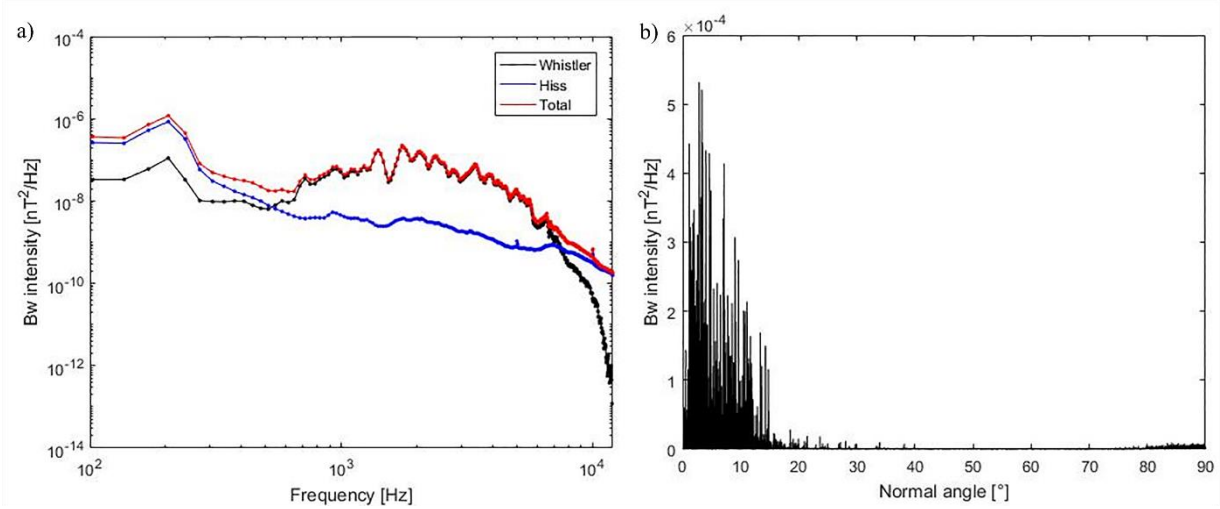

Figure 3.9. Same format as Figure 3.2 for ducted whistler event on 20160625.

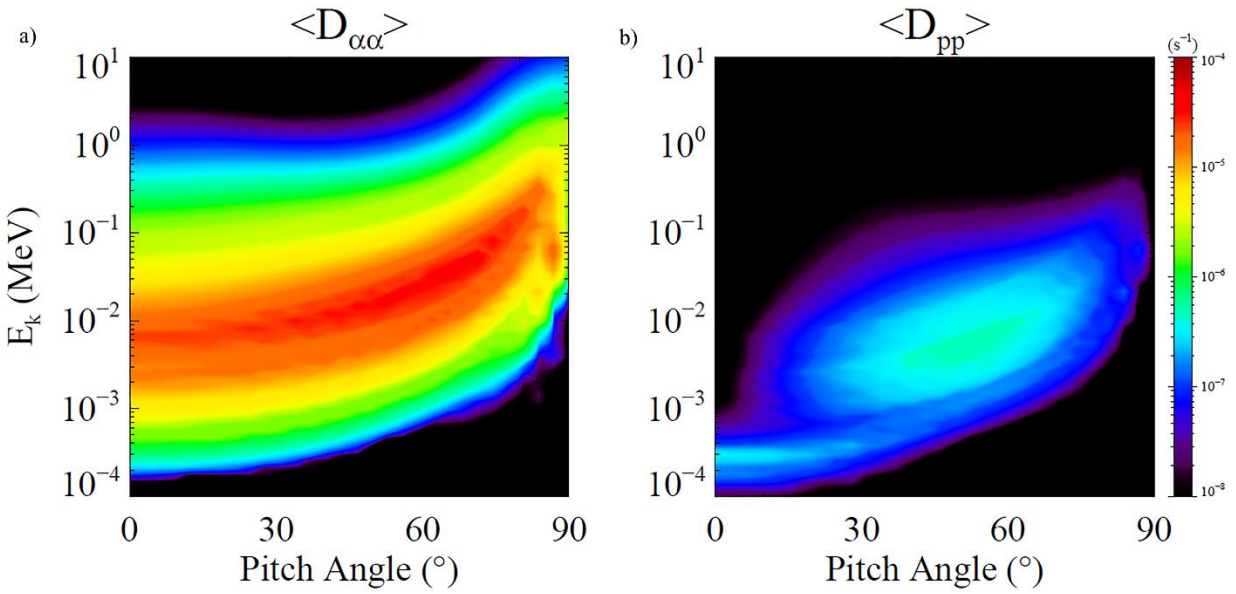

Figure 3.10. Same format as Figure 3.3 for ducted whistler event on 20160625.

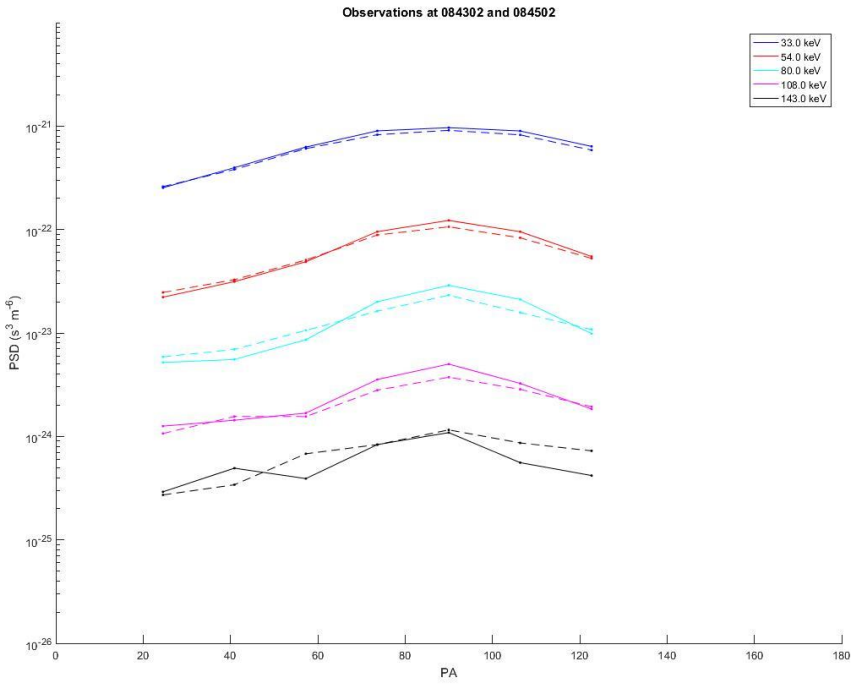

Figure 3.11. Pitch angle distribution of RBSP-A in 2 minutes (solid: before; dash: after). Different colors indicate different energy channels.

Chapter 4. SUMMARY AND FUTURE WORK

In the following chapter, I briefly summarize the key findings in this dissertation and provide suggestions for future work.

4.1 CONCLUSIONS

In this dissertation, we used a new and unique dataset to study lightning-generated whistler waves in the Earth's inner magnetosphere. Global lightning data and high-resolution waveform data in the radiation belts are connected together to study the lightning-generated whistler waves including the source, propagation, wave-particle interactions and electron precipitation.

The conjunction work between WWLLN and Van Allen Probes is conducted from July to September 2013 and from March to April 2014, which provided the simultaneous observations of global lightning and whistler waves used in this thesis. Global lightning data of the past 3 years from WWLLN are used to forecast the lightning occurrence along the magnetic footpoints trajectories of the Van Allen Probes. In each day, a ten-minute window is selected for data collecting in burst mode at the satellites. By using this method, lightning-generated whistler waves near the geomagnetic equator at low L-shells were successfully predicted with a rate of ~80%. About 22.6% of the whistlers observed by the Van Allen Probes corresponds to possible source lightning in the WWLLN data both in time and position. This rate agrees with the detection efficiency of WWLLN. About 40.1% more whistlers observed by Van Allen Probes may correspond with WWLLN lightning if the source region is extended from 2000 km to the global area. The energy of lightning may not be the dominant factor to decide the appearance or absence of the lightning-generated whistler waves in the inner magnetosphere if the far-field radiated

energy of lightning is larger than 100 J. The new data set based on our method can be valuable for the future study of whistler-related phenomena.

In previous research, the pitch angle scattering of energetic electron by lightning-generated whistler waves is estimated by using average wave strength and hypothetical wave normal angle distribution. The results may not be accurate for specific cases. In this thesis, we show detailed analyses for two types of whistler events using new data from Van Allen Probes. The detailed waveform and wave normal angle data of lightning whistlers only are used for calculating the diffusion coefficients. The two events in this thesis both showed stronger wave intensities than the averaged results in the previous work. Specifically, the ducted whistler event, with small wave normal angles is larger than the oblique whistler event with large wave normal angles. The diffusion coefficients show that the strong lightning-generated whistler waves may be important for scattering electrons with energies around 100 keV. Ducted whistler waves may be more effective in pitch angle scattering processes than non-ducted whistler waves due to the small wave normal angles. But from another perspective, the propagation of ducted whistler requires an electron density gradient, and it may not exist long enough. The work in this thesis shows the possibility to simulate the electron precipitation caused by lightning-generated whistler waves in individual cases.

4.2 Future Work Suggestions

The work in this thesis shows several important results with the new data from global lightning and high-time resolution waveform data in the radiation belts. But there are still several studies can be done to extend the understanding in the future.

Ray tracing method is very useful to simulate the propagation of lightning-generated whistler waves from ionosphere to the inner magnetosphere. But currently there is not a complete model to

explain the propagation from lightning to the leak points at the ionosphere. The most common hypothesis used for this process is that any point within 2000 km or more from the lightning can be a possible entry point for lightning-generated whistlers. In the future study, some simulation works can be done to generate a whistler wave strength map based on the distance to the lightning location. After that, we can combine this map with the ray tracing simulations to get a 3-D whistler wave intensity map generated from each individual lighting stroke. Background plasma density from existing models or real measurements can be used as input for ray propagation model. There are some preliminary results at 700 - 800 km [e.g., Jacobson et al., 2016], but it is necessary to extend the model to a high altitude, to the inner magnetosphere.

In this thesis, we only show two whistler events at high L-shells from a list with several hundred whistler events. As mentioned in Chapter Two, the dechirping method no longer works well for the whistler detection at high L-shells. We try to use two methods to identify the whistler waves at high L-shells. The first thing we tried is the dechirping method with a high frequency cutoff around 0.3 or 0.4 f_{ce}. The second thing we used is the cross-matching method in the previous work. We manually generated several reference whistler waves with different dispersion constants as candidates and try to match them with wave spectrograms to see if any one fits better than a set threshold. But neither method can solve the problem perfectly. In the future work, we may build a convolution neural network to identify the whistler wave patterns in the spectrograms. There is already a neural network trained for DEMETER satellite to identify the whistler phenomena at low altitude. The parameters of this neural network are not open, and it only works for well-structed 0+ whistler waves at low altitude. In the future work, a new neural network model can be trained if there are enough whistler training samples at high L-shells.

After we have a better solution on automatic whistler wave detection at high L-shells, we can statistically analyze all whistler wave events to get a better understanding on the whistler wave intensity distribution. It is also possible to get more electron precipitation cases with the conjunction work of low altitude satellites (like new CubeSats with high resolution electron flux data) and the Van Allen Probes.

References

Abarca, S. F., K. L. Corbosiero, and T. J. Galarneau (2010), An evaluation of the Worldwide Lightning Location Network (WWLLN) using the National Lightning Detection Network (NLDN) as ground truth, J. Geophys. Res., 115, D18206, doi:10.1029/2009JD013411.

Abel, B., and R. M. Thorne (1998a), Electron scattering loss in Earth's inner magnetosphere: 1. Dominant physical processes, J. Geophys. Res.,103(A2), 2385–2396, doi:10.1029/97JA02919.

Abel, B., and R. M. Thorne (1998b), Electron scattering loss in Earth's inner magnetosphere: 2. Sensitivity to model parameters, J. Geophys. Res., 103(A2), 2397–2407, doi:10.1029/97JA02920.

Baumjohann, W. and R. A. Treumann (1997), Basic Space Plasma Physics, World Scientific Press.

Blake, J. B., Inan, U. S., Walt, M., Bell, T. F., Bortnik, J., Chenette, D. L., and Christian, H. J. (2001), Lightning-induced energetic electron flux enhancements in the drift loss cone, J. Geophys. Res., 106(A12), 29733–29744, doi:10.1029/2001JA000067.

Blake, J. B., et al. (2013), The Magnetic Electron Ion Spectrometer (MagEIS) Instruments Aboard the Radiation Belt Storm Probes (RBSP) Spacecraft, Space Sci. Rev., 179, 1-4, doi:10.1007/S11214-013-9991-8.

Bortnik, J., U. S. Inan, and T. F. Bell (2002), L dependence of energetic electron precipitation driven by magnetospherically reflecting whistler waves, J. Geophys. Res., 107(A8), 1150, doi:10.1029/2001JA000303.

Bortnik, J., U. S. Inan, and T. F. Bell (2003), Frequency-time spectra of magnetospherically reflecting whistlers in the plasmasphere, J. Geophys. Res., 108(A1), 1030, doi:10.1029/2002JA009387.

Bortnik, J. (2004), Precipitation of radiation belt electrons by lightning-generated magnetospherically reflecting whistler waves, Stanford University Press.

Bortnik, J., Thorne, R. M., O'Brien, T. P., Green, J. C., Strangeway, R. J., Shprits, Y. Y., and Baker, D. N. (2006a), Observation of two distinct, rapid loss mechanisms during the 20 November 2003 radiation belt dropout event, J. Geophys. Res., 111, A12216, doi:10.1029/2006JA011802.

Bortnik, J., Inan, U. S., and Bell, T. F. (2006b), Temporal signatures of radiation belt electron precipitation induced by lightning-generated MR whistler waves: 1. Methodology, J. Geophys. Res., 111, A02204, doi:10.1029/2005JA011182.

Burkholder, B. S., M. L. Hutchins, M. P. McCarthy, R. F. Pfaff, and R. H. Holzworth (2013), Attenuation of lightning-produced sferics in the Earth-ionosphere waveguide and low-latitude ionosphere, J. Geophys. Res. Space Physics, 118, 3692–3699, doi:10.1002/jgra.50351.

Carpenter, D. L. (1963), Whistler evidence of a 'knee' in the magnetospheric ionization density profile, J. Geophys. Res., 68(6), 1675-1682, doi:10.1029/JZ068i006p01675.

Dowden, R. L. (1971), VLF discrete emissions deduced from Helliwell's theory, J. Geophys. Res., 76(13), 3046– 3054, doi:10.1029/JA076i013p03046.

Dowden, R. L., J. B. Brundell, and C. J. Rodger (2002), VLF lightning location by time of group arrival (TOGA) at multiple sites, J. Atmos. Sol. Terr. Phys., 64(7), 817–830, doi:10.1016/S1364-6826(02)00085-8.

Draganov, A. B., U. S. Inan, V. S. Sonwalkar, and T. F. Bell (1992), Magnetospherically reflected whistlers as a source of plasmaspheric hiss, Geophys. Res. Lett., 19(3), 233–236, doi:10.1029/91GL03167.

Dungey, J. (1963), Loss of Van Allen electrons due to whistlers, Planet. Space Sci., 11(6), 591–595, doi:10.1016/0032-0633(63)90166-1.

Evans, D. S., and M. S. Greer (2004), Polar Orbiting Environmental Satellite Space Environment Monitor-2: Instrument descriptions and archive data documentation, NOAA Tech. Mem. 93, version 1.4, Space Weather Predict. Cent., Boulder, Colo.

Fiser, J., J. Chum, G. Diendorfer, M. Parrot, and O. Santolik (2010), Whistler intensities above thunderstorms, Ann. Geophys., 28(1), 37–46, doi:10.5194/angeo-28-37-2010.

Glauert, S. A., Horne, R. B., and Meredith, N. P. (2014), Three-dimensional electron radiation belt simulations using the BAS Radiation Belt Model with new diffusion models for chorus, plasmaspheric hiss, and lightning-generated whistlers, J. Geophys. Res. Space Physics, 119, 268–289, doi:10.1002/2013JA019281.

Goldberg, R. A., J. R. Barcus, L. C. Hale, and S. A. Curtis (1986), Direct observation of magnetospheric electron precipitation stimulated by lightning, J. Atmos. Terr. Phys., 48(3), 293–299.

Green, J. L., S. Boardsen, L. Garcia, W. W. L. Taylor, S. F. Fung, and B. W. Reinisch (2005), On the origin of whistler mode radiation in the plasmasphere, J. Geophys. Res., 110, A03201, doi:10.1029/2004JA010495.

Green, J. L., S. Boardsen, L. Garcia, W. W. Taylor, S. F. Fung, and B. W. Reinisch (2006), Reply to comment on "On the origin of whistler mode radiation in the plasmasphere" by Green et al., J. Geophys. Res., 111, A09211, doi:10.1029/2006JA011622.

Gurnett, D. A., and U. S. Inan (1988), Plasma wave observations with the dynamics explorer 1 spacecraft, Rev. Geophys., 26(2), 285–316, doi:10.1029/RG026i002p00285.

Helliwell, R. A. (1965), Whistlers and Related Ionospheric Phenomena, Stanford Univ. Press, Stanford, Calif.

Holzworth, R. H., M. C. Kelley, C. L. Siefring, L. C. Hale, and J. D. Mitchell (1985), Electrical measurements in the atmosphere and the ionosphere over an active thunderstorm: 2. Direct current electric fields and conductivity, J. Geophys. Res., 90(A10), 9824–9830, doi:10.1029/JA090iA10p09824.

Holzworth, R. H., R. M. Winglee, B. H. Barnum, Y. Li, and M. C. Kelley (1999), Lightning whistler waves in the high-latitude magnetosphere, J. Geophys. Res., 104(A8), 17,369–17,378, doi:10.1029/1999JA900160.

Holzworth, R. H., M. P. McCarthy, R. F. Pfaff, A. R. Jacobson, W. L. Willcockson, and D. E. Rowland (2011), Lightning-generated whistler waves observed by probes on the Communication/Navigation Outage Forecast System satellite at low latitudes, J. Geophys. Res., 116, A06306, doi:10.1029/2010JA016198.

Horne, R. B., N. P. Meredith, R. M. Thorne, D. Heynderickx, R. H. A. Iles, and R. R. Anderson (2003), Evolution of energetic electron pitch angle distributions during storm time electron acceleration to megaelectronvolt energies, J. Geophys. Res., 108(A1), 1016, doi:10.1029/2001JA009165.

Hutchins, M. L., R. H. Holzworth, J. B. Brundell, and C. J. Rodger (2012), Relative detection efficiency of the World Wide Lightning Location Network, Radio Sci., 47, RS6005, doi:10.1029/2012RS005049.

Hutchins, M. L., R. H. Holzworth, K. S. Virts, J. M. Wallace, and S. Heckman (2013), Radiated VLF energy differences of land and oceanic lightning, Geophys. Res. Lett., 40, 2390–2394, doi:10.1002/grl.50406.

Hutchins, M. L., R. H. Holzworth, and J. B. Brundell (2014), Diurnal variation of the global electric circuit from clustered thunderstorms, J. Geophys. Res. Space Physics, 119, 620–629, doi:10.1002/2013JA019593.

Inan, U. S., Piddyachiy, D., Peter, W. B., Sauvaud, J. A., and Parrot, M. (2007), DEMETER satellite observations of lightning‐induced electron precipitation, Geophys. Res. Lett., 34, L07103, doi:10.1029/2006GL029238.

Jacobson, A. R., R. Holzworth, J. Harlin, R. Dowden, and E. Lay (2006), Performance assessment of the World Wide Lightning Location Network (WWLLN), using the Los Alamos Sferic Array (LASA) as ground truth, J. Atmos. Oceanic Technol., 23(8), 1082–1092, doi:10.1175/JTECH1902.1.

Jacobson, A. R., R. H. Holzworth, R. F. Pfaff, and M. P. McCarthy (2011), Study of oblique whistlers in the low-latitude ionosphere, jointly with the C/NOFS satellite and the World-Wide Lightning Location Network, Ann. Geophys., 29(5), 851–863, doi:10.5194/angeo-29-851-2011.

Jacobson, A. R., Holzworth, R. H., Pfaff, R., and Heelis, R. (2016), Automated identification of discrete, lightning-generated, multiple-dispersed whistler waves in C/NOFS-VEFI very low frequency observations, Radio Sci., 51, 1547–1569, doi:10.1002/2016RS005989.

Kelley, M. C., Siefring, C. L., Pfaff, R. F., Kintner, P. M., Larsen, M., Green, R., Holzworth, R. H., Hale, L. C., Mitchell, J. D., and Le Vine, D. (1985), Electrical measurements in the atmosphere and the ionosphere over an active thunderstorm: 1. Campaign overview and initial ionospheric results, J. Geophys. Res., 90(A10), 9815–9823, doi:10.1029/JA090iA10p09815.

Kelley, M. C., J. G. Ding, and R. H. Holzworth (1990), Intense ionospheric electric and magnetic field pulses generated by lightning, Geophys. Res. Lett., 17(12), 2221–2224, doi:10.1029/GL017i012p02221.

Kletzing, C., et al. (2013), The Electric and Magnetic Field Instrument Suite and Integrated Science (EMFISIS) on RBSP, Space Sci. Rev., 179(1–4), 127–181, doi:10.1007/s11214-013-9993-6.

Koons, H. C. (1985), Whistlers and whistler-stimulated emissions in the outer magnetosphere, J. Geophys. Res., 90(A9), 8547–8551, doi:10.1029/JA090iA09p08547.

Kurth, W. S., S. De Pascuale, J. B. Faden, C. A. Kletzing, G. B. Hospodarsky, S. Thaller, and J. R. Wygant (2015), Electron densities inferred from plasma wave spectra obtained by the Waves instrument on Van Allen Probes, J. Geophys. Res. Space Physics, 120, 904–914, doi:10.1002/2014JA020857.

Lauben, D. S., U. S. Inan, and T. F. Bell (2001), Precipitation of radiation belt electrons induced by obliquely propagating lightning-generated whistlers, J. Geophys. Res., 106(A12), 29,745–29,770, doi:10.1029/1999JA000155.

Li, W., Bortnik, J., Thorne, R. M., and Angelopoulos, V. (2011), Global distribution of wave amplitudes and wave normal angles of chorus waves using THEMIS wave observations, J. Geophys. Res., 116, A12205, doi:10.1029/2011JA017035.

Li, W., et al. (2013), An unusual enhancement of low-frequency plasmaspheric hiss in the outer plasmasphere associated with substorm-injected electrons, Geophys. Res. Lett., 40, 3798-3803, doi:10.1002/grl.50787.

Li, W., et al. (2014), Radiation belt electron acceleration by chorus waves during the 17 March 2013 storm, J. Geophys. Res. Space Physics, 119, 4681–4693, doi:10.1002/2014JA019945.

Li, Y. Q., R. H. Holzworth, H. Hu, M. McCarthy, R. D. Massey, P. M. Kintner, J. V. Rodrigues, U. S. Inan, and W. C. Armstrong (1991), Anomalous optical events detected by rocket-borne sensor in the WIPP campaign, J. Geophys. Res., 96(A2), 1315–1326, doi:10.1029/90JA01727.

Liemohn, H. B., and F. L. Scarf (1964), Whistler determination of electron energy and density distributions in the magnetosphere, J. Geophys. Res., 69(5), 883–904, doi:10.1029/JZ069i005p00883.

Ma, Q., Li, W., Thorne, R. M., Ni, B., Kletzing, C. A., Kurth, W. S., Hospodarsky, G. B., Reeves, G. D., Henderson, M. G., Spence, H. E., Baker, D. N., Blake, J. B., Fennell, J. F., Claudepierre, S. G. and Angelopoulos, V. (2015), Modeling inward diffusion and slow decay of energetic electrons in the Earth's outer radiation belt. Geophys. Res. Lett., 42: 987–995. doi: 10.1002/2014GL062977.

Ma, Q., Mourenas, D., Li, W., Artemyev, A., and Thorne, R. M. (2017), VLF waves from ground‐based transmitters observed by the Van Allen Probes: Statistical model and effects on plasmaspheric electrons, Geophys. Res. Lett., 44, 6483–6491, doi:10.1002/2017GL073885.

Meredith, N. P., Thorne, R. M., Horne, R. B., Summers, D., Fraser, B. J., and Anderson, R. R. (2003a), Statistical analysis of relativistic electron energies for cyclotron resonance with EMIC waves observed on CRRES, J. Geophys. Res., 108, 1250, doi:10.1029/2002JA009700, A6.

Meredith, N. P., R. B. Horne, R. M. Thorne, and R. R. Anderson (2003b), Favored regions for chorus-driven electron acceleration to relativistic energies in the Earth's outer radiation belt, Geophys. Res. Lett., 30(16), 1871, doi:10.1029/2003GL017698.

Meredith, N. P., R. B. Horne, M. A. Clilverd, D. Horsfall, R. M. Thorne, and R. R. Anderson (2006), Origins of plasmaspheric hiss, J. Geophys. Res., 111, A09217, doi:10.1029/2006JA011707.

Meredith, N. P., Horne, R. B., Glauert, S. A., and Anderson, R. R. (2007), Slot region electron loss timescales due to plasmaspheric hiss and lightning-generated whistlers, J. Geophys. Res., 112, A08214, doi:10.1029/2007JA012413.

Meredith, N. P., R. B. Horne, S. A. Glauert, D. N. Baker, S. G. Kanekal, and J. M. Albert (2009), Relativistic electron loss timescales in the slot region, J. Geophys. Res., 114, A03222, doi:10.1029/2008JA013889.

Meredith, N. P., Horne, R. B., Isles, J. D., and Green, J. C. (2016), Extreme energetic electron fluxes in low Earth orbit: Analysis of POES E > 30, E > 100, and E > 300 keV electrons, Space Weather, 14, 136–150, doi:10.1002/2015SW001348.

Millan, R., and R. Thorne (2007), Review of radiation belt relativistic electron losses, J. Atmos. Sol. Terr. Phys., 69(3), 362–377, doi:10.1016/j.jastp.2006.06.019.

Ni, B., R. M. Thorne, Y. Y. Shprits, and J. Bortnik (2008), Resonant scattering of plasma sheet electrons by whistler-mode chorus: Contribution to diffuse auroral precipitation, Geophys. Res. Lett., 35, L11106, doi:10.1029/2008GL034032.

Ni, B., Thorne, R. M., Meredith, N. P., Shprits, Y. Y., and Horne, R. B. (2011), Diffuse auroral scattering by whistler mode chorus waves: Dependence on wave normal angle distribution, J. Geophys. Res., 116, A10207, doi:10.1029/2011JA016517.

Ni, B., Bortnik, J., Thorne, R. M., Ma, Q., and Chen, L. (2013), Resonant scattering and resultant pitch angle evolution of relativistic electrons by plasmaspheric hiss, J. Geophys. Res. Space Physics, 118, 7740–7751, doi:10.1002/2013JA019260.

Park, C. G., and D. L. Carpenter (1970), Whistler evidence of large-scale electron-density irregularities in the plasmasphere, J. Geophys. Res., 75(19), 3825–3836, doi:10.1029/JA075i019p03825.

Park, C. G., D. L. Carpenter, and D. B. Wiggin (1978), Electron density in the plasmasphere: Whistler data on solar cycle, annual, and diurnal variations, J. Geophys. Res., 83(A7), 3137–3144, doi:10.1029/JA083iA07p03137.

Rodger, C. J., Clilverd, M. A., and McCormick, R. J. (2003), Significance of lightning-generated whistlers to inner radiation belt electron lifetimes, J. Geophys. Res., 108, 1462, doi:10.1029/2003JA009906, A12.

Rodger, C. J., R. J. McCormick, and M. A. Clilverd (2004), Testing the importance of precipitation loss mechanisms in the inner radiation belt, Geophys. Res. Lett., 31, L10803, doi:10.1029/2004GL019501.

Rodger, C. J., J. B. Brundell, R. H. Holzworth, and E. H. Lay (2009), Growing detection efficiency of the World Wide Lightning Location Network, AIP Conf. Proc., 1118(1), 15–20, doi:10.1063/1.3137706.

Rycroft, M. J. (1973), Enhanced energetic electron intensities at 100 km altitude and a whistler propagating through the plasmasphere, Planet. Space Sci., 21, 241–251, doi:10.1016/0032-0633(73)90009-3.

Santolík, O., Parrot, M., and Lefeuvre, F. (2003), Singular value decomposition methods for wave propagation analysis, Radio Sci., 38, 1010, doi:10.1029/2000RS002523, 1.

Santolík, O., M. Parrot, U. Inan, D. Burešová, D. Gurnett, and J. Chum (2009), Propagation of unducted whistlers from their source lightning: A case study, J. Geophys. Res., 114, A03212, doi:10.1029/2008JA013776.

Santolík, O., Pickett, J. S., Gurnett, D. A., Menietti, J. D., Tsurutani, B. T., and Verkhoglyadova, O. (2010), Survey of Poynting flux of whistler mode chorus in the outer zone, J. Geophys. Res., 115, A00F13, doi:10.1029/2009JA014925.

Shprits, Y. Y., and B. Ni (2009), Dependence of the quasi-linear scattering rates on the wave normal distribution of chorus waves, J. Geophys. Res.,114, A11205, doi:10.1029/2009JA014223.

Smith, R. L., and Angerami, J. J. (1968), Magnetospheric properties deduced from OGO 1 observations of ducted and nonducted whistlers, J. Geophys. Res., 73(1), 1–20, doi:10.1029/JA073i001p00001.

Sonwalkar, V. S., and U. S. Inan (1989), Lightning as an embryonic source of VLF hiss, J. Geophys. Res., 94(A6), 6986–6994, doi:10.1029/JA094iA06p06986.

Stratton, J., R. Harvey, and G. Heyler (2013), Mission overview for the Radiation Belt Storm Probes mission, Space Sci. Rev., 179(1–4), 29–57, doi:10.1007/s11214-012-9933-x.

Summers, D., C. Ma, N. P. Meredith, R. B. Horne, R. M. Thorne, D. Heynderickx, and R. R. Anderson (2002), Model of the energization of outer-zone electrons by whistler-mode chorus during the October 9, 1990 geomagnetic storm, Geophys. Res. Lett., 29(24), 2174, doi:10.1029/2002GL016039.

Thorne, R. M., T. P. O'Brien, Y. Y. Shprits, D. Summers, and R. B. Horne (2005), Timescale for MeV electron microburst loss during geomagnetic storms, J. Geophys. Res., 110, A09202, doi:10.1029/2004JA010882.

Thorne, R. M., R. B. Horne, and N. P. Meredith (2006), Comment on "Onthe origin of whistler mode radiation in the plasmasphere" by Green et al., J. Geophys. Res.,111, A09210, doi:10.1029/2005JA011477.

Tsurutani, B. T., and Lakhina, G. S. (1997), Some basic concepts of wave-particle interactions in collisionless plasmas, Rev. Geophys., 35(4), 491–501, doi:10.1029/97RG02200.

Tsyganenko, N. (1989), A magnetospheric magnetic field model with a warped tail current sheet, Planet. Space Sci., 37(1), 5–20, doi:10.1016/0032-0633(89)90066-4.

Turner, D. L., Y. Y. Shprits, M. Hartinger, and V. Angelopoulos (2012), Explaining sudden losses of relativistic electrons during geomagnetic storms, Nature Phys., 8, doi:10.1038/NPHYS2185.

Van Allen, J. A., and L. A. Frank (1959), Radiation around the earth to a radial distance of 107,400 km, Nature, 183, 430-434, doi:10.1038/183430a0.

Voss, H., et al. (1984), Lightning-induced electron precipitation, Nature, 312, 740–742, doi:10.1038/312740a0.

Voss, H. D., M. Walt, W. L. Imhof, J. Mobilia, and U. S. Inan (1998), Satellite observations of lightning-induced electron precipitation, J. Geophys. Res., 103(A6), 11,725–11,744, doi:10.1029/97JA02878.

Walt, M., and W. M. MacDonald (1964), The influence of the Earth's atmosphere on geomagnetically trapped particles, Rev. Geophys., 2(4), 543–577, doi:10.1029/RG002i004p00543.

Walt, M. (1994), Introduction to geomagnetically trapped radiation, Cambridge University Press.

Wygant, J., et al. (2013), The electric field and waves instruments on the radiation belt storm probes mission, Space Sci. Rev., 179(1–4), 183–220, doi:10.1007/s11214-013-0013-7.

Zheng, H., Holzworth, R. H., Brundell, J. B., Jacobson, A. R., Wygant, J. R., Hospodarsky, G. B., Mozer, F. S., and Bonnell, J. (2016), A statistical study of whistler waves observed by Van Allen Probes (RBSP) and lightning detected by WWLLN, J. Geophys. Res. Space Physics, 121, 2067–2079, doi:10.1002/2015JA022010.

Appendix A. WWLLN SERVICE UNIT TEST

A.1 NEW DESIGN

The WWLLN service unit was redesigned due to the audio problems in the Gumstix operating system with new version of kernels. The stereo signals may randomly swap the left and right channels which is a big problem for the analysis of VLF data. There are some other changes in the design of service unit. In the new design, the Gumstix is removed from the service unit and we separate the computer and service unit again like we did in SUv3. By doing that, the new design is more compatible with different computers, and we can easily switch to another one if the current choice is discontinued or there is a major system failure which can't be fixed at our end easily. All the connectors related to the Gumstix are all removed including the HDMI, Ethernet and USB ports. We can no longer remotely control the preamp power supply but we revised the design of yellow LEDs so it can directly monitor the currents feeding into the preamp. The new design is also compatible with both two types of GPS units using in SUv3 and SUv4. The two voltage regulators used in SUv4 are all replaced by DC/DC convertors to guarantee enough power for the circuits. The components of new design are all located on one side now instead of two sides in the previous design.

A.2 COMPUTER SELECTION

The Raspberry Pi 3 Model B+ was chosen to be the current computer instead of a regular desktop used with SUv3. There are several advantages of that, 1) it is light and small; 2) it is not expensive; 3) there is a large community using it, so the support is much better than Gumstix. There are some basic requirements which should be satisfied for the future upgrades, like Internet access (Ethernet connection preferred), Linux Operating System, USB connections and video outputs. There are

some other soft requirements like sound card, RAM size, MicroSD card options, cost and service support.

The new version of Raspberry Pi was chosen for its popularity and support. The operating system of Raspberry Pi, called Raspbian, is a Debian-based computer operating system. The large open source community can provide an environment with flexibility, security and robust. But since the Raspberry Pi doesn't come with a sound card, we need to find a USB sound card, which can analyze 48 kHz stereo signals. The USB sound card we chose here is Behringer U-Control UCA222. It is powered by USB port, and have stereo input choice with RCA connectors.

A.3 DESIGN AND LAYOUT

The board design is shown in Figure A.1 with component name and values. The connections between service unit and Raspberry Pi is not shown in this figure. This a minor problem which can be fixed in the future design. It is designed to be compatible with two types of GPS units. But the output voltage of two types of GPS units are different. The voltage at pin 3 of socket 1 is 3.3V but the voltage at pin 3 of socket 2 is 5V. The voltage difference will not destroy the circuit but may generate different brightness of LED A1 when it is triggered. So, in the future design, it may be better to put one resistor for each TXD output before the conjunction point instead of using only one R6.

The layout is shown in Figure A.2. There are four connectors in the front side (left of Figure A.2), including GPS serial jack, GPS unit connector, stereo jack and preamp jack. There is only one power jack at the back side (right of Figure A.2). We kept the two-way GPS serial communication between computer and service unit by using the FT232 board. The new version of FT232 now uses micro-USB jack instead of mini-USB jack. The connector position of two GPS units are aligned in the horizontal directions but the heights are different, so before we drill the

service unit box, we still need to know which type of GPS unit will be put inside of it. The stereo jack is directly connected to the USB sound card through a stereo-to-RCA cable and the USB sound card is connected to Raspberry Pi.

A.4 CONSTRUCTION

The construction work for the new service unit also includes two parts: board and box. At first, we assemble the board with all the necessary components, socket and jumpers. Then we do several tests (see Section A.5) to make sure the board is working correctly. After that, we start the construction of box. In Figure C.3 and C.4, we have the schematics for box holes and mounting holes on each side. After the drill work, we mount the service unit board into box, plug in all the cables as shown in Figure C.5, and do the final test in the Raspberry Pi system.

A.5 TEST PROCEDURES

In the initial board test, we don't mount the GPS unit or plug in cables. When the input voltage slowly increases from 0 to 12V, the current should reach about 45 mA. Test the voltage for GPS and preamp. The SMT360 socket should have two voltages, 5V on pin 1 and 3.3V on pin 2. The NLC-SKII-CP2_V2.0 socket should only have one voltage, 5V on pin2. All other pins in the GPS part should be zero. We also need to test the voltage for preamp. The voltage between pin 5 and pin 1 should be 15V and the voltage between pin 4 and pin 1 should be -15V.

Turn off the board and mount the GPS unit. At 12 V input voltage, the board should draw about 73 mA.

With all the cables connected, including the GPS and preamp antenna, the board should draw about 117 mA at 12 V input voltage. Both yellow LEDs should be on. Since the GPS unit is not configured so far, we will talk about the red LEDs later.

A.6 SOFTWARE SETUP

The Raspberry Pi system usually boots from a MicroSD card, so we need to build a operating system in a MicroSD card first. Here are the steps to build the system:

1. Download the official Raspbian image from the official website. The current version is Raspbian Stretch.
2. Find right tool and write the image to the MicroSD card.
3. Mount the MicroSD card to any Linux machine, then copy the directory of firstRunFiles to /home/pi/firstRunFiles under the rootfs directory in the MicroSD card. The firstRunFiles directory includes the WWLLN software and all necessary configuration files.
4. Unmount the MicroSD card safely and plug it into the Raspberry Pi.
5. Connect the full system as shown in Figure C.5, boot the Raspberry Pi.
6. Run install.sh and setup.sh under the firstRunFiles directory to install required packages, create accounts and finish the configurations.
7. After reboot, make other necessary configurations in the GUI of raspi_config, like allow ssh access, don't use pi as default log in account, etc.
8. Configure the GPS unit. Run the sendTSIP_*.py script and follow the instructions. There is another way to configure the GPS. We can directly connect the GPS serial to a Windows PC and configure it by Trimble software. After the GPS configuration, both two red LEDs should flash once per second.
9. Check the GPS status by running readTSIP_*.py script.
10. Check VLF data. We need to check the vlf.png file under /home/sferix/public_html directory. This file should provide the latest spectrogram of VLF. The sferics.log file

under /home/sferix/sferics can provide more detailed information about the sferics results.

11. Change the default webpage in the web browser to the vlf.png file so the host can easily visit it.

The SSH tunnel settings are still under test so the network configurations are not listed here. The Raspberry Pi will run with DHCP at this moment. It is easy to change it to a static IP if the host has one. At first, open the file at /etc/dhcpcd.conf with vi or nano. Then scroll all the way to the bottom of the file and add one of the following snippets. Here is an example:

```
interface eth0
static ip_address=192.168.0.10/24
static routers=192.168.0.1
static domain_name_servers=192.168.0.1
```

Here *interface* defines which network interface you are setting the configuration for, *ip_address* is the IP address that you want to set your device to; the /24 is the subnet mask, which indicates 255.255.255.0 in this example; *routers* is the IP address of your gateway (probably the IP address or your router) and *domain_name_servers* is the IP address of your DNS. You can add multiple DNS here separated with a single space. After you type all the required information, save the file and reboot. You can check the IP information by the ifconfig command or any website which can help to identify your IP.

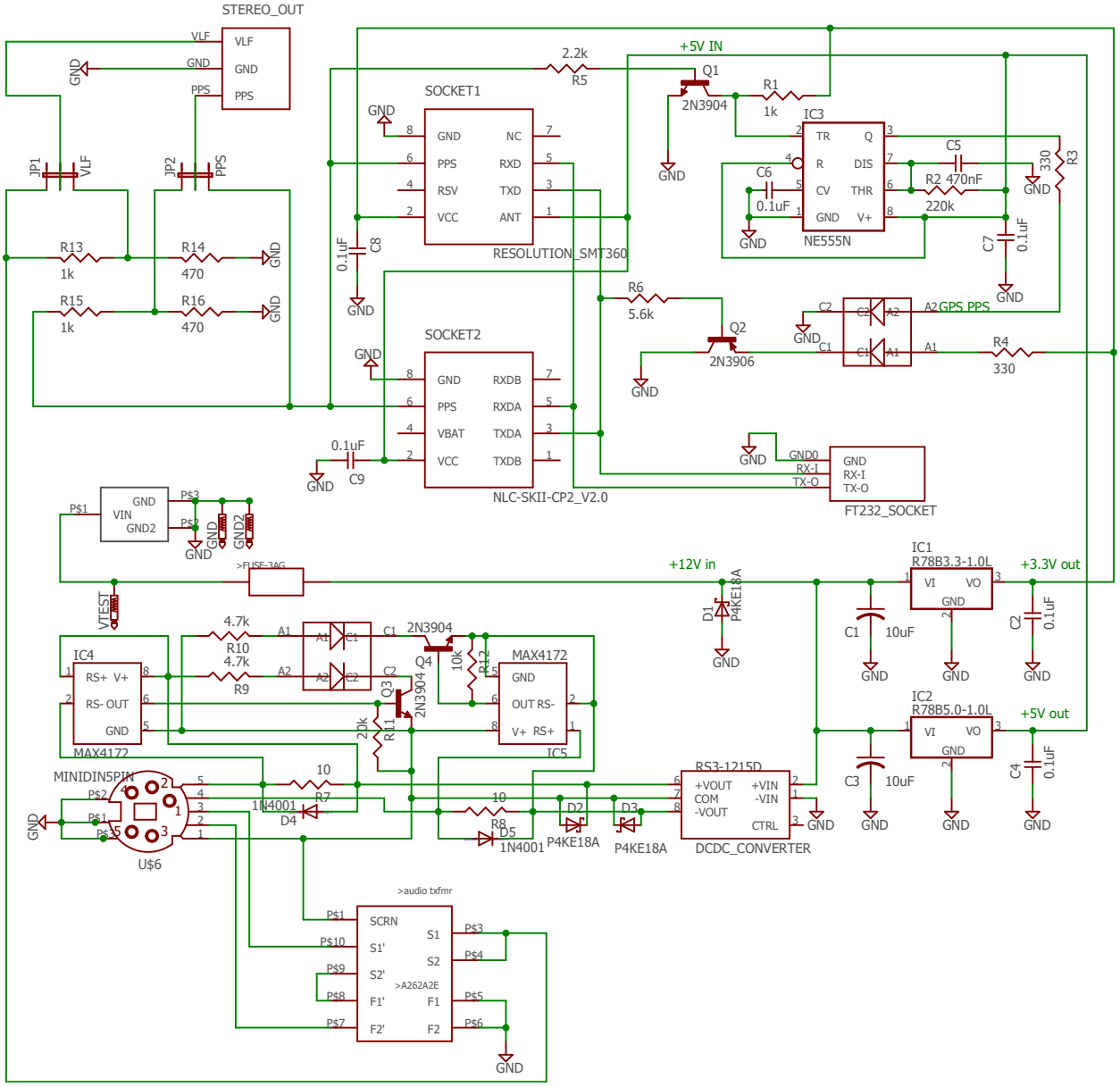

Figure A.1. WWLLN Service Unit Test v2 design.

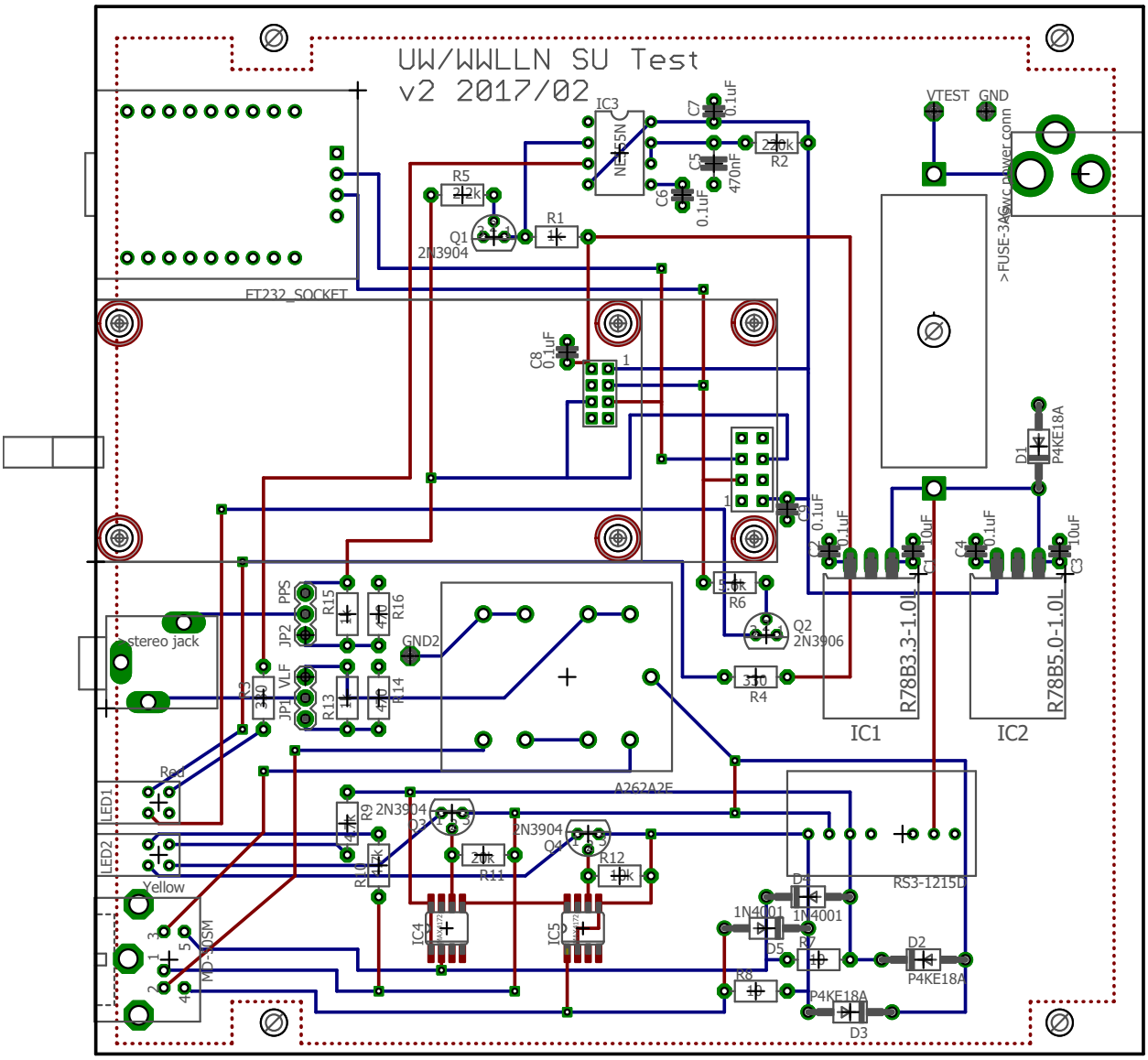

Figure A.2. WWLLN Service Unit Test v2 schematic.

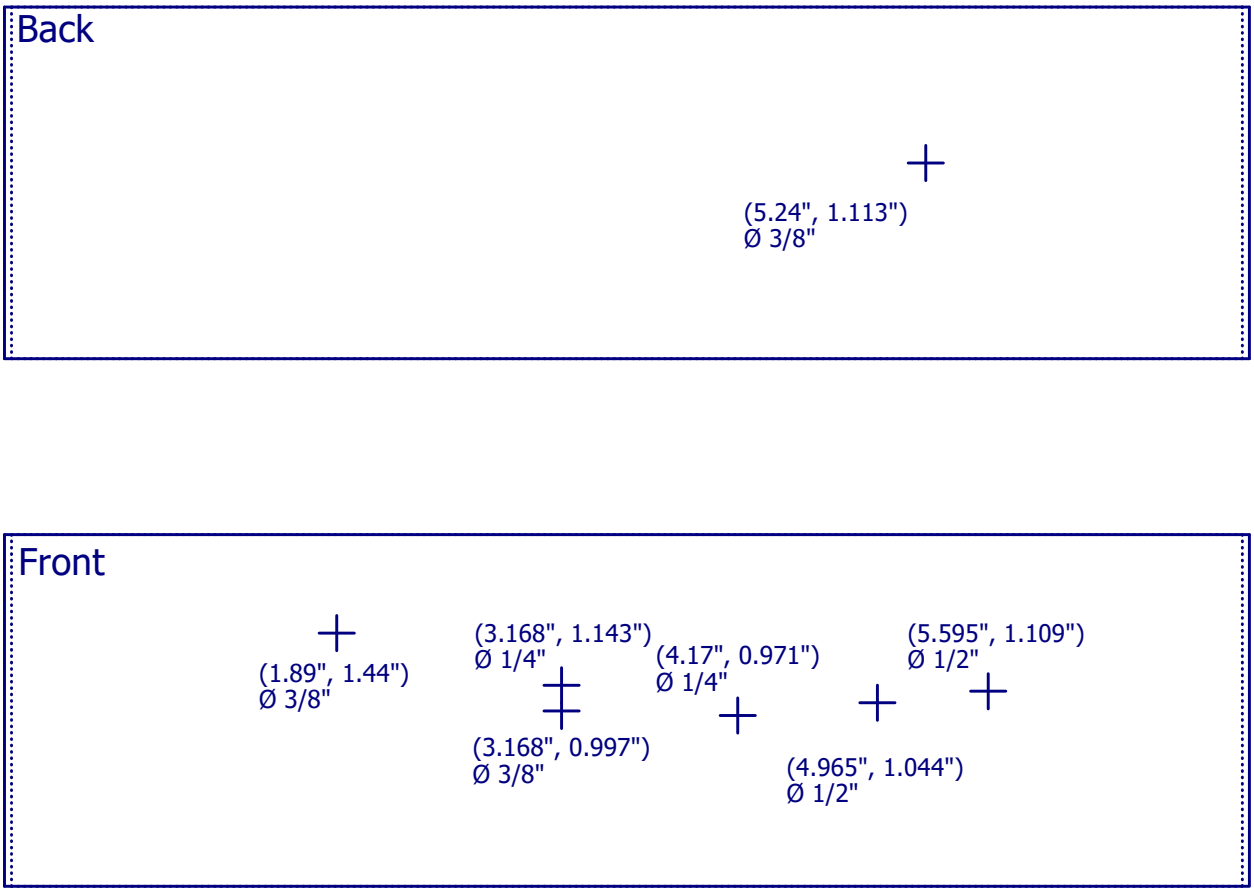

Figure A.3. Schematic for Service Unit box holes.

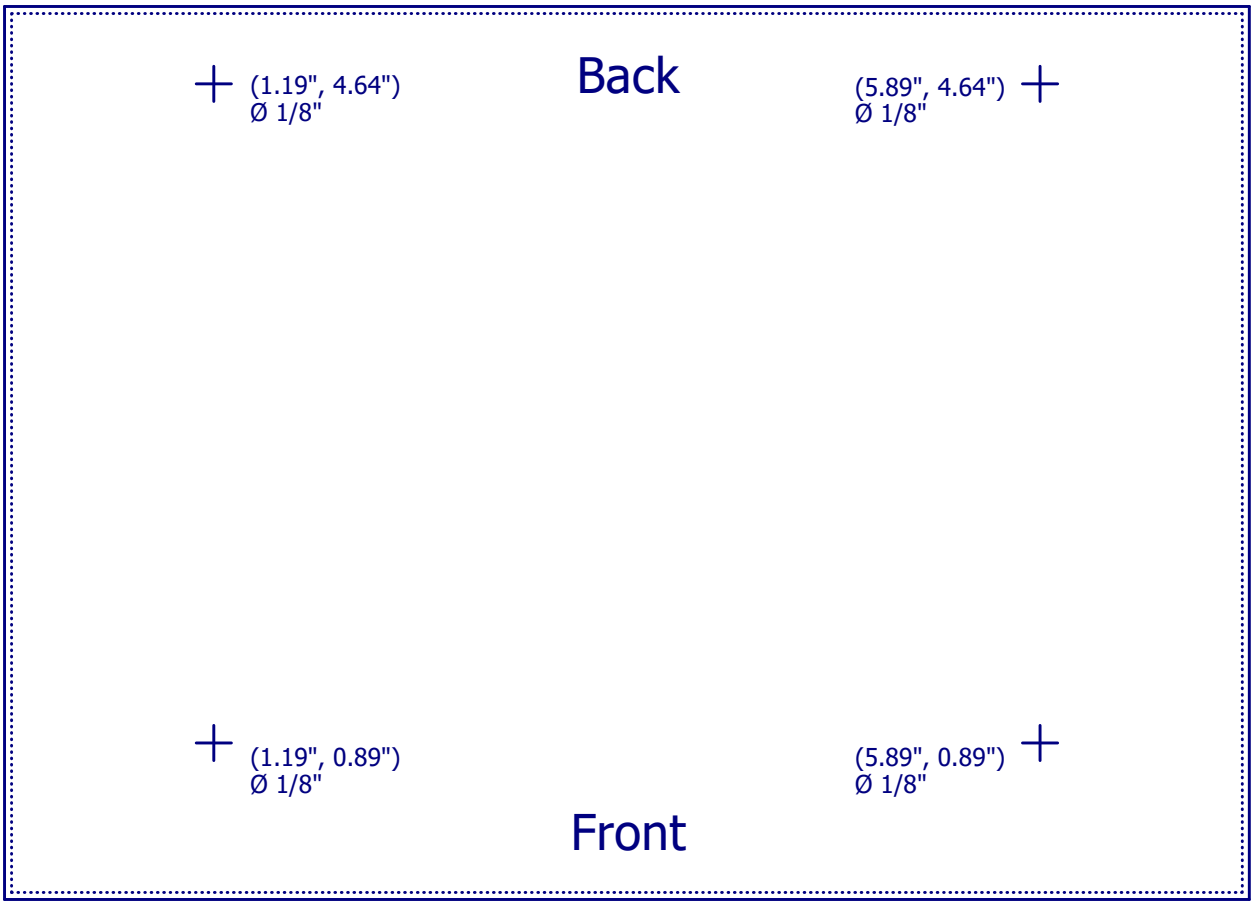

Figure A.4. Schematic for Service Unit mounting holes.

Figure A.5. Overview of WWLLN Service Unit Test.

VITA

Hao Zheng left his hometown to join Peking University for a B.S. in Space Physics. After that, he spent 3 more years to get a M.S. in Space Physics at Peking University. His master thesis studied the Bursty Bulk Flows and Dipolarization Fronts in the magnetotail. In 2012, he took a 12-hour flight to join University of Washington studying lightning-generated whistler waves.